



Excitonic properties in bulk GaN and GaN nanowires under high excitation

Léo Mallet-Dida

► To cite this version:

Léo Mallet-Dida. Excitonic properties in bulk GaN and GaN nanowires under high excitation. Materials Science [cond-mat.mtrl-sci]. Université Clermont Auvergne, 2022. English. NNT : 2022UC-FAC031 . tel-03982395

HAL Id: tel-03982395

<https://theses.hal.science/tel-03982395>

Submitted on 27 Apr 2023

HAL is a multi-disciplinary open access archive for the deposit and dissemination of scientific research documents, whether they are published or not. The documents may come from teaching and research institutions in France or abroad, or from public or private research centers.

L'archive ouverte pluridisciplinaire **HAL**, est destinée au dépôt et à la diffusion de documents scientifiques de niveau recherche, publiés ou non, émanant des établissements d'enseignement et de recherche français ou étrangers, des laboratoires publics ou privés.

UNIVERSITÉ CLERMONT AUVERGNE

ÉCOLE DOCTORALE DES SCIENCES FONDAMENTALES

THESIS

to obtain the grade of

Doctorate of University

Speciality : Dense Environments and Materials

By

LÉO MALLET-DIDA

Excitonic properties in bulk GaN and GaN nanowires under high excitation

Public oral defense on June 30, 2022, with the following commission :

Mathieu GALLART	Associate professor, IPCMS, Strasbourg, France	Reporting judge
Maria TCHERNYCHEVA	Research director, C2N, Paris-Saclay, France	Reporting judge
Blandine ALLOING	Researcher, CNRS-CRHEA, Valbonne, France	Co-supervisor
Joël LEYMARIE	Professor, Institut Pascal, Clermont-Ferrand, France	Thesis director
Pierre DISSEIX	Professor, Institut Pascal, Clermont-Ferrand, France	Examiner
Amélie DUSSAIGNE	Research Engineer, CEA, Grenoble, France	Examiner
Jesús ZÚNIGA-PÉREZ	Research director, CRHEA, France	Examiner

Institut Pascal (Axe Photon) - INP, Université Clermont Auvergne
Centre de Recherche sur l'Hétéro-Epitaxie et ses Applications (CNRS - CRHEA)

"Science isn't about why! It's about why not!"
Cave Johnson

Acknowledgments

J'adresse mon profond respect et mes sincères remerciements aux membres du jury Mathieu Gallart, Maria Tchernycheva, les rapporteurs, ainsi que Amélie Dussaigne et Jesús Zúniga-Pérez, les examinateurs, qui m'ont permis de défendre ma thèse dans d'excellentes conditions.

Un travail de thèse se fait avant tout en équipe. Ce sujet s'inscrit dans la continuité des projets et du savoir faire de l'équipe Spectroscopie Optique des Solides et il me semble important d'en remercier chacun des membres. J'adresse avant tout, mes sincères remerciements à toi Joël pour ta patience et surtout ta capacité à "sentir" la physique. Grâce à tes enseignements, j'ai pu nourrir ma curiosité et apprécier chacun des instants en salle de manip'. Merci Blandine pour ta gentillesse et ta pédagogie, bien que Valbonne soit fort loin de Clermont, les sagesses du CRHEA m'ont vraiment plu et m'ont fait découvrir l'épitaxie. J'exprime aussi ma gratitude envers Jésus pour toutes les discussions durant la thèse et pour l'étendue de ton oeuvre pléthorique dans les semiconducteurs qui m'a profondément inspiré. Merci beaucoup Pierre, sans qui les repas auraient été nettement moins animés sans tes fameuses "Pierrades". Ces heures passées en salle de manip' à tes côtés ont été précieuses et m'ont permis de façonner ma vision scientifique. Merci François pour les moments passés ensemble en fin de thèse. Je regrette que nous n'ayons pas pu échanger plus tôt, ta rigueur et tes méthodologies méticuleuses me suivront pour longtemps. Merci Martine pour ton humanité, ton écoute et ta gentillesse. Merci Pierre B. pour toutes ces supers discussions et ton talent infini de cuisinier. J'ai pu me régaler et ça m'a beaucoup aidé pendant la période de rédaction ! Merci François pour m'avoir formé en début de thèse sur les manips. Enfin, je souhaite beaucoup de courage à mes collègues thésards Léa (dernière ligne droite !) et Loïc (l'aventure commence !), merci pour les bons moments passés à vos côtés.

La vie de thésard au labo se ponctue évidemment de très belles rencontres et collaborations avec les autres équipes et disciplines. Merci à toute l'équipe Croissance d'avoir rendu ces trois années très vivantes et intéressantes, Evelyne, Yamina, Agnes, Mohammed, Hadi, Geoffrey, Jihenn, Manu, Elias, ce fut un réel plaisir. Comment ne pas citer les fiers membres du concours du Pâté aux pommes de terre Borbonnais, Marco et Eric, ainsi que l'équipe Capteur, Christelle, Jérôme, Amadou et Paul.

Merci Antoine pour les bons moments de sciences passés ensemble et pour cette magnifique expérience des journées de la science qui m'auront valu la meilleure des lettres jamais reçue. Un

remerciement tout particulier pour Françoise et Cyrille. Vous m'avez beaucoup aidé sur les démarches administratives qui parfois sont dignes des 12 travaux d'Asterix, merci pour tout.

Gardons les meilleurs pour la fin : Gabin et Charly, les fiers solides. Tous ces moments partagés en votre compagnie au laboratoire sont précieux et grâce à la Science nous avons pu développer une sincère amitié. Les moments d'amitiés auront d'ailleurs été nombreux pendant la thèse. Merci énormément Quentin et Charlène, Chloé, Erwan, Mathilde, Loïc, Alexis et Alexandre (vive le TdV!).

Cet accomplissement n'aurait jamais été possible sans le soutien indéfectible de ma famille. Une pensée émue va à mes chères grand-mères : ce travail de thèse leur est dédié. Merci beaucoup Maman d'avoir cru en moi et d'avoir été à l'écoute même dans les moments difficiles, merci Papa pour ton engouement pour mes projets.

Enfin, merci Valériane de partager ma vie, d'avoir trouvé les mots justes pour m'aider dans cette quête. Tu m'as poussé à donner le meilleur de moi-même et ta présence au quotidien m'est inestimable.

Je finirais cette page de remerciements pour souhaiter bon courage aux étudiants qui seraient amenés à lire ce manuscrit. Il a été construit en gardant à l'esprit qu'un jour, un stagiaire aurait bien besoin de savoir pourquoi les excitons de GaN sont passionnant à étudier ! J'ai essayé de développer le contenu de la façon la plus pédagogique possible en posant le contexte et en justifiant chacun des éléments étudiés. Le parcours universitaire est beau et je vous souhaite de profiter à tout instant de vos explorations scientifiques.

Table of contents

Dedications

Acknowledgments

Introduction	1
I Gallium nitride	5
I.1 A brief history of gallium nitride	5
I.2 Crystallographic properties	5
I.3 Growth	6
I.4 Structural properties	8
I.4.1 Elasticity and stress constants	8
I.4.1.1 c-axis growth	9
I.4.1.2 m-axis growth	9
I.4.2 Thermal conductivity	10
I.4.3 Vibrational properties	10
I.5 Electronic properties	12
I.5.1 Spontaneous polarization and piezoelectricity	12
I.5.2 Band Structure	13
I.5.3 Effective masses	15
I.6 Optical properties	17
I.6.1 Introduction to excitons	18
I.6.2 Hydrogen model of the Wannier-Mott exciton	19

I.6.3	Excitons in GaN	20
I.6.4	Dielectric constant and oscillator strength	22
I.6.4.1	Local Model	23
I.6.4.2	Non Local Model	24
I.7	Light-Matter Interaction	25
I.7.1	Refractive index	25
I.7.2	Bandgap Renormalization	26
I.7.3	Introduction to the Mott transition	27
I.7.3.1	Debye-Hückel Model	28
I.7.3.2	Thomas-Fermi Model	28
I.7.3.3	Versteegh Model	29
I.7.4	Strong coupling	30
I.7.4.1	Bose-Einstein Condensate	31
I.7.4.2	Polariton Lasing	33
I.7.4.3	State of the art of polariton laser	35
I.8	GaN based lasers and interest of nanowires	35
I.9	Conclusion	36
II	Experimental techniques	39
II.1	Optical spectroscopy	39
II.2	Photoluminescence and reflectivity	40
II.2.1	Photoluminescence principle	40
II.2.2	Optical recombinations	43
II.2.2.1	Localized level-band recombinations	44
II.2.2.2	Recombination of donor-acceptor pairs	45
II.2.2.3	Bound excitons recombination	45
II.2.2.4	Free excitons recombination	46
II.2.3	Reflectivity	47
II.3	Experimental setup	48
II.3.1	Micro-photoluminescence	49
II.3.1.1	Objectives	50

II.3.1.2	Spectrometer	51
II.3.1.3	Laser sources	51
II.3.2	Gaussian spot size determination	52
II.3.3	Real-space imaging	52
II.3.4	Fourier imagery	54
II.4	Time-resolved optical spectroscopy	55
II.4.1	Principle	55
II.4.2	Experimental setup	55
II.4.2.1	Laser source	55
II.4.2.2	Streak camera	56
II.5	Conclusion	57
III	Determination of the excitonic Mott density in a GaN bulk sample	61
III.1	Context: excitonic binding energy scaling law	61
III.2	Sample presentation	62
III.2.1	Bulk GaN reference sample : H46-2	62
III.2.2	Temperature study	63
III.3	Excitonic Mott transition	66
III.3.1	Photoluminescence as a function of excitation intensity	66
III.3.2	Electronical temperature	67
III.3.3	Time resolved photoluminescence	70
III.3.4	Determination of the injected carriers density	70
III.3.5	Study of the redshift as a function of the carrier density	73
III.3.6	Bandgap renormalization	74
III.3.7	Versteegh model and excitonic fraction determination	75
III.3.8	Temperature influence on Mott transition	77
III.4	Results discussion	78
III.4.1	Inhomogeneities of the carrier distribution	79
III.4.2	Carrier distribution in the presence of a bi-molecular recombination term	80
III.4.2.1	Solution by the numerical method	80
III.4.2.2	Results	84

III.4.3	Influence of the bi-molecular recombination term	86
III.4.3.1	Context	86
III.4.3.2	Fit with the term bi-molecular recombination	87
III.4.3.3	Estimation of the bi-molecular recombination term	89
III.5	Conclusion	91
IV	Spectroscopy of single core-shell nanowires	95
IV.1	Sample presentation	96
IV.1.1	CC0414	96
IV.1.2	CC0287a	98
IV.2	Optical characterization of a single nanowire	100
IV.2.1	Power study	100
IV.2.1.1	Continuous excitation	100
IV.2.1.2	Pulsed excitation	102
IV.2.2	Temperature study	104
IV.3	Single nanowire time-resolved spectroscopy	107
IV.3.1	Single nanowire TRPL at 5K	107
IV.3.2	Influence of temperature on decay times	108
IV.4	Spectroscopy of a single n-i-p core-shell nanowire structure designed for electrical injection	110
IV.5	Laser effect in a nanowire	114
IV.5.1	Experimental characteristics of the laser effect	114
IV.6	Conclusion	118
Conclusion		121
Bibliography		125
Bibliography	125

Introduction

Interest in nitride-based semiconductors for optoelectronics has constantly grown over the years. This success is due to the remarkable properties of the material: (i) direct bandgap structure used for optical devices based on (Al,In,Ga)N alloys, which allows for a spectrum of applications from visible to ultraviolet in emission and detection [1]; (ii) significant excitonic binding energies and oscillator strengths, leading to a relative robustness of excitons at high temperature [2]; (iii) well controlled doping and growth [3]. The fabrication of devices such as light emitting diodes (LEDs) and lasers have made it the first III-V material in terms of industrial share in a wide range of wavelengths (white, green, blue, and ultra-violet).

Historically, the GaN material is known for its high hardness and its very high melting point making it a good candidate for electronic devices operating at high temperatures and high frequencies. Unfortunately, the large amount of crystalline defects and the difficulties to grow this material associated with the p-doping barrier that had yet to be overcome, had blocked the understanding of the physical phenomena involved in this semiconductor and delayed the realization of electronic devices.

The work of Amano et al lead to the development of the first light-emitting diode (LED) [4] and its implementation by Nakamura et al. a few years later [5] have largely contributed to the development of research related to nitrides and especially GaN-based components such as GaN, InGaN, AlGaN. It is in this historical context that the development of the industrialization of nitrides and the research related to the knowledge of the fundamental physical properties of this material is set. Since then, the market for optoelectronic components in the blue to near-ultraviolet wavelengths has grown steadily for over a decade. Since then, the development of high quality microcavities, based on the development of vertical cavity surface emitting laser diodes (VCSELs), has allowed the emergence of a new candidate for the realization of low threshold high efficiency lasers: the microcavity exciton-polariton (also called polariton).

Exciton-polaritons result from the strong coupling between the first excited states of solids (excitons) and photons. Due to their bosonic character, a gain mechanism based on stimulated relaxation by final-state occupation can trigger polariton condensation and, thus, coherent light emission, at particle densities below those conventionally encountered in edge-emitting and vertical-cavity surface emitting lasers [6]. In the context of coherent light emission from GaN-based devices, a potential

way to reduce the laser threshold is to use exciton-polaritons within the strong light-matter coupling regime [7]. The polaritonic states however are not permanent; by increasing the excitation density the number of carriers injected into the valence band increases. In the case of a bulk semiconductor, it is commonly accepted that the energy of the excitonic transition remains constant up to the Mott density, the renormalization of the band gap energy being compensated by the reduction of the binding energy of the exciton. This Mott density constitutes a critical threshold beyond which the strong coupling is lost. Polaritons progressively lose their bosonic character when their density becomes too high, and they have relatively short lifetimes. These two particularities have been a major obstacle to the establishment of a Bose-Einstein condensate of excitons.

As stated before, the research on GaN lasers, and in particular on polariton lasers, requires an in-depth and reliable knowledge of the GaN electronic properties: as excitons may have a substantial role in lowering the laser threshold, it is thus essential to investigate the conditions, in terms of particle density and temperature, under which GaN excitons can exist. This in turn will determine the possible laser gain mechanisms which may involve polaritonic relaxation stimulated by the final state occupation [6], P-band exciton interaction scattering processes [8], or standard degenerate electron-hole plasma [9].

This in-depth research is in line with the recurrent trend in the development of optoelectronic components aiming towards the lowest energy consumption and the best photonic confinement, thus opening perspectives for the realization of non-conventional optoelectronic components. As a reminder, "conventional" lasers and luminescent components such as LEDs operate in a weak coupling regime between light and matter. The advantage of the strong coupling regime is that coherent energy is exchanged between the cavity photons and the excitons of a semiconductor material. For very low scale components (below the μm), it then becomes possible to convert an electrical signal into an optical signal in order to accelerate signal and energy transmissions, allowing an all-optical processing of information.

All this history justifies the elaboration of nanowires as a new geometry designed in the aim of reducing the defects of cavities and bulk layers: good crystalline quality, reduction of dislocation densities and the use of the nanowire facets as cavity without the need of highly-reflective UV distributed Bragg reflector (DBRs) are all arguments that facilitate the use of GaN-based nanowires in the realization of polariton lasers. Moreover, structured nanowires can also be considered for the realization of devices under electric injection: to date, the growth and doping of the core-shell structure is well controlled [10, 6]. However, improvements of the structures are to be considered to optimize the p-n junction but technological and spectroscopic investigations are necessary to better consider the electrical injection in the nanowires. Consequently, the objectives of this work are divided into two main axes:

- Spectroscopy of undoped bulk GaN under optical excitation in order to experimentally evidence the Mott density at low temperature and to measure the exciton optical transitions in a reference sample. The temperature and power studies will be done with several types of optical excitation (continuous and pulsed) and will be complemented by an extensive time-resolved spectroscopy

campaign to effectively measure the carrier lifetimes in an undoped bulk GaN layer.

- Spectroscopy of nanowires under optical excitation. The aim is to study in detail the gain mechanisms involving excitons or polaritons via the exciton-photonic mode coupling. This point requires the study of the optical modes in different nanowire structure. These processes will be analyzed as a function of temperature and for various optical excitation intensities in order to precisely identify the appearance of the electron/hole plasma and the associated gain mechanism. The power densities at the laser threshold will be measured for each type of process identified: excitonic gain, polaritonic gain or via electron/hole pair recombination mechanisms.

All those objectives are essential to further understand the electrical injection, which would be the following step, performed in a first step in pulsed regime at low temperature. The polariton laser effect under continuous injection will be the ultimate goal of this work.

In the first chapter, the theoretical context presenting the structural, electronic and optical properties of GaN will be established, allowing to lay the foundation of this work necessary for the realization and the interpretation of experimental campaigns.

The second chapter will be dedicated to the presentation of the experimental techniques used during this thesis. The optical spectroscopy will be discussed in its generality and details will be provided for photoluminescence and time-resolved photoluminescence in order to proceed to the analysis and interpretation of results.

The third chapter will be dedicated to the results of different campaigns performed on a non intentionally doped bulk GaN reference sample. Micro-photoluminescence and time-resolved photoluminescence studies at temperatures ranging from 5K to 300K have been performed to characterize the optical properties of our sample. The objective of these campaigns is double, first an in depth experimental work has been done in order to establish the Mott transition and determine the domain of existence of excitons in bulk GaN and second the complete characterization of a reference sample allows to experimentally verify with updated techniques the intrinsic properties of GaN.

Finally, the fourth and last chapter will be devoted to the spectroscopy of single core-shell nanowires as a function of temperature and excitation power density. These single-wire campaigns are the result of multiple improvements of our experimental methodology allowing the realization of time-resolved photoluminescence; those results are essential in the study of gain mechanisms in nanowires for electrical injection.

Gallium nitride

I.1 A brief history of gallium nitride

Since the realization of the first transistor based on a double p-n junction in 1948 and with the development of electronics in the 1970s, scientific and industrial interest in semiconductors has grown exponentially. Initially largely dominated by the silicon industry (integrated circuits and microprocessors), the semiconductor market left more and more space to optoelectronics.

Golden age of nitride based devices began fifty years ago as in 1971 Pankove et al. published the first Gallium Nitride (GaN)-based light-emitting diode (LED) [11, 12]. Nitride based devices then went through different revolution both fundamental and industrial, culminating in 2014 with the Nobel Prize in Physics for the invention of efficient blue light-emitting diodes which has enabled bright and energy-saving white light sources, from Isamu Akasaki, Hiroshi Amano and Shuji Nakamura [13]. GaN is a III-V wide bandgap semiconductor typically used for devices requiring fast carrier transport with a high breakdown voltage and is used in a wide range of applications. This material is especially known in Light Emitting Diodes (LEDs), as well as in Field Effect Transistors (FETs) and also as the base material in AlGaN/GaN Hetero-junction Bipolar Transistors (HEBTs) [14].

I.2 Crystallographic properties

GaN is a semiconductor which belongs to the III-V group. It can crystallize in two stable phases: wurtzite (WZ) and zinc blende (ZB). The group III atom (Ga) is surrounded by four nitrogen atoms. This coordination is characteristic of a sp^3 hybridization and thus of a bond with a strong covalent character [15]. However, the ionic character of the bond cannot be neglected because of the high electronegativity of nitrogen. The most common phase found at room temperature is the wurtzite structure as it is the most thermodynamically stable.

The WZ structure belongs to the $P6_3mc$ space group in Hermann-Mauguin notation (or C_6^4v in

Schoenflies notation). The ideal crystal is made of two hexagonal lattices: one containing the gallium atoms (Ga) and the other the nitrogen atoms (N), interpenetrated and shifted along the c axis of $3/8$ th of the unit cell. The wurtzite stacking sequences along $[0001]$ can be described as: ...ABAB... for mono-layer or ...AaBbAaBb... for bi-layers as shown on figure I.1.

The WZ structure is characterized by the lattice parameters a and c . In an ideal wurtzite crystal the ratio $\frac{c}{a} = \sqrt{\frac{8}{3}} \approx 1.633$ but this value obviously changes when measured in a real structure. The main values for WZ GaN are given in the table I.1:

\	Parameters	GaN
WZ	a	3.189\AA
	c	5.185\AA
	c/a	1.626

Table I.1 – Lattice parameters if GaN in WZ Structure [17]

As WZ structure does not have inversion center, the orientations $\vec{c} = [0001]$ and $-\vec{c} = [000\bar{1}]$ are not equivalent regarding the crystal orientation. We define the polarity of the layer as Ga-polar if it is grown along \vec{c} meaning the metal-nitride bond face the surface and as N-polar if it is grown along the $-\vec{c}$ direction. The figure I.2 illustrate both metal and nitride polarities. Due to this crystalline anisotropy, the optical properties of wurtzite-type nitrides are anisotropic. This results in a uniaxial birefringence of these materials.

I.3 Growth

As the wurtzite phase is the most thermodynamically stable, this hexagonal structure represents the majority of the nitride based epitaxy. The growth is essentially performed along the c -axis, in the $[0001]$ plane however it is possible to grow along the a $[11\bar{2}0]$ and m $[1\bar{1}00]$ planes which are parallel

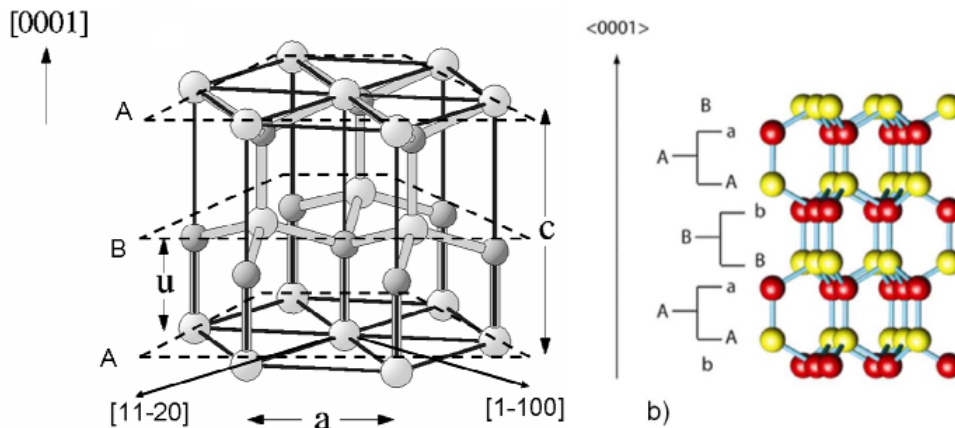


Figure I.1 – Crystalline structures wurtzite from [16] and [15]

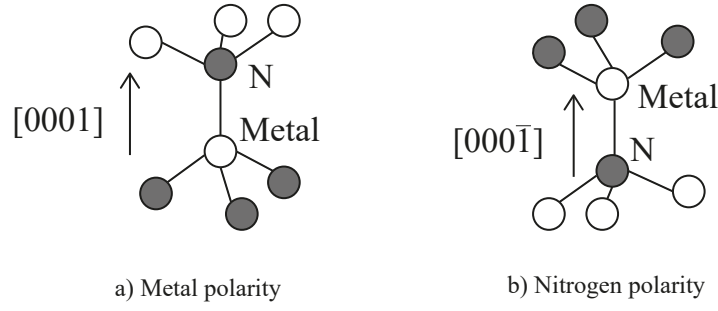


Figure I.2 – illustration of Ga-polarity and N-polarity

to the c axis and form an angle of 90 between them (figure I.3).

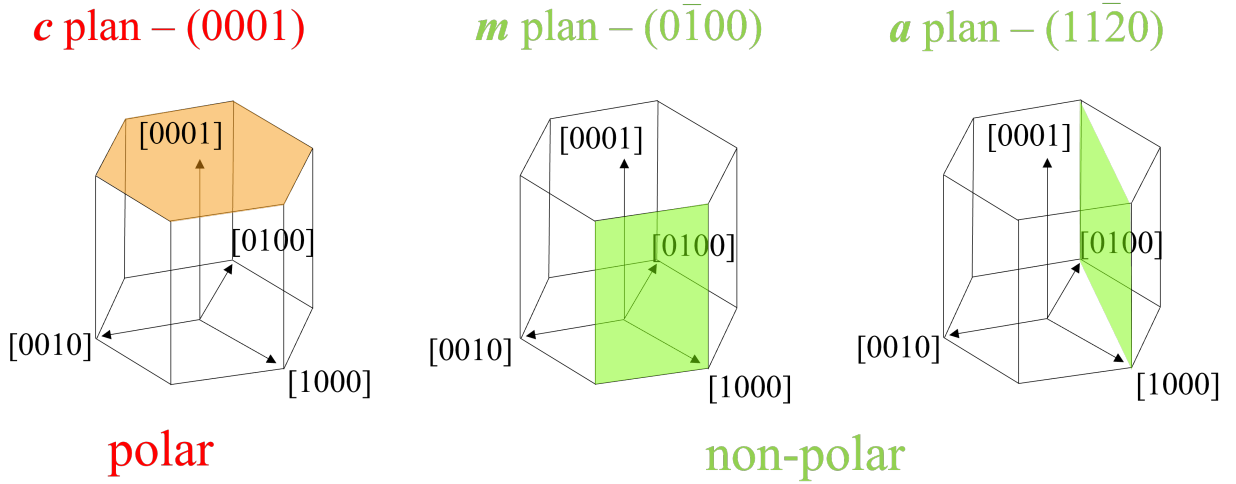


Figure I.3 – Most used planes in a wurtzite structure growth. The c plane (0001) is polar, with Ga polarity. The other planes are non-polar.

The properties of these last two planes differ from those of the c plane (optical transitions, index ...) and allow the realization of non-polar heterostructures. Nitride based semiconductors are mainly grown by heteroepitaxy techniques as the fabrication of gallium nitride wafers requires drastic conditions. The heteroepitaxy is made from a substrate of different nature : those substrates often feature different thermal expansion coefficient and induce lattice mismatches which are detrimental to the quality of the materials during the growth. At the end of the growth process, the crystal relaxes plastically and get high dislocation density. The main substrates used in epitaxy are presented in table I.2. The lattice mismatch is calculated with $\frac{\Delta a}{a} = \left(\frac{a_s - a_l}{a_l}\right) \times 100$ with a_l and a_s being the lattice parameters of the epitaxied layer and the substrate. The thermal expansion coefficient between two temperatures as function of the lattice parameter a is calculated with $\alpha_a = \frac{2[a(T_1) - a(T_2)]}{(T_2 - T_1)[a(T_1) + a(T_2)]}$ and the mismatch of coefficient of thermal expansion as $\frac{\Delta \alpha}{\alpha} = \left(\frac{\alpha_l - \alpha_s}{\alpha_s}\right) \times 100$ with α_l and α_s being the thermal expansion coefficient parameters of the epitaxied layer and the substrate. The substrate parameters are of crucial importance as they will affect the physical properties of the future sample. The most commonly used growth techniques can be classified in two categories:

- a physical deposition of matter such as molecular beam epitaxy (MBE) and physical vapor

deposition (PVD). Those techniques are based on the condensation of matter on a substrate.

- a chemical deposition such as Hydride Vapour Phase Epitaxy (HVPE) and Metal Organic Vapor Phase Epitaxy (MOCVD).

MOCVD and HVPE are preferred in industry as those techniques feature good reproducibility, high growth rates and an easier maintenance. .

Substrate	a (Å)	lattice mismatch (%)	$\alpha(10^{-6} \text{ K}^{-1})$	thermal coef. mismatch (%)
GaN (0001)	3.189	0	4.3	0
AlN (0001)	3.112	-2.4	3.0	30
sapphire (0001)	4.758	14 (30° rotation)	7.5	-441
silicon (111)	3.845	-17	2.59	40
silicon carbide 6H	3.082	3	4.7	-32

Table I.2 – Differences in lattice parameters and thermal expansion coefficients between GaN and various substrates

There is no affordable substrate with low or no lattice mismatch with GaN. It has been seen in part I.3 that the lattice mismatch between GaN and a substrate of different nature such as AlN, InGaN or sapphire is a source of strain in the 2D heterostructures generating dislocations during the plastic relaxation. These dislocations reduce the crystalline quality of the material and degrade the opto-electronic properties of the devices by increasing the number of collisions of free carriers impacting the mobility of the carriers [18] and their lifetimes. Dislocations can also contribute to a leakage current through GaN/AlN heterostructures [19] and act as non-radiative recombination centers [20]. However, other structures than planar layers can be grown in order to reduce growth induced dislocations. Due to stress relaxation by free surfaces, nanowires of element III - nitrides can be grown on substrates with high lattice mismatch. A growth without dislocation is therefore possible on low cost substrates such as Si(111) [21] or Si(100) [22].

I.4 Structural properties

The structural properties will have a direct link on the optical properties of GaN. The main structural properties that can influence the optical characterization will be detailed.

I.4.1 Elasticity and stress constants

In the elastic domain, where the deformations are not irreversible, Hooke's law allows us to relate the strain tensor $[\varepsilon]$ to the stress tensor $[\sigma]$ from the elasticity coefficients C_{ij} . This law states that the stress is proportional to the strain meaning that, the stress components are linear functions of the strain components. Since GaN has a wurtzite-like structure featuring a C_{6v} symmetry group, the

set of elastic modulus values reduces to a (6×6) matrix and the number of elastic constants reduces to six. Below are given the relations between strain and stress:

$$\begin{pmatrix} \sigma_{xx} \\ \sigma_{yy} \\ \sigma_{zz} \\ \sigma_{xy} \\ \sigma_{yz} \\ \sigma_{zx} \end{pmatrix} = \begin{pmatrix} C_{11} & C_{12} & C_{13} & 0 & 0 & 0 \\ C_{12} & C_{11} & C_{13} & 0 & 0 & 0 \\ C_{13} & C_{13} & C_{33} & 0 & 0 & 0 \\ 0 & 0 & 0 & 2C_{44} & 0 & 0 \\ 0 & 0 & 0 & 0 & 2C_{44} & 0 \\ 0 & 0 & 0 & 0 & 0 & 2C_{66} \end{pmatrix} \begin{pmatrix} \varepsilon_{xx} \\ \varepsilon_{yy} \\ \varepsilon_{zz} \\ \varepsilon_{xy} \\ \varepsilon_{yz} \\ \varepsilon_{zx} \end{pmatrix} \quad (\text{I.1})$$

Deformations along the normal axis are described by the normal strains ε_{xx} , ε_{yy} and ε_{zz} following the three orthogonal directions $[1\bar{1}10]$, $[11\bar{2}0]$, and $[0001]$. Shear strains ε_{xy} , ε_{yz} and ε_{zx} appear when the deformation is not along the three principal directions. Only normal strains are present when growing on polar or non-polar planes.

I.4.1.1 c-axis growth

When growing along the c-axis, in-plane deformations are isotropic $\varepsilon_{xx} = \varepsilon_{yy}$:

$$\varepsilon_{xx} = \varepsilon_{yy} = \varepsilon_{\parallel} = \frac{a_s - a}{a} \quad (\text{I.2})$$

Perpendicular to the growth axis:

$$\varepsilon_{zz} = \varepsilon_{\perp} = \frac{c_s - c}{c} \quad (\text{I.3})$$

With a , c the lattice parameters of the epitaxial layer and a_s , c_s the lattice parameters of the substrate.

In the case of a bi-axial stress:

$$\begin{cases} \sigma_{xx} = \sigma_{yy} = (C_{11} + C_{12} - 2\frac{C_{13}^2}{C_{33}})\varepsilon_{\perp} \\ \sigma_{zz} = C_{13}(\varepsilon_{xx} + \varepsilon_{yy}) + C_{33}\varepsilon_{zz} = 0, \text{ surface of the sample being stress free} \\ \sigma_{xy} = \sigma_{yz} = \sigma_{zx} = 0 \end{cases} \quad (\text{I.4})$$

whereby the ε_{zz} component can be expressed as a function of the ε_{xx} component:

$$\varepsilon_{zz} = -2\frac{C_{13}}{C_{33}}\varepsilon_{\parallel} \quad (\text{I.5})$$

I.4.1.2 m-axis growth

When growth is performed on the m-plane $[1\bar{1}00]$, the uniaxial symmetry of the crystal changes from C_{6v} to C_{2v} . The resulting lattice mismatch will also change and the in-plane deformation become

anisotropic. As the surface remains stress-free, we obtain the following component for σ_{yy} :

$$\sigma_{yy} = C_{12}\varepsilon_{xx} + C_{11}\varepsilon_{yy} + C_{13}\varepsilon_{zz} \quad (\text{I.6})$$

We can then express the growth axis component inside the deformation tensor by:

$$\varepsilon_{yy} = -\frac{C_{12}\varepsilon_{xx} + C_{13}\varepsilon_{zz}}{C_{11}} \quad (\text{I.7})$$

Experimental values for the elasticity coefficients C_{ij} measured by the propagation speed of sound [23] or using Brillouin scattering [24] are summarized in the table I.3

Ref	C_{11}	C_{12}	C_{13}	C_{33}	C_{44}	C_{66}
[25]	396	144	100	392	91	126
[26]	390	145	106	398	105	123
[27]	296	130	158	267	24	88

Table I.3 – Elastic constants values in wurtzite GaN (in GPa)

The strain will influence the band structure (see I.5.2) of the semiconductor and thus modify the energy of optical transitions, this subject will be further explained. Theoretical calculations using strain potentials show that the transitions are affected in GaN [28] making the position of the excitons a good indicator of the strain state.

I.4.2 Thermal conductivity

The thermal conductivity of a material is the kinetic property determined by the contributions of the degrees of freedom of the molecules. In intrinsic semiconductors, because of the low density of conduction electrons and holes, the main contribution to heat transport is dominated by lattice vibration or phonons. Of all the thermal properties, conductivity is the most affected by structural defects: the thermal conductivity values reported in bulk GaN range from 420 to 1000 $W.m^{-1}.K^{-1}$.

I.4.3 Vibrational properties

Vibrational properties are directly related to phonons and are described as the energy quantum of an elastic wave. The knowledge of the vibrational properties of a material is essential as phonons have an influence in the interaction processes with other particles. Phonons can be described as oscillations of the atoms of the crystal lattice causing a series of vibration waves to propagate in the lattice.

A wurtzite structure counts 12 phonon modes:

- one acoustic longitudinal mode (LA)
- two acoustic transverse modes (TA)

- three optical longitudinal modes (LO)
- six optical transverse modes (TO)

The vibrations can induce a relative displacement of charges, equivalent to oscillating dipoles that couple to electromagnetic waves of the same frequency. This charge displacement is how infrared radiation incident on the crystal is absorbed, its energy being used to create lattice vibrations. The energies of the optical phonons in the center of the Brillouin zone have important implications on the electronic transport properties. Their high frequencies in GaN are also indicators of the hardness of the material. Experimentally, the determination of the phonon frequencies is done by infrared or Raman spectroscopy in the center of the Brillouin zone. We will see that the vibrational properties influence the electronic and optical properties.

Temperature	A ₁ (TO)	E ₂ (TO)	E ₂ ^{high}	E ₂ ^{low}	A ₁ (LO)	E ₁ (LO)
T=6K [29]	533.8	560.2	569.0	143	736.6	744.0
T=300K [29]	531.8	558.8	567.6	144	734	741.0

Table I.4 – Phonon frequencies and energies at the center of the Brillouin zone (Γ point) in the case of wurtzite GaN in cm^{-1} ($1 \text{ cm}^{-1} = 0,124 \text{ meV}$)

Temperature	A ₁ (TO)	E ₂ (TO)	E ₂ ^{high}	E ₂ ^{low}	A ₁ (LO)	E ₁ (LO)
T=300K [29]	65.9	68.9	70.4	17.9	91	91.9

Table I.5 – Phonon energies (meV) at the center of the Brillouin zone in the case of wurtzite GaN. ($1 \text{ cm}^{-1} = 0,124 \text{ meV}$)

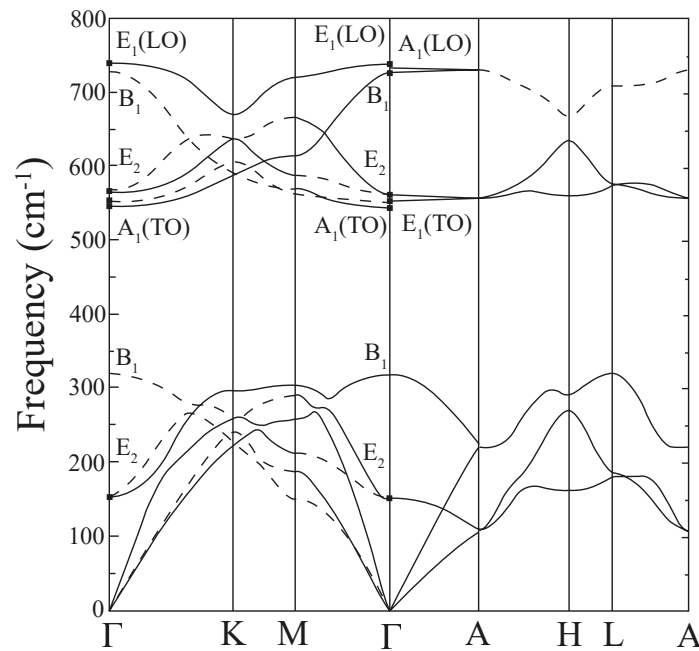


Figure I.4 – Phonon mode dispersion curves of GaN [29]

I.5 Electronic properties

The study of the band structure around the first Brillouin zone, allows us to understand the influence of the electronic properties on the optical and transport properties. The piezoelectric interactions within GaN with phonons will also have effects on the optical effects on the broadening of optical transients. In order to estimate these effects, the knowledge of the spontaneous polarization and piezoelectric tensor is useful.

I.5.1 Spontaneous polarization and piezoelectricity

It has been seen in I.2 that nitride crystals are non-centrosymmetric because of their wurtzite crystalline structure. The polarity of the Ga-N bond is induced by a strong electronegativity difference between both atoms. As a consequence, electrons are more strongly attracted by nitrogen than gallium. To keep the macroscopic neutrality the tetrahedron along the c-axis are distorted to compensate the strong ionicity of the Ga-N bonds as shown in figure I.5. Physically it can be seen by a shorter Ga-N bond in the c-axis: each tetrahedron is thus distorted along the c-axis, resulting in a macroscopic polarization for layers grown along this axis.

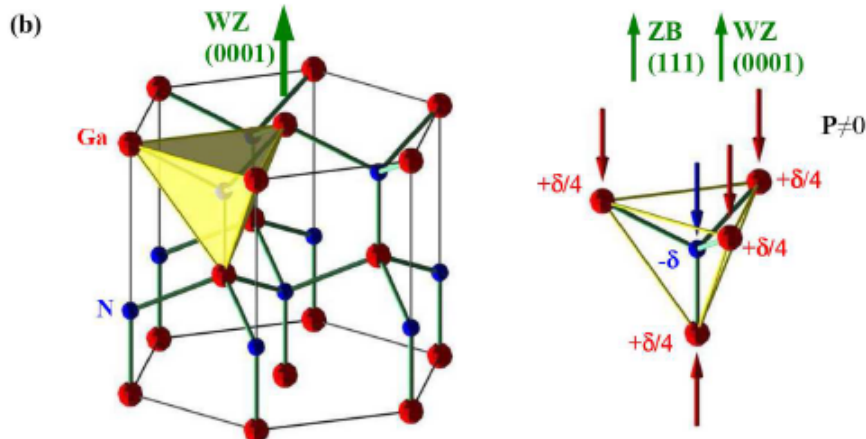


Figure I.5 – Lattice and associated deformation of the tetrahedron in case of an applied stress in the [0001] direction. The tetrahedron is not centro-symmetric thus creating a piezoelectric polarization. Extracted from [30]

Although the electronic neutrality is preserved, the distortion effect is not compensated on the first charged layer: it is the spontaneous polarization. The value of spontaneous has been evaluated by Lähnemann et al [31] and is around $-0.022 \pm 0.007 \text{ C/m}^2$. It has been seen in I.3 that GaN is affected during its growth by lattice mismatch and thermal coefficients. Moreover in the case where strain is added on a polar direction, the tetrahedron will be deformed along the axis generating an additional piezoelectric polarization.

For a wurtzite type crystal, we have the following piezoelectric tensor:

$$\begin{pmatrix} P_{xx} \\ P_{yy} \\ P_{zz} \end{pmatrix} = \begin{pmatrix} 0 & 0 & 0 & 0 & e_{15} & 0 \\ 0 & 0 & 0 & e_{15} & 0 & 0 \\ e_{31} & e_{31} & e_{33} & 0 & 0 & 0 \end{pmatrix} \begin{pmatrix} \varepsilon_{xx} \\ \varepsilon_{yy} \\ \varepsilon_{zz} \\ 2\varepsilon_{xy} \\ 2\varepsilon_{yz} \\ 2\varepsilon_{zx} \end{pmatrix} \quad (\text{I.8})$$

With P_{xx} and P_{yy} the piezoelectric polarizations along the direction perpendicular to the c-axis, P_{zz} the polarization along the c axis. The values of the different components of the piezoelectric tensor e_{ij} in the case of wurtzite GaN are given in the table I.6

	e_{31}	e_{33}	e_{15}
GaN (C.m ⁻²)	-0,33	0,65	-0,33

Table I.6 – Piezoelectric constants of GaN [32]

I.5.2 Band Structure

The first Brillouin zone shown in figure I.6 is a region of space in the reciprocal lattice. It is determined from the crystal lattice, and is defined by a set of perpendicularly bisecting planes which cross the reciprocal lattice (RL) translation vectors (connecting the nearest neighboring RL points) at their respective mid-points.

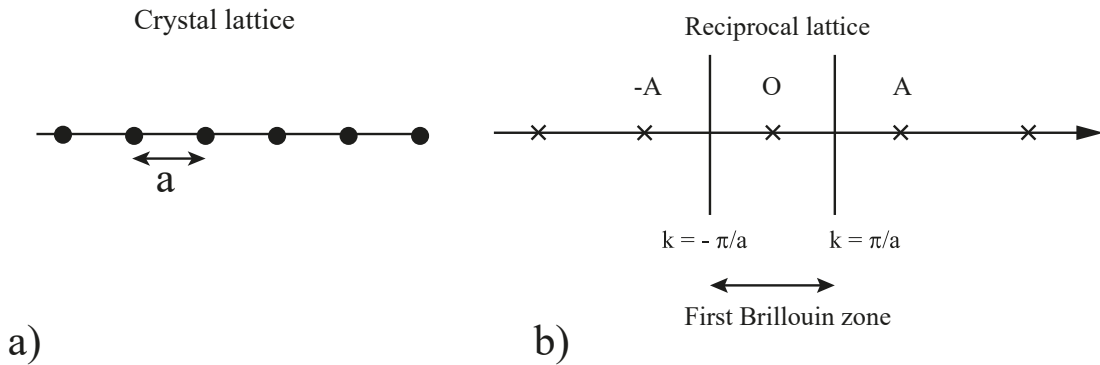


Figure I.6 – One-dimensional crystal lattice (a), and its associated reciprocal lattice (b). The translation vector for the reciprocal lattice is the vector A located at $2\pi/a$. The two perpendicular lines at the midpoints of OA and $-OA$ define the first Brillouin zone of the reciprocal lattice from [33].

Bloch's theorem means that it is not necessary to consider the whole crystal but only the unit cell of the reciprocal lattice because of the invariance of the wave functions $\phi_{ek}(\vec{r})$ by translation of an elementary vector \vec{G} of the reciprocal lattice and the periodicity of the dispersion relations. The

figure I.7 shows the first Brillouin zone for a hexagonal structure of wurtzite type. The center of the Brillouin zone $k = (0; 0; 0)$ is noted Γ .

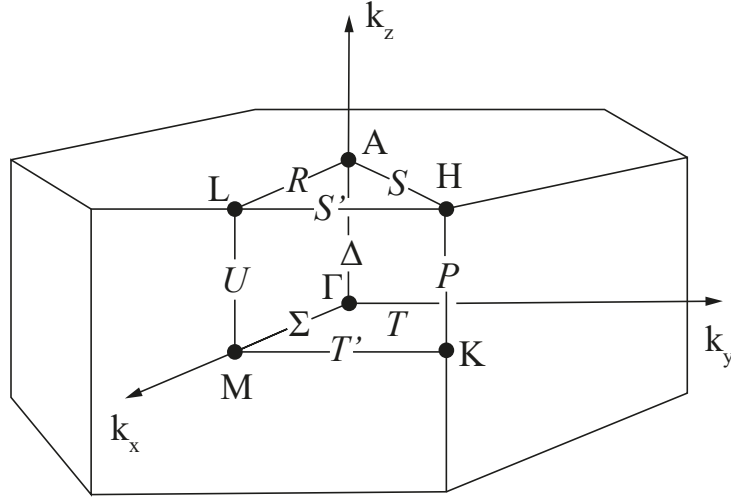


Figure I.7 – Wurtzite structure's First Brillouin zone

In an atom, the energy states are discrete and to each of these states we associate an orbital or an electronic wave function representing the probability of presence of the electron around the atomic nucleus. Orbitals can be seen as an electronic wave function and the electrons are distributed on the different energy levels while respecting the Pauli exclusion principle.

Atoms are periodically distributed on a lattice in a crystalline solid and when the distance between two atoms decreases, the electrostatic interaction modifies significantly the shape of the orbitals. The energy levels associated with these orbitals form two series of continuum that are represented by energy bands. The number of states in these bands depends on the number of atoms in the crystal while the filling of these states depends on the initial electronical occupation of the atomic orbitals. For GaN, the conduction band states originate in the s-type anti-bonding orbitals (4s orbitals of Ga^+ cations) having a zero orbital moment L . The valence band comes from 2p orbitals of N^- anions having an orbital moment $L = 1$. In GaN the bandgap E_g is direct, the conduction and valence band extrema are located at the center Γ ($k = 0$) of the Brillouin zone, the conduction band is separated from the first valence band by the band gap of width E_g . Each of these bands is spin degenerated. Taking into account the spin-orbit coupling as well as the crystal field leaves the conduction band states unchanged at $\vec{k} = 0$ while the degeneracy of the valence states is partially lifted. More precisely, there are six representations Γ_1 to Γ_6 to which are added three additional representations taking into account the spin of electrons belonging to groups Γ_7 to Γ_9 .

At Γ point, the crystal field due to the non-cubicity of the lattice induces a degenerate lifting Δ_{cr} ($\Delta_{cr} = 16$ meV [35]) into two sub-levels called heavy holes (HH) Γ_5 , a light hole band (LH) Γ_1 in the center of the zone. Finally, a split-off band (SO) is located at a smaller energy given by the spin-orbit coupling energy Δ_{so} ($\Delta_{so} = 12$ meV [35]) of heavy holes and light holes Γ_5 and Γ_7 . The spin-orbit interaction associated to the crystal field then lifts the degeneracy of the higher energy valence band giving three non-degenerate valence bands called A, B and C bands $\Gamma_7(C)$, $\Gamma_7(B)$ and

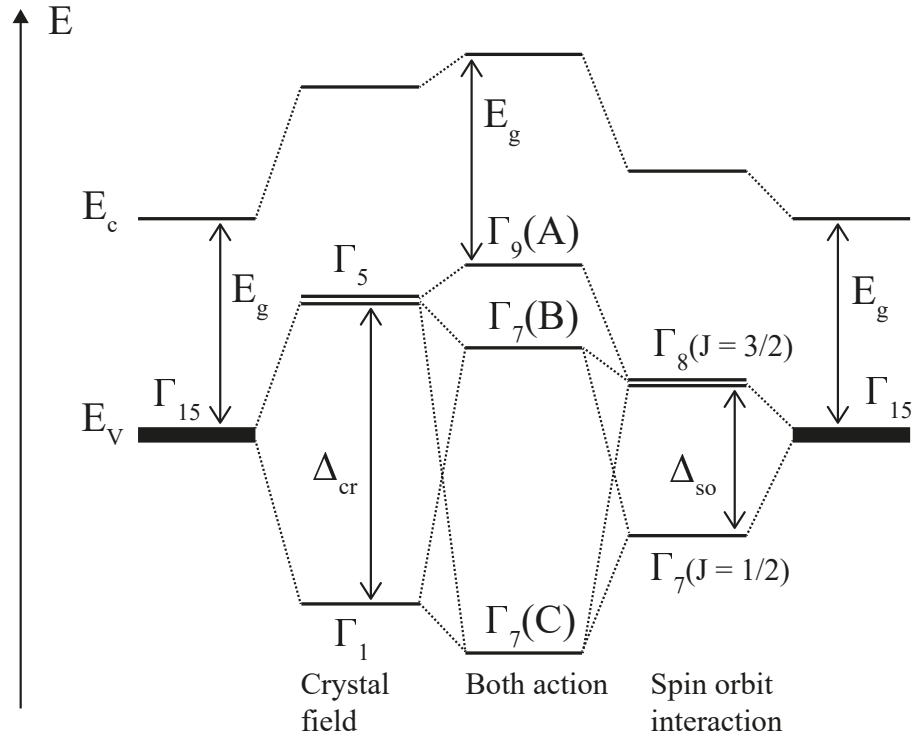


Figure I.8 – Degeneracy lifting in GaN wurtzite at the Γ point ($k = 0$) of the valence band from [34]

$\Gamma_9(A)$ as shown in Fig.I.8.

I.5.3 Effective masses

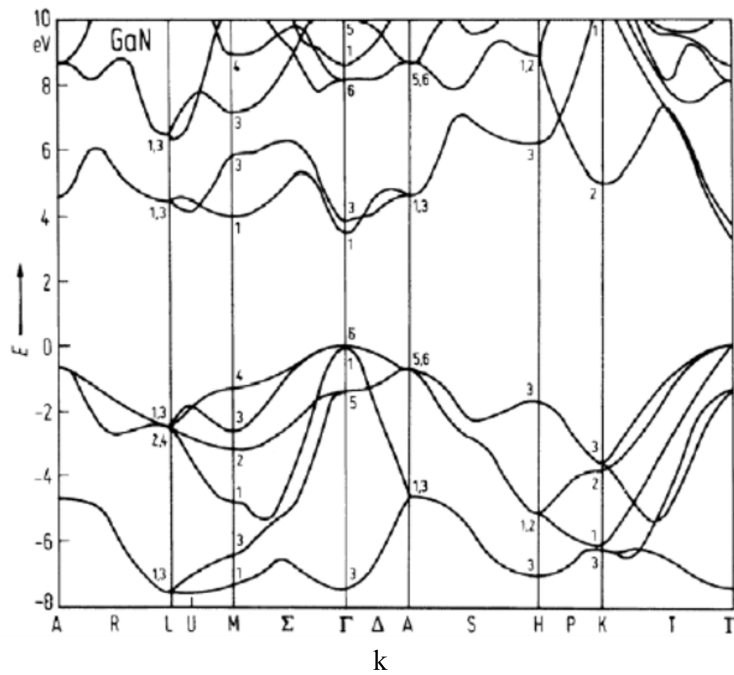


Figure I.9 – Band structure of GaN wurtzite [36]

An electron behavior inside the conduction band is a particle of mass m_0 and charge $-e$ in a crystal potential $V(\vec{r})$ formed by the action of other particles in the crystal. By introducing an effective mass m_e , the electron is considered as a quasi-particle subjected only to external forces. Thus, the interactions with ions and other electrons in the crystal are taken into account through the effective mass. An electron in motion in a semiconductor, is assimilated to a particle of mass m_e in vacuum subjected to an external electric force.

As shown in fig.I.9 the bands of semiconductors tend to be parabolic in the vicinity of the band extrema at the Γ point. These extrema are most important for the optical and transport properties. The effective masses are constant in these regions as shown in fig. I.10. Thanks to this concept, an

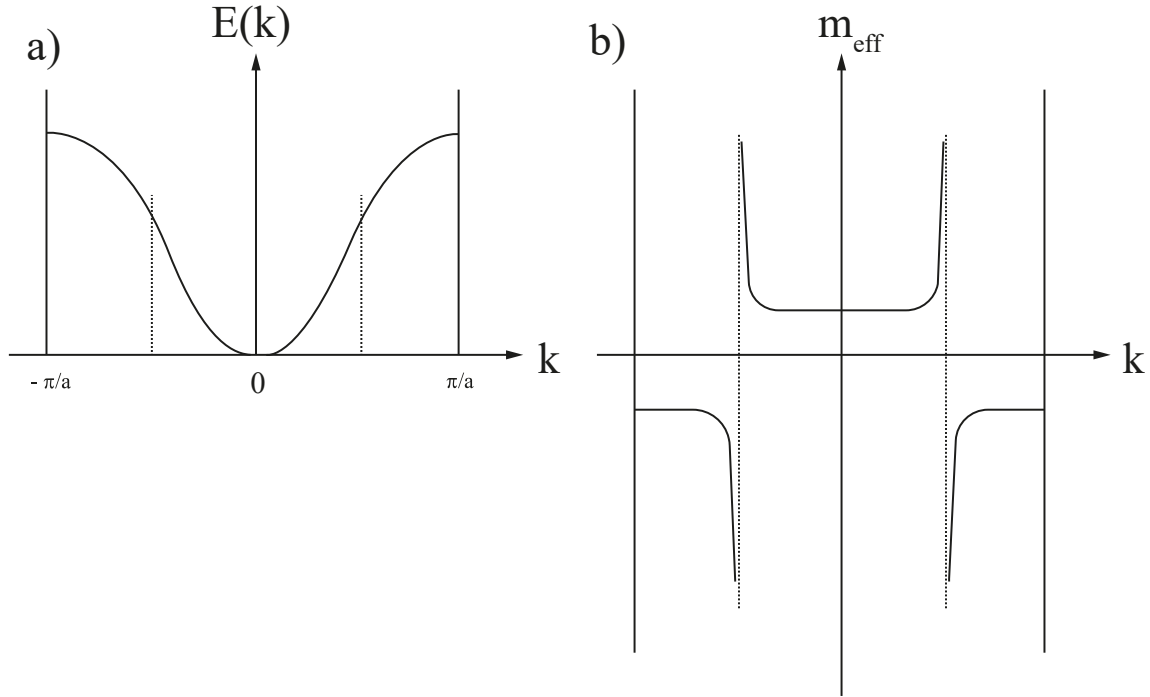


Figure I.10 – Schematic dispersion (a) of a conduction band and the resulting effective mass (b) in a one-dimensional crystal lattice from [37]

electron moving in a semiconductor is assimilated to a particle of mass m_e in vacuum subjected to an external electric force.

$$\vec{F}_e = m_e \frac{d\vec{v}}{dt} \quad (\text{I.9})$$

The kinetic energy theorem is used to express the energy $E(\vec{k})$ as function of the work of the electric force \vec{F}_e and the group speed \vec{v}_g such as:

$$dE(\vec{k}) = \vec{F}_e \cdot \vec{v}_g dt = \vec{F}_e \cdot \left(\frac{1}{\hbar} \frac{dE(\vec{k})}{d\vec{k}} \right) dt = \frac{dE(\vec{k})}{d\vec{k}} d\vec{k} \quad (\text{I.10})$$

By comparison with Newton's law, we obtain two equivalent expressions of the force \vec{F}_e .

$$\vec{F}_e = m_e \vec{a} = \hbar \frac{d\vec{k}}{dt} \quad (\text{I.11})$$

We can then calculate the acceleration \vec{a} as the derivative with respect to time of the group velocity \vec{v}_g :

$$\vec{a} = \frac{d\vec{v}_g}{dt} = \frac{1}{\hbar} \frac{\partial^2 E}{\partial k \partial t} = \frac{1}{\hbar} \frac{\partial^2 E}{\partial k^2} \frac{d\vec{k}}{dt} = \frac{1}{\hbar^2} \frac{\partial^2 E}{\partial k^2} \vec{F}_e \quad (\text{I.12})$$

By analogy with the formula I.11, it is possible from I.12 to obtain the expression of the effective mass of the electron which is proportional to the inverse of the second derivative of the energy in \vec{k} space:

$$\frac{1}{m_e} = \frac{1}{\hbar^2} \frac{\partial^2 E}{\partial k_i \partial k_i} \quad \text{with} \quad i, j = x, y, z \quad (\text{I.13})$$

Therefore we can also state as a rule of thumb, that narrow gap semiconductors tend to have small effective masses and wide gap semiconductors tend to have carriers with larger effective masses. In the context of optical transitions we consider mainly the Γ point where the dispersion $E(\vec{k})$ is supposed to be parabolic, which leads to a constant effective mass m_e . In the same way, it is possible to define effective masses m_h for the holes, corresponding to each of the three valence bands and generally higher than for the electron. The concept of effective masses is strongly present in the analysis of optical and electronic properties, in particular during the analysis of optical transitions detailed later.

I.6 Optical properties

The structural and electronic properties previously presented can influence the optical properties of a semiconductor. The optical properties of a semiconductor are mainly due to the interactions between photons and electrons. These interactions have a considerable impact on the dielectric function when the energy of the photons is equal to the energy difference between two electronic states.

The fundamental state of a semiconductor ($E = 0$ and $\vec{k} = 0$) is defined when the valence band is fully occupied and the conduction band empty. The excitation of the material by photons of energy higher than the gap of the semiconductor will induce an absorption phenomenon: an electron will then pass into the conduction band. The electron defect in the valence band can be represented by a pseudo-particle of opposite charge to the electron, called hole as shown in fig I.11. The two quasi-particles are annihilated during the recombination process. A coulombic interaction is possible between the hole and the electron forming a composite quasi-particle seen as a system similar to the hydrogen atom: the exciton.

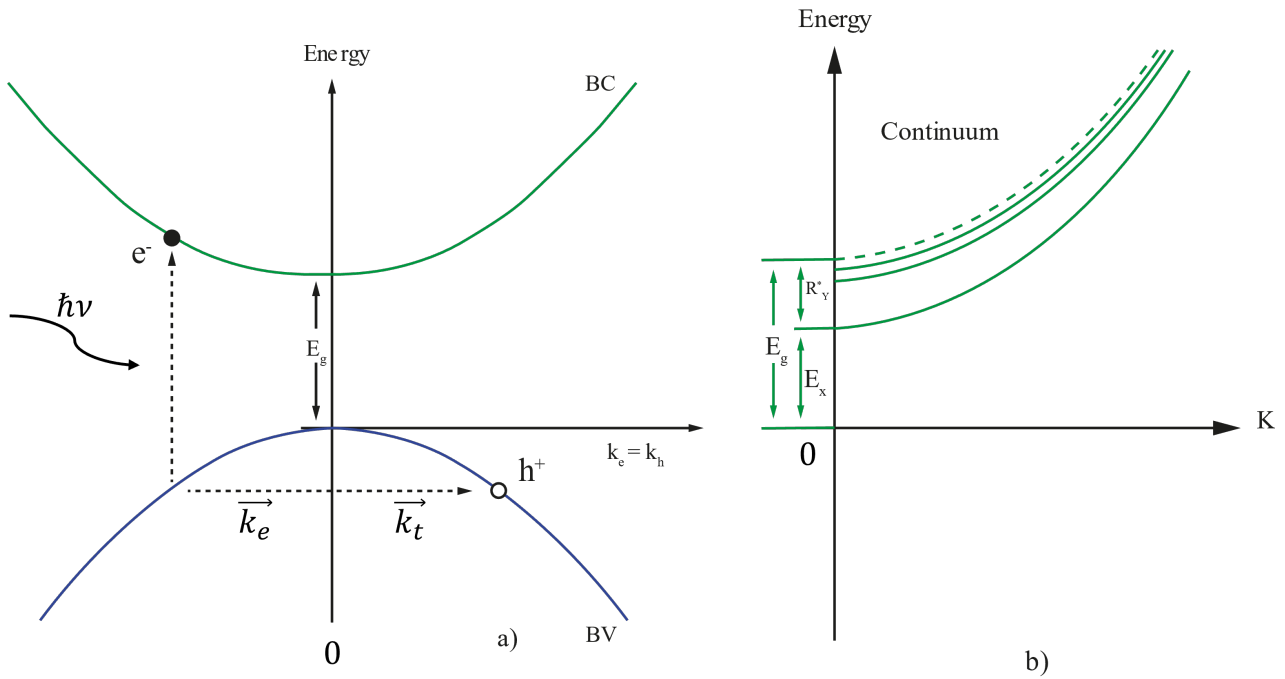


Figure I.11 – Electron-hole pair (a) in a valence and conduction band diagram and (b) in a representation of the exciton

I.6.1 Introduction to excitons

Excitons can be described as an N-body problem. The exciton arises from the Coulombic interaction between the N-1 electrons of the valence band and the electron of the conduction band. The crystal potential of the semiconductor includes a correlation exchange component that describes the energy that can be gained by the correlated movement of electrons between them. This potential has the effect of increasing the average distance between two electrons and thus reduces the Coulombic energy due to electron-electron interactions [33]. Thus, in most semiconductors, the exciton can be described, in the effective mass approximation, by the interaction of a hole of mass m_h and charge $+e$ with an electron of mass m_e and charge $-e$.

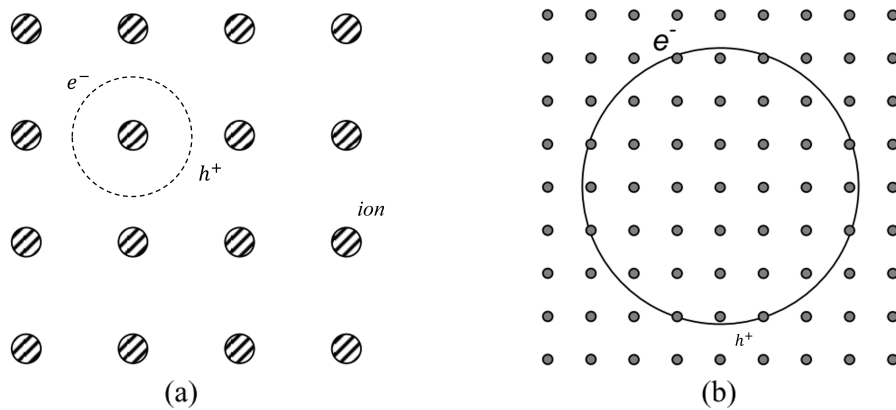


Figure I.12 – Schematic representation of Frenkel excitons (a) and Wannier excitons (b)

As seen on Figure I.12, we distinguish two extreme states of excitons in semiconductors and insulators:

- Frenkel excitons [38] where the electron-hole distance is comparable to the crystal lattice periodicity featuring a very strong electron-hole attraction as the exciton is located inside the elementary cell
- Wannier-Mott excitons [39, 40] which are much larger than the lattice size due to the electrostatic screening of an electron.

For most inorganic semiconductors, including GaN, the coulombic interactions are screened by the correlated motion of all other valence electrons in the valence band. The orbits of the electron and the hole around their center of masses are wider than the unit cell of the crystal lattice.

I.6.2 Hydrogen model of the Wannier-Mott exciton

The properties of this pseudo-particle can be modeled using the formalism of the hydrogenoid model in the framework of the envelope function approximation. For this purpose, we use the effective mass approximation and assume the isotropy of the valence and conduction bands.

$$E_c(\vec{k}) = E_g + \frac{\hbar k^2}{2m_e} \quad \text{and} \quad E_v(\vec{k}) = -\frac{\hbar k^2}{2m_h} \quad (\text{I.14})$$

E_c, E_v being the conduction and valence band energies, m_e, m_h being the effective masses of conduction band and valence band. The envelope function of the exciton is the solution of the Schrödinger equation :

$$\left[-\frac{\hbar^2}{2m_e} \vec{\nabla}_{\vec{r}_e}^2 + -\frac{\hbar^2}{2m_h} \vec{\nabla}_{\vec{r}_h}^2 - \frac{e^2}{4\pi\epsilon |\vec{r}_e - \vec{r}_h|} \right] \psi(\vec{r}_e, \vec{r}_h) = (E - E_g) \psi(\vec{r}_e, \vec{r}_h) \quad (\text{I.15})$$

The first two terms of equation I.15 correspond to the kinetic energy terms of the electron and the hole.

The third term of equation I.15 is the coulombic interaction between the electron and the hole; e is the elementary charge, \vec{r}_e et \vec{r}_h the positions of the electron and the hole. $\epsilon = \epsilon_0\epsilon_r$ is the static dielectric constant, it allows us to take into account the screening effects due to the electrons of the valence band. In order to determine the total energy of the exciton we dissociate :

The movement of the center of mass, of coordinate

$$\vec{R} = \frac{m_e \vec{r}_e + m_h \vec{r}_h}{m_{ex}}$$

The total energy of the excitons E_R is then equals to :

$$E_R = E_g + \frac{\hbar^2 K^2}{2m_{ex}}$$

where E_g is the band gap energy, $m_{\text{ex}} = m_e + m_h$ is the weight of the exciton of \vec{K} wave vector.

The relative motion of the electron with respect to the hole is treated by introducing the vector $\vec{r} = \vec{r}_e - \vec{r}_h$ and the reduced mass μ as $\frac{1}{\mu} = \frac{1}{m_e} + \frac{1}{m_h}$. This system is analogous to the one of the hydrogen atom. The energy, $E_r(n)$ is then quantized, n being the quantum number:

$$E_r(n) = -\frac{E_b}{n^2}$$

where $E_b = 13,6 \frac{\mu/m_0}{\epsilon_r^2}$ (eV) is the binding energy of the exciton in its ground state and m_0 is the mass of the electron at rest.

The total energy of the exciton of quantum number n is then given by :

$$E_n = E_g + \frac{\hbar^2 K^2}{2m_{\text{ex}}} - \frac{E_B}{n^2} \quad (\text{I.16})$$

From the hydrogenoid model, it is also possible to determine the Bohr radius of the exciton a_B , associated with the spatial extension of the excitonic wave function. In the case where $n = 1$ (1s orbital) the expression of the Bohr radius is given by the relation

$$a_B = a_H \cdot \frac{\epsilon_r}{\mu/m_0} \quad (\text{I.17})$$

with $a_H = 0,529\text{\AA}$, the Bohr radius of the hydrogen atom.

For comparison, several binding energies have been reported in Table I.7

	CuCl	CuBr	ZnO	AlN	ZnS	CdS	GaN	ZnSe	CdTe	GaAs
$E_b(\text{meV})$	190	108	60	55	38	29	25	20	11	4.2

Table I.7 – Excitonic binding energy for some inorganic semiconductors [41, 42, 43, 44, 45, 46, 47, 48, 49, 2, 50],

I.6.3 Excitons in GaN

As seen in I.5.2, GaN has three excitons A, B and C each formed from an electron of the conduction band and a hole of the valence band A, B or C. The different binding energy of excitons A, B and C are reported in the table I.8.

Bohr radii are calculated from the equation I.17 where μ is the reduced mass such as $1/\mu = 1/m_e + 1/m_h$, m_e the electron mass and m_h the hole mass and $\mu = 0.13(m_0)$ [55], $\epsilon_r \approx 9,9$ and are equal to 29.3\AA , 29.4\AA , and 27.1\AA , respectively [46, 56].

Experimentally not all excitonic transitions will be observed. From the symmetries of the valence bands, determined previously in part I.2, it is possible to establish selection rules governing the

$E_b(X_A)$	$E_b(X_B)$	$E_b(X_C)$	Ref.
$24, 8 \pm 0, 1$	$24, 7 \pm 0, 1$	$26, 8 \pm 0, 1$	[46]
$21 \pm 0, 1$	$21 \pm 0, 1$	$23 \pm 0, 1$	[51]
20	18, 5	—	[52]
22	22	—	[53]
26	—	—	[54]

Table I.8 – Experimental values of the binding energies of the GaN excitons X_A , X_B , and X_C expressed in meV

excitonic transitions. The representation of an exciton is the product of the representation of the hole of the valence band, the electron of the conduction band and the envelope function which, for the exciton in the fundamental state ($n = 1$) is symmetrical.

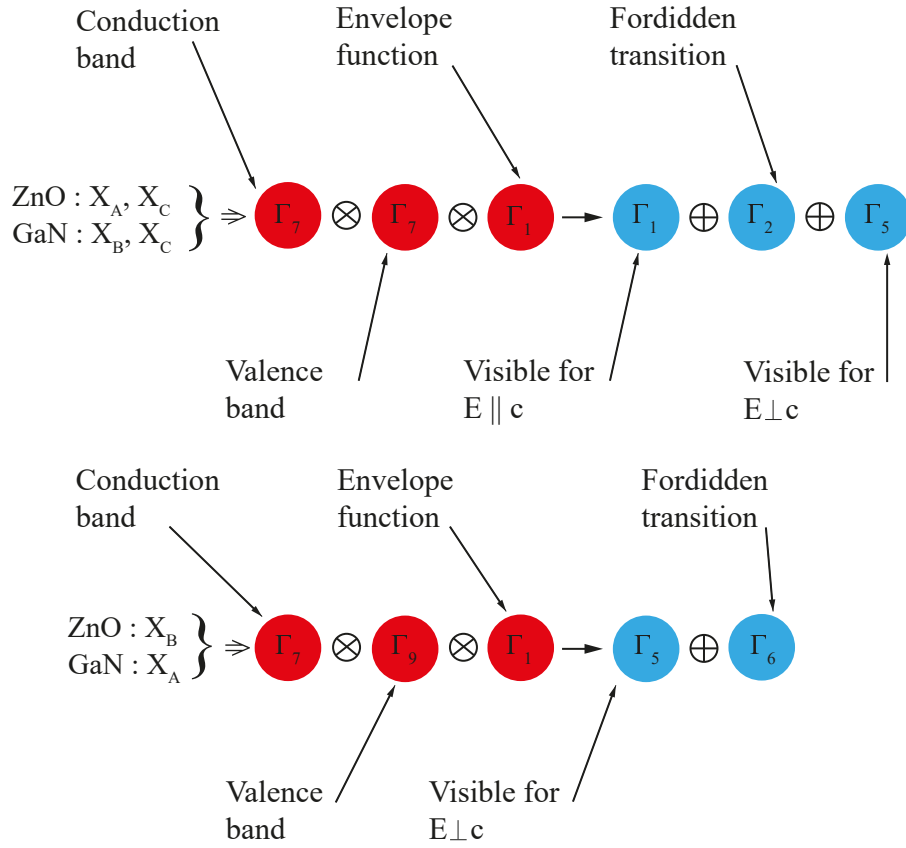


Figure I.13 – Representation of GaN and ZnO excitons [57]

By following these rules we can predict that excitons A and B will be visible in TE polarization ($\vec{E} \perp \vec{c}$) while exciton C will be visible only in TM polarization ($\vec{E} \parallel \vec{c}$). The probability of observing the C exciton transition in TE polarization is not very high. This probability is equivalent to the oscillator strength of the considered optical transition whose properties will be stated in part I.6.4. Table I.9 shows interband transition matrix elements for GaN A, B and C excitons in GaN and table I.10 summarizes the different transitions and their respective probabilities.

Exciton	$\vec{E} \perp \vec{c}$	$\vec{E} \parallel \vec{c}$
A	0.5	0
B	0.44	0.12
C	0.06	0.77

Table I.9 – Interband transition matrix elements for GaN A, B and C excitons in GaN, normalized to the sum of the A, B and C matrix elements for TE polarization - extracted from figure 7 of [58]

Exciton	authorized transition	Polarization	Probability of transition
A(Γ 5)	Yes	$\vec{E} \perp \vec{c}$	High
A(Γ 6)	No	—	—
B(Γ 1)	Yes	$\vec{E} \parallel \vec{c}$	Low
B(Γ 2)	No	—	—
B(Γ 5)	Yes	$\vec{E} \perp \vec{c}$	High
C(Γ 1)	Yes	$\vec{E} \parallel \vec{c}$	High
C(Γ 2)	No	—	—
C(Γ 5)	Yes	$\vec{E} \perp \vec{c}$	Moderate

Table I.10 – Selection rules for strain-free c-plane bulk GaN

I.6.4 Dielectric constant and oscillator strength

The response of a material to a light excitation (electric field \vec{E}) is governed by its dielectric function $\epsilon(\omega)$. In the vicinity of an excitonic resonance, the strong interaction between the exciton and the photon induces a notable variation of the dielectric constant and of the refractive index and the absorption coefficient.

The response of a semiconductor to a light excitation assimilated to an electric field \vec{E} in a system which is neutral, linear, homogeneous, isotropic and non-magnetic ($\mu_r = 1$) is represented by the electric induction field \vec{D} such that :

$$\vec{D}(\omega, \vec{k}) = \epsilon_0 \epsilon(\omega, \vec{k}) \vec{E}(\omega, \vec{k}) \quad (\text{I.18})$$

ϵ_0 being the permittivity of vacuum and $\epsilon(\omega, \vec{k})$ the complex dielectric function. For energies close to the band gap energy, the response of the semiconductor to a light wave is strongly influenced by the presence of excitons but also by the band-to-band absorption. The expression of the excitonic dielectric function can be considered through the local model where the spatial dispersion is neglected or through the non local model taking into account the spatial dispersion. We will see in a last part how to add to the dielectric function the contribution of the band-to-band absorption.

I.6.4.1 Local Model

In the local model the dielectric function does not depend on the wave vector k . The excitons are assimilated to a harmonic oscillators of mass m_{ex} , of resonance pulsation ω_0 , excited by the electric field $\vec{E} = \vec{E}_0 e^{i(\omega t - \vec{k} \cdot \vec{r})}$. The position of the oscillator will be marked by the vector \vec{u} characteristic of the deviation from equilibrium. The local model is based on the assumption that the response at a point in space depends only on the properties at that point. In a neutral, linear, homogeneous, isotropic and non-magnetic ($\mu_r = 1$) system, the electromagnetic wave will induce a polarization within the material such as:

$$\vec{P}(t, \omega) = -eN\vec{u} = \epsilon_0\chi_e\vec{E}$$

where e is the charge of the electron and N the number of oscillating elements per unit volume. χ_e is the electrical susceptibility, and is related to the dielectric function by the relation: $\epsilon = 1 + \chi_e$, it is then possible to determine the electrical susceptibility from \vec{u} and based on the fundamental principle of dynamics.

$$m_0 \frac{d^2\vec{u}}{dt^2} = -m_0\omega_0^2\vec{u} - m_0\Gamma \frac{d\vec{u}}{dt} - e\vec{E} \quad (\text{I.19})$$

where Γ corresponds to the energy absorption (fluid friction of force). The dielectric function has then the following expression :

$$\epsilon_{\text{ex}}(\omega) = 1 + \frac{Ne^2}{m_0\epsilon_0(\omega_0^2 - \omega^2 + i\Gamma\omega)} \quad (\text{I.20})$$

In the relation I.20, the term $Ne^2/(m_0\epsilon_0)$ is responsible for the coupling between the electric field and matter. This term was obtained from a purely classical method. In the case of semiconductors, this term is proportional to the square of the optical matrix element. In a quantum approach, and when the transition between the excitonic $|\Psi_{\text{ex}}\rangle$ state and the final $|0\rangle$ state is allowed, the expression of this term then becomes :

$$|H_{\text{ex}}|^2 = |\langle \Psi_{\text{ex}} | H | 0 \rangle|^2 \quad (\text{I.21})$$

where H is the interaction Hamiltonian. The dielectric function for all optical excitonic transitions of a semiconductor is then:

$$\epsilon_{\text{ex}}(\omega) = \epsilon_b + \sum_j \frac{f_j}{(\omega_{0j}^2 - \omega^2 + i\Gamma_j\omega)} \quad (\text{I.22})$$

where ϵ_b is the non-resonant dielectric function, f quantifies the coupling of an excitonic transition to the electric field, f is commonly called the oscillator strength.

j refers either to the exciton A, B or C in its ground state but also their excited states. In the case of the excited states, the oscillator strength of the level n , in the case of the hydrogen model, is equal to :

$f_j^n = f_j^{n=1}/n^3$. We can deduce from the expression I.21, that the energy distribution of the oscillators is a Lorentzian of width at half maximum Γ . For this reason, the Γ term is called homogeneous broadening. It is caused by the interactions of excitons with other particles like phonons, impurities, or other excitons. The density of phonons increasing with the temperature, the homogeneous broadening will also increase with the rise of the temperature. Note that due to the selection rules the value of the oscillator strengths depends on the polarization of the electromagnetic wave with respect to the c axis. Moreover, GaN is anisotropic, so the value of the off-resonance dielectric function ϵ_b also depends on the polarization of the electromagnetic wave. It is then clear that the expression of the total dielectric function depends on the angle between the c axis and the polarization of the electromagnetic wave.

When the material is inhomogeneous (dislocations, thickness or stress inhomogeneities), the consideration of an inhomogeneous broadening is inevitable. In this case, we consider a Gaussian distribution of harmonic oscillators similar to those described by equation I.22, whose energy is centered on $\hbar\omega_0$ and of standard deviation σ . As a reminder, the width at half maximum of a Gaussian is equal to : $2\sigma\sqrt{\ln 4}$. The expression of the dielectric function is then given by :

$$\epsilon_{\text{ex}}(\omega) = \epsilon_b + \sum_j \int \frac{1}{\sqrt{2\pi}\sigma_j} \frac{f_j}{\omega_{0j}^2 - \omega^2 + i\Gamma_j\omega} \exp\left(-\frac{(x - \omega_{0j})^2}{2\sigma_j^2}\right) dx \quad (\text{I.23})$$

where x represents the resonance energy of the excitons. This broadening is related to the crystal quality and does not depend on the temperature. In many materials it dominates over the homogeneous broadening only at low temperature. Experimentally, measurements at 5K will be necessary to estimate σ .

I.6.4.2 Non Local Model

One of the assumptions of the model detailed in the previous section is the locality, this one leads to a model which does not take into account the spatial dispersion and thus the mass of the excitons. A non-local model can be useful to interpret experimental observations [59, 60]. Hopfield and Thomas have thus developed a dispersive model [61]. In the classical model used previously, to take into account the dispersive effects, it is sufficient to link the oscillators together.

The dielectric function is then expressed as :

$$\epsilon_{\text{ex}}(\omega, k) = 1 + \sum_j \frac{f_j}{(\omega_{0j}^2 - \omega^2 + B_j k^2 + i\Gamma_j\omega)} \quad (\text{I.24})$$

The term B_j has then the expression $B_j = \frac{\hbar\omega_{0j}}{m_{\text{exj}}}$ where m_{ex} is the mass of the exciton. One can note that in this case the dispersive model does not take into account the k dependence of the broadening.

I.7 Light-Matter Interaction

I.7.1 Refractive index

The optical index is influenced by the presence of excitons. First, it is possible to separate the contribution of excitons, from a basic index (excluding excitonic resonances) which does not vary with temperature (except for a translation in energy related to the decrease of the band gap energy when the temperature increases). The optical index is a parameter to know when analyzing excitons.

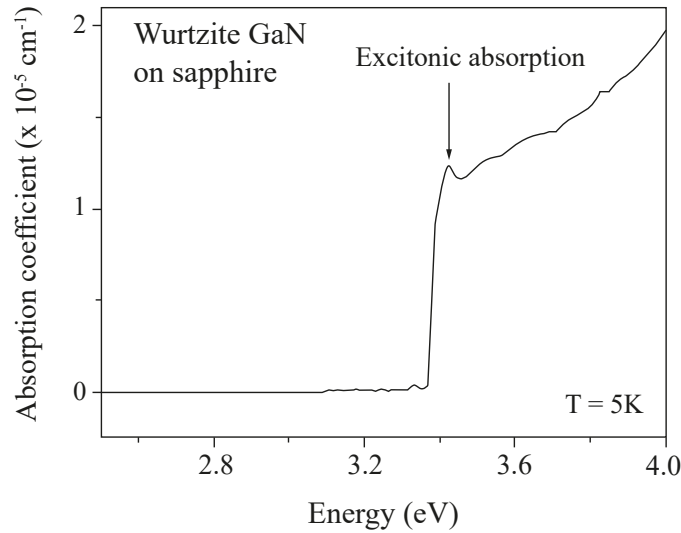


Figure I.14 – Absorption coefficient of a GaN wurtzite sample epitaxial on sapphire measured by ellipsometry at 5K [62].

Due to the crystalline anisotropy described in the I.2 part, the optical properties of wurtzite-type nitrides are anisotropic. This results in a uniaxial birefringence of these materials. The knowledge of the refractive indices is important for the elaboration of the structures of optoelectronic devices, in particular for optical confinement. In the particular case where the material is considered as isotropic (we can consider in the case of our setup that the sample is isotropic), the complex refractive index is written as follows:

$$N = n - iK \quad (\text{I.25})$$

where n is the real part of the refractive index and K is the extinction coefficient which reflects the absorption. The complex index is related to the dielectric constant by the relation:

$$\varepsilon_r = N^2 = n^2 - K^2 + 2inK \quad (\text{I.26})$$

As $\varepsilon_r = \varepsilon_1 + i\varepsilon_2$ then: $\varepsilon_1 = n^2 - K^2$ et $\varepsilon_2 = 2nK$

In the transparency range, far from the band gap energy of the semiconductor, the variation of the real refractive index as a function of the wavelength is given by Sellmeier's law:

$$n(\lambda) = \sqrt{a + \frac{b\lambda^2}{\lambda^2 - c^2}} \quad (\text{I.27})$$

a, b and c are the Sellmeier's coefficients. The refractive index can be measured precisely by spectroscopic ellipsometry. Far from an excitonic resonance, the material is considered as a transparent medium and the refractive index becomes real, i.e. $\varepsilon_r = n^2$. For direct-gap materials, the value of the square of the absorption coefficient is linear with the photon energy above the gap energy, i.e.:

$$\alpha^2 = (\alpha_0)^2 (E - E_g) \quad (\text{I.28})$$

This coefficient is related to the extinction coefficient by : $\alpha = \frac{4\pi K}{\lambda_0}$ Figure I.14 displays the α absorption coefficient of bulk GaN epitaxial on sapphire.

I.7.2 Bandgap Renormalization

The bandgap energy introduced in paragraph I.5.2 is not constant in relation to the carrier density and the temperature. The width of the bandgap depends on the total amount of interacting carriers in a semiconductor and on the critical temperature T_c above which the carriers have the characteristics of a liquid-like electron-hole plasma.

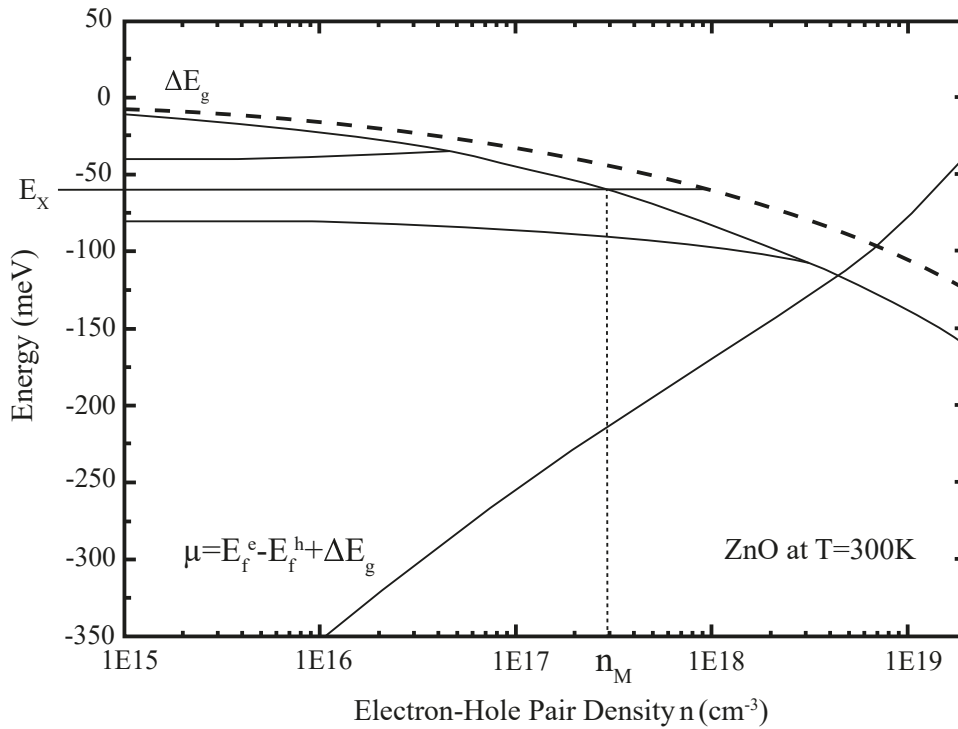


Figure I.15 – Evolution of the band gap energy shift ΔE_g , the exciton energy E_X and the chemical potential μ of electron-hole pairs as a function of the electron-hole density n at 300 K in ZnO. The dotted line ΔE_g corresponds to the calculation of the reference [63] and the vertical dotted line n_M define the Mott transition. Figure from [64]

Experimentally, and as shown on the fig.I.15 the width of the bandgap will decrease with the increase of the density of electron-hole pairs. Concretely, inside the electron-hole plasma, we can see that the Coulomb energies attract the carriers of opposite charge and repel those of the same charge. If

the distribution of carriers in the material was random, the coulomb attractions and repulsions would cancel each other exactly and would not depend on the carrier density. In reality, the carriers are not randomly distributed in the electron-hole plasma. The Pauli principle, which is a consequence of the exchange interaction of identical fermions, forbids two electrons of parallel spin to be in the same unit cell. Since this situation would occur for a random distribution, but does not occur for fermions, one can conclude that the exchange energy increases the average distance between the parallel spin and parallel spin electrons and consequently reduces their total repulsive Coulomb energy. The reduction of a repulsive energy term means a decrease in the total energy of the electron system. The same arguments apply to holes. The volume r_s^3 occupied by a carrier pair in the plasma can be compared with the volume of an exciton. The dimensionless quantity r_s/a_B is used to describe the reduction of the bandgap ΔE_g normalized by the excitonic Rydberg energy as a function of the normalized plasma density n_p including the exchange correlation energy [65, 63].

$$r_s = \left(\frac{4\pi a_B^3}{3} n_p \right)^{-1/3} \text{ and } \Delta E_g/E_B = f(r_s) \quad (\text{I.29})$$

Due to the negative exponent, the volume will decrease as the carrier plasma density will increase. The renormalization is not directly temperature dependent as it relies on the binding energy of carriers. The fig I.15 also display the constant energy of the exciton as a function of n_p . As the gap ΔE_g decrease with increasing n_p , one can expect to see a shift towards lower energy as well as the decreasing of the exciton binding energy due to the screening of the Coulomb energy which shifts the exciton closer to the gap. Those two simultaneous phenomenon compensates almost perfectly and justify the absolute energy of the exciton [64]. The increase of carrier density n_p will cause the decrease of oscillator-strength and the reduction of the binding energy leads to an increase of the excitonic radius and thus to a decrease of the overlap of electron and hole wavefunction. It will also have another consequences such as the screening of the coulombic interactions between electrons and holes dissociating the excitons into an electron-hole plasma. The critical carrier density is called the Mott density n_M .

I.7.3 Introduction to the Mott transition

The exciton is composed of two fermions, has an integer spin, so the exciton is part of the family of bosons and meets the Bose-Einstein statistic.

An increase in carrier density is followed by an increase in the number of excitons and will gradually reduce the average distance between them. This increase has the effect of reinforcing their fermionic character through coulombic interactions and the continuous filling of the phase space. The reason for this resides in the effective screening of the Coulomb interaction between electrons and holes owing to the surrounding free carriers. The screening of Coulomb interactions cause the end of $e - h$ pairs and the interaction potential then becomes:

$$U_s(r) = -\frac{e^2}{4\pi\epsilon_0\epsilon_r} \exp(-k_s r) \quad (\text{I.30})$$

where $k_s = k_s(n) > 0$ is the so-called screening factor and n the carrier density. Alternatively, $\lambda_s = k_s^{-1}$ is called the screening length. As the $e - h$ pair density n increases, the screening length λ_s get shorter until it approaches the free exciton radius a_{B_X} where the attraction between the electron and hole is destroyed. The Mott transition will partially change the carrier behaviors: a mix between an exciton gas made of bosons and described by the Bose-Einstein statistic with an electron-hole plasma (through ionization) driven by the Fermi statistics. The carrier density n thus, will be the most decisive parameter in the calculation of the Mott density. Debye-Hückel and Thomas-Fermi models relies on the screening length to determine the critical carrier density where excitons no longer exists. They will now be described.

I.7.3.1 Debye-Hückel Model

The Debye-Hückel model also state that the Mott density n_M is achieved when the excitonic Bohr radius a_{B_X} becomes comparable to the screening length. The screening length λ_s is given by:

$$\lambda_{DH} = \left(\frac{\epsilon_r \epsilon_0 k_B T}{e^2 n} \right)^{1/2} \quad (I.31)$$

The Mott density is then deduced as:

$$n_M^{DH} = (1.19)^2 \frac{\epsilon_r \epsilon_0 k_B T}{e^2 a_B^2} = (1.19)^2 \frac{k_B T}{2 a_B^3 E_B} \quad (I.32)$$

This model comes with limitation in extremum of temperature as it cannot describe the Mott density in the $T \rightarrow \infty$ temperature limit as $n_M^{DH}(T \rightarrow \infty) = \infty$ and will also fails to calculate the Mott density at low temperatures as the screening of excitons will automatically occur, meaning when $n_M^{DH}(T \rightarrow 0) = 0$. The Debye-Hückel is essentially used in literature [66] for intermediate temperatures. The approach followed by this model is valid as long as the exciton and carrier gases are described through the classical Maxwell-Boltzmann statistics.

The phase diagram shown in fig. I.16 describes the different phase possible for the carriers. Depending of the carrier density and screening length, carriers may transform into electron-hole plasma (EHP), Bose-Einstein condensate (BEC) or electron-hole liquid (EHL) phases. Critical point n_C and the calculated Mott density from Thomas Fermi (n_M^{TF}) as well as the Mott transition calculated from the Debye-Hückel (n_M^{DH}) are also indicated. The areas are calculated from the Debye-Hückel model. At low temperatures, where the carrier gas is degenerate, the Thomas-Fermi screening length is more appropriate and will be described.

I.7.3.2 Thomas-Fermi Model

The Thomas-Fermi Model gives a temperature-independent value of n_M^{TF} as follow:

$$n_M^{TF} a_B^3 \approx 1 \quad (I.33)$$

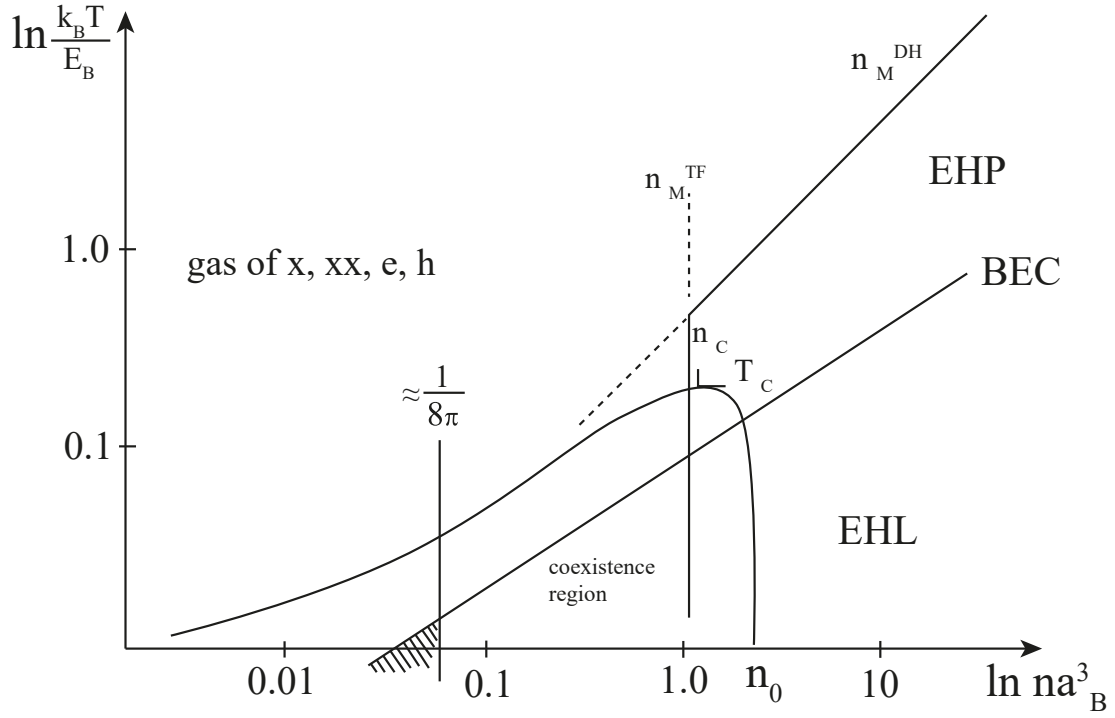


Figure I.16 – Phase diagram for Excitonic phases and EHP based on the Debye-Hückel model. The initial carrier density n_0 undergo several phase transition. From [67]

the position of n_M^{TF} is also reported on fig. I.16. This model is more or less a rule of thumbs of the Mott density estimation as it tends to overestimate by one or two order of magnitude the Mott transition. As shown in the fig. I.16 from the Thomas-Fermi model, the electron-hole plasma as abruptly induced at a certain carrier density. Considering a degenerate electron-hole plasma, the Thomas-Fermi screening length leads to the following expression for the Mott density:

$$n_M^{TF} = (1.19)^6 a_B^{-3} \frac{\pi}{192} \left(\frac{m_e m_h}{(m_e + m_h)^2} \right)^3 \quad (I.34)$$

I.7.3.3 Versteegh Model

In order to compute the Mott density we consider the screening of the Coulomb interaction through the Yukawa potential, as characterized by its screening length, λ_s , within the approximation of static screening which is verified for GaN. The Mott density n_{Mott} corresponds to the density at which λ_s matches the exciton Bohr radius.

To compute the Mott density, we use the same approach developed by Versteegh et al.[68]. The screening of the Coulomb interaction is described through the Yukawa potential:

$$V(\vec{r}_e - \vec{r}_h) = \frac{e^2}{4\pi\epsilon_0\epsilon_r \|\vec{r}_e - \vec{r}_h\|} e^{-\frac{\|\vec{r}_e - \vec{r}_h\|}{\lambda_s}}$$

The latter is characterized by the screening length, λ_s , within the approximation of static screening, which can be justified by the fact that the Fermi energies ($E_{F,i} = \frac{\hbar^2}{2m_i}(3\pi^2 n)^{2/3}$) are smaller than \hbar

times the plasma frequency $\omega_p = \sqrt{\frac{e^2 n}{\epsilon_0 \epsilon_r m_r}}$ where m_r is the reduced mass of the electron-hole pair. The ideal gas model in which the electron density is equal to the hole density, $n_e = n_h = n$ is considered for optical excitation. The Mott density n_M corresponds to the density at which λ_s equals the exciton Bohr radius a_0 . λ_s is derived using numerical calculation of the chemical potentials as function of the carrier density n in the ideal gas approximation:

$$\lambda_{s,e} = \sqrt{\frac{\epsilon_0 \epsilon_r}{e^2} \frac{\partial \mu_e}{\partial n}}$$

and $\lambda_s^{-1} = \lambda_{s,e}^{-1} + \lambda_{s,h}^{-1}$.

The ideal-gas chemical potential (μ_e, μ_h) is numerically calculated from:

$$p = n = \frac{1}{2\pi^2} \left(\frac{2m_i}{\hbar^2} \right)^{2/3} \int_0^\infty \frac{\sqrt{\epsilon}}{1 + \exp\left(\frac{\epsilon - \mu_i}{kT}\right)} d\epsilon, \text{ with } i = e \text{ or } h \quad (\text{I.35})$$

The electron chemical potential μ_e is measured from the conduction-band edge and the hole chemical potential μ_h is measured from the valence-band edge. Note that the ideal gas approximation slightly overestimates the screening due to the weaker screening by excitons than by unbound carriers. This first approach can be refined by computing the excitonic fraction n_{exc}/n , which represents the fraction of carriers that are bound into excitons with respect to the total carrier density n :

$$n = n_{exc} + \frac{1}{2\pi^2} \left(\frac{2m_i}{\hbar^2} \right)^{2/3} \int_0^\infty \frac{\sqrt{\epsilon}}{1 + \exp\left(\frac{\epsilon - \mu_i}{kT}\right)} d\epsilon,$$

$$n_{exc} = \frac{1}{\pi^2} \left(\frac{2(m_e + m_h)}{\hbar^2} \right)^{2/3} \int_{-E_s}^0 \sqrt{\epsilon + E_s} \times f_{exc}(\epsilon) d\epsilon$$

with f_{exc} given by Bose-Einstein statistic:

$$f_{exc}(\epsilon) = \frac{1}{\exp\left(\frac{\epsilon - \mu}{kT}\right) - 1}$$

and $E_s = \begin{cases} (1 - a_0/\lambda_s)^2 E_B & \text{if } \lambda_s \geq a_0 \\ 0 & \text{if } \lambda_s < a_0 \end{cases}$, a_B and E_B being the unscreened hydrogenoid

excitonic Bohr radius and binding energy respectively. By making the rough assumption that excitons do not contribute to screening at all, the excitonic fraction firstly derived from the ideal gas model is used to reevaluate the screening length and then a self-consistent calculation tends towards the new excitonic fraction and screening length. This leads that the errors in the screening length because of using the ideal gas theory are at less than 7% for GaN.

I.7.4 Strong coupling

So far, we have considered independently bulk-confined photons and excitons. The following section will detail how these two particles are linked by the light-matter coupling.

Two types of coupling are possible: the weak coupling and the strong coupling. The weak coupling corresponds to the case where the interactions between the confined photons and the excitons of the semiconductor are irreversible. The light-matter coupling is treated as a perturbation and the system is described by the Fermi golden rule and the Purcell effect. When the lifetime of the photon is greater than the time necessary for its re-absorption by the excitons, the interactions are reversible and the previous treatment is no longer valid.

When exciton and photon are linked to each other in the microcavity and if the coupling force is greater than the damping losses, the strong coupling regime is reached. Polaritons are quasi-particles whose properties vary according to the excitonic (respectively photonic) fraction of its wave function and are considered as bosons. The excitonic and photonic modes give two new eigenstates: the lower polaritonic branch and the upper polaritonic branch (commonly called LPB and UPB). The corresponding quasi-particle is the exciton-polariton, simply called polariton hereafter. The strong coupling can be described with a classical model using the formalism of Maxwell's equations or using a quantum model. Both of those models will not be described in this thesis. After having described the strong coupling regime we will determine the density conditions favorable to the polariton lasing effect. Finally, a state of the art of polariton lasers will be presented.

I.7.4.1 Bose-Einstein Condensate

In this part, the properties of bosons and the phenomenon of Bose-Einstein condensation will be explained. We will see how the condensation takes place in the case of microcavity polaritons and what specific mechanisms are involved in the polariton laser effect. From a quantum point of view, it is possible to describe the polariton as a proper state resulting from the superposition of the wave functions of the photon and the exciton.

Quantum effects occur when the De Broglie wavelength λ_T representing the spatial extension of the particle becomes comparable to the inter-particle distance.

$$\lambda_T = \sqrt{\frac{2\pi\hbar^2}{mk_bT}} \quad (\text{I.36})$$

The above equation shows that the temperature and mass are the two parameters influencing the appearance of quantum effects. The classification of quantum particles is done according to the symmetry of their wave functions, we find two categories: fermions whose wave function is anti-symmetric and bosons whose wave function is symmetric. The distribution of bosons follows the Bose-Einstein statistics through the occupation function f_{BE} such as:

$$f_{BE}(\vec{k}, T, \mu) = \frac{1}{\exp\left(\frac{E(\vec{k}) - \mu}{k_B T}\right) - 1} \quad (\text{I.37})$$

Where $E(\vec{k})$ is the dispersion relation of the considered bosons and μ the chemical potential, determined from the conservation of the total number of particles N . As the occupation function f_{BE}

cannot be negative, the chemical potential must respect the condition $\mu < E(0)$ where $E(0)$ is the energy of the fundamental level. The expression for the total number of particles is as follows:

$$N(T, \mu) = \sum_{\vec{k}} f_{BE}(\vec{k}, T, \mu) = \frac{1}{\exp\left(\frac{E(0)-\mu}{k_B T}\right) - 1} + \sum_{\vec{k} \neq 0} f_{BE}(\vec{k}, T, \mu) \quad (I.38)$$

In the thermodynamic limit ($N \rightarrow \infty$, $L^d \rightarrow \infty$, and $n = N/L^d$ is constant and where d represents the physical dimension of the system), the total density n is obtained by integrating the distribution in \vec{k} space :

$$n(T, \mu) = \lim_{L \rightarrow \infty} \frac{N(T, \mu)}{L^d} = n_0(T, \mu) + \frac{1}{(2\pi)^d} \int_{E > E(0)}^{+\infty} f_{BE}(\vec{k}, T, \mu) d^d \vec{k} \quad (I.39)$$

where $n_0(T, \mu)$ is the density in the ground state :

$$n_0(T, \mu) = \lim_{L \rightarrow \infty} \frac{1}{L^d} \frac{1}{\exp\left(\frac{E(0)-\mu}{k_B T}\right) - 1} \quad (I.40)$$

$n_0(T, \mu)$ is null when μ is different from $E(0)$. Also, the term on the right of equation I.39 is an increasing function of μ corresponding to the density of excited states. Increasing the density of particles in the system is therefore equivalent to increasing the chemical potential. The maximum density that this term can reach is called critical density $n_c(T)$:

$$n_c(T) = \lim_{\mu \rightarrow 0} \frac{1}{(2\pi)^d} \int_{E > E(0)}^{+\infty} f_{BE}(\vec{k}, T, \mu = E(0)) d^d \vec{k} \quad (I.41)$$

n_c converges only for values of dimension d higher than 2.

Beyond the critical density, the excited states are saturated and additional particles will occupy the ground state. This phase transition to a macroscopic occupation of the lowest energy level was first proposed in 1925 by Einstein. Its density is expressed by:

$$n_0(T) = n(T) - n_c(T) = n(T) \left[1 - \left(\frac{T}{T_c} \right)^{3/2} \right] \quad (I.42)$$

where T_c is the critical temperature below which the Bose-Einstein transition occurs. Because of their photonic component, their effective mass is of the order of 10^{-8} times that of atoms and 10^{-3} that of excitons. However, the critical temperature T_c of condensation is inversely proportional to the mass of the particle studied. In a 3D space, for an ideal Bose gas the critical temperature is equal to :

$$T_c = \frac{2\pi\hbar^2}{mk_B} \left(\frac{n}{2.612} \right)^{2/3} \quad (I.43)$$

The first experimental observation of a Bose-Einstein condensate was made by Wieman and Cornell in 1995, in a system of rubidium atoms cooled down to 170 nK [69]. This extremely low

temperature is required because of the high mass of these atoms. With the idea of increasing T_c to more experimentally accessible temperature ranges, lighter particles are needed. Cavity polaritons, whose mass may be up to five orders of magnitude smaller than that of electrons, appear to be ideal candidates. However, the previous 3D space assumption for the critical temperature does not apply because the confinement of photons gives the system 2D characteristics. In this case, the last term of equation I.39 never converges and Bose-Einstein condensation in the strict sense is not allowed. Nevertheless, a local condensation via a transition to a superfluid state is possible (Kosterlitz-Thouless transition) [70].

I.7.4.2 Polariton Lasing

The original theory of Bose-Einstein condensation was established by considering a closed, thermodynamically equilibrium, interaction-free system of bosons. Microcavity polaritons do not respect any of these three properties as they have an extremely short lifetime, of the order of a picosecond, and their equilibrium distribution is a compromise between the polaritons created by the pumping, which interact through their excitonic component to relax to the ground state, and the polaritons that escape from the cavity. The microcavity polaritons thus constitute an open system out of equilibrium. However, it is possible to bring the system relatively close to equilibrium by playing with some parameters the system relatively close to equilibrium.

In this case, the properties of the polariton quasi-condensate will be very similar to those of a Bose-Einstein condensate (macroscopic occupation of the ground state, high coherence length, etc). The first experiment demonstrating polariton Bose-Einstein condensation was performed in 2006 by Kasprzak et al. in a CdTe microcavity [71]. Since then, the name polariton condensate is commonly accepted and will be used hereafter. The different steps leading to the condensation of polaritons in the lowest energy state in the typical case of a non-resonant optical excitation are summarized in the figure below:

1. The first step corresponds to the high energy optical pumping of the microcavity using a continuous or pulsed laser or pulsed laser, with energy higher than the band gap energy of the material composing the active layer.
2. In a second step, the high energy electron-hole pairs will relax in a few tens of femtoseconds towards the lowest energy states by emitting optical phonons [72]. This process is accelerated in GaN and ZnO due to the high energy of the LO phonons (92 and 72 meV) and the Fröhlich coupling between the free carriers and the optical phonons. The emission of acoustic phonons takes over once the excess energy of the carriers becomes lower than the energy of these processes lead to the formation of polaritons (with a very strong excitonic character) in the excitonic reservoir located at large wave vector (or large angle).
3. These polaritons will then enter the light cone and relax along the lower branch by emitting optical and acoustic phonons. These relaxation processes become inefficient at the level where the curvature of the LPB changes its sign: the polaritons must give up an energy and little wave

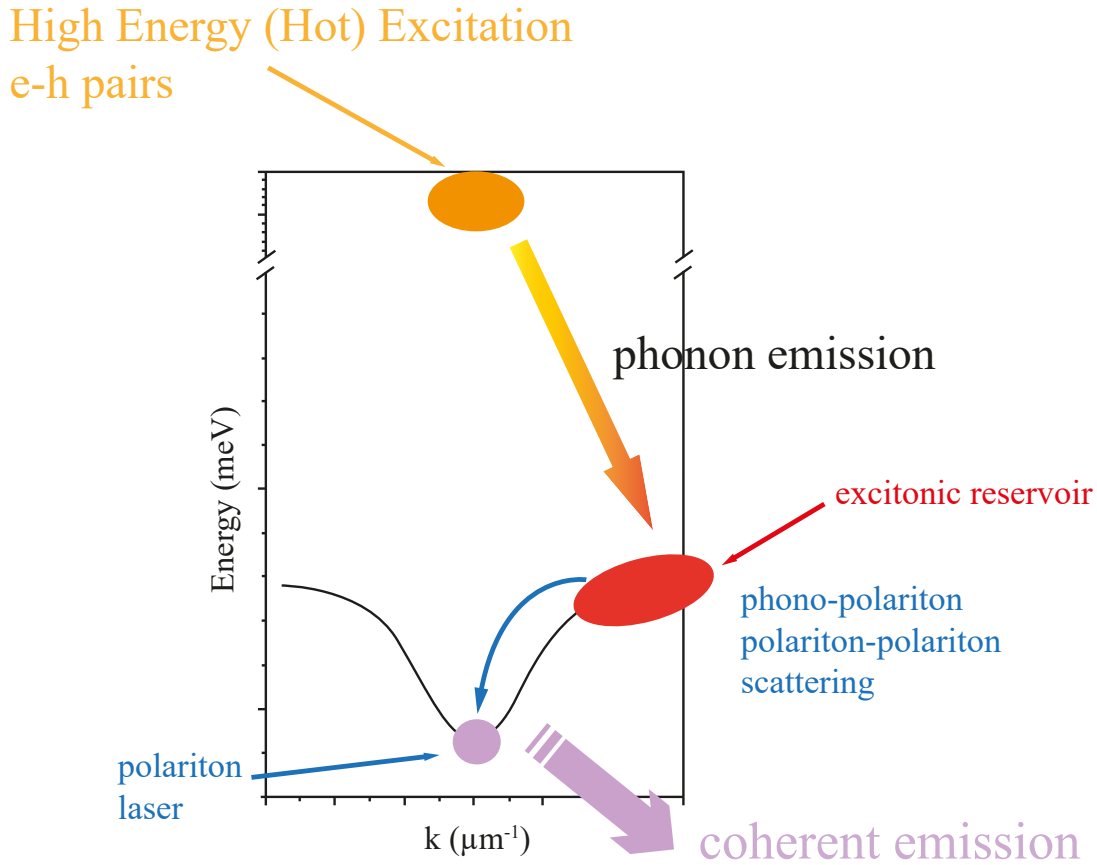


Figure I.17 – Schematic representation of the processes leading to the polariton laser in a planar microcavity under non-resonant excitation. The black curve corresponds to the dispersion of the LPB from [6]

vector.

The polaritons will therefore accumulate in this region, called "bottleneck [73]. Moreover, as the polaritons relax, their photon fraction increases as for low k values, the LPB dispersion is strongly influenced by the photonic dispersion. Consequently, the decreases of both their lifetime and their probability to interact with other particles. This effect can be overcome by increasing the carrier density, in order to increase the population of polaritons and to favor polariton-polariton scattering processes. These processes relaxation processes allow the polaritons to reach the ground state. We will also see that relaxation can take place directly from the excitonic reservoir to the ground state of the LPB when the difference between these two levels is equal to the energy of one or two LO phonons.

4. The relaxation process comes to an end when the minimum of the lower branch at $\vec{k} = 0$ is reached: this state is privileged for the accumulation of polaritons and consequently for polariton lasing [6].

The luminescence of the polariton condensate, also called polariton laser [7], shares similar properties to those of a classical laser such as the emission of coherent and monochromatic photons. The relaxation of polaritons is "stimulated" by the occupation of the final state and not by the emission

of light known in classical lasers. Therefore, and contrary to the classical laser, the polariton laser does not require any population inversion. The excitation power required to obtain polariton condensation and polariton lasing is called the laser threshold and is intrinsically linked to the efficiency of polariton relaxation from the excitonic reservoir to the bottom of the LPB.

I.7.4.3 State of the art of polariton laser

After the theoretical description of the polariton laser given by Imamoglu et al. [7], the first experimental signs of stimulated ground state emission were observed by Le Si Dang et al. in 1998 in a CdTe quantum well microcavity at 5K [74]. These results were followed followed in 2003 by the demonstration of the polariton lasing effect by Deng et al. in a GaAs quantum well microcavity at 4K [75]. Since then, the polariton laser has been observed repeatedly in both materials, either in microcavities [71, 76, 77], or in geometries allowing an increased confinement of polaritons, such as micropillars [6, 78]. In all these publications, the macroscopic occupation of the ground state has been realized only for temperatures below 100K because of the low binding energies of the GaAs and CdTe excitons ($E_B \leq 10\text{meV}$).

The objective being to benefit from the advantages of the polariton laser operating at room temperature, the use of materials possessing excitons with high binding energies is essential. In inorganic materials, attention has quickly turned to semiconductors with larger band gap energies such as GaN [79, 80], ZnO [81, 82], CuCl [83] or ZnSe [84, 85]. Currently, even if all these materials have allowed the observation of the strong coupling regime in microcavities, the demonstration of the polariton laser at room temperature remains experimentally challenging because of the strong thermal agitation ($k_B T > 25\text{meV}$), the bandgap energy evolution in regard of the temperature and the low carrier lifetime at high excitation densities.

I.8 GaN based lasers and interest of nanowires

Interest in nitride-based semiconductors for optoelectronics has constantly grown over the years. This success is due to the remarkable properties of the material: (i) direct bandgap structure used for optical devices based on (Al,In,Ga)N alloys which allows for a spectrum of applications from visible to ultraviolet in emission and detection [1]; (ii) significant excitonic binding energies and oscillator strengths, leading to a relative robustness of excitons at high temperature [2]; (iii) well controlled doping and growth [3]. The fabrication of devices such as light emitting diodes (LEDs) and lasers have made it the first III-V material in terms of industrial share in a wide range of wavelengths (white, green, blue, and ultra-violet).

In the context of coherent light emission from GaN-based devices, a potential way to reduce the laser threshold is to use exciton-polaritons within the strong light-matter coupling regime [7]. Due to the exciton-polaritons bosonic character, a gain mechanism based on stimulated relaxation

by final-state occupation can trigger polariton condensation and, thus, coherent light emission, at particle densities below those conventionally encountered in edge-emitting and vertical-cavity surface emitting lasers [6].

As it has been seen in Part I.3, difficulties due to heteroepitaxial growth related to structural properties are a strong limitation on the quality of GaN-based devices. Nanowires are part of a growing research effort since 30 years and represent an interesting geometry to not only overcome the defects of planar based layers but also to show promising results in a wide range of applications that will further be detailed.

The main advantages of the nanowire geometry are:

- The limitation of dislocation density through strain relaxation even on highly mismatched substrate [86, 87].
- the higher active surface compared to a planar structure thanks to the use of a core-shell structure [88].
- possibility to control the critical wire diameter variation, crucial for optical confinement via selective growth and the use of binary materials (In and Al) [89].
- the increase of the optical extraction and natural predisposition to the guidance [90].

Nanowires are more and more often related to the creation of photonic devices such as polarization sensitive photodetectors [91], light-emitting diodes, [92, 93, 94, 95], and lasers [96, 97, 98, 99]. It has been shown in the literature that researches tend to involve single nanowires as optical wave-guides and Fabry–Pérot cavities [97, 98], and the optical excitation of single nanowire cavities has produced stimulated emission and lasing [96, 97, 99]. As the understanding of gain mechanism in nanowire lasers are yet to perfectly master, integrated applications exploiting nanowire lasers will likely involve electrical injection devices. More specifically, the research on GaN lasers, and in particular on polariton lasers, requires an in-depth and reliable knowledge of the GaN opto-electronic properties: as excitons may have a substantial role in lowering the laser threshold, it is thus essential to investigate the conditions, in terms of particle density and temperature, under which GaN excitons can exist. This will in turn determine the possible laser gain mechanisms in play that, from a general point of view, may involve polaritonic relaxation stimulated by the final state occupation [6], P-band exciton interactions scattering processes [8], or standard degenerate electron-hole plasma [9].

I.9 Conclusion

To conclude, this first part was essential to better grasp all the concepts involved with GaN based studies. It highlights the complexity and the overall connection between crystalline quality (impacted by the chosen growth technique) and the electronic or optical properties. We will introduce in the next chapter all the experimental measurements involved in the optical characterization of GaN based samples as well as their exploitation.

Experimental techniques

This chapter is focused on the description of the experimental techniques used throughout the thesis. As the experimental results depend directly on the equipment, a precise understanding of the phenomena is required in order to fully exploit and interpret the results that are gathered through the different experimental campaigns. The first section presents the general principles of optical spectroscopy in real and Fourier space as well as in the equipment used for its realization. We will then see in more detail the principles of time-resolved optical spectroscopy and the types of results provided by these experimental techniques

II.1 Optical spectroscopy

The aim of spectroscopy is to disperse luminescence radiation into a spectrum, which is subsequently detected and recorded. In our case, optical spectroscopy is the study of the spectra of re-emitted, absorbed or transmitted radiation by a semiconductor material when it is subjected to light excitation. In the range of electromagnetic spectrum, it allows to probe for different energies the intrinsic properties (optical index, dielectric constant, energy, oscillator strength of optical transitions, lattices' interaction...) structural (thickness, alloy composition, stress...) and to a certain extent the extrinsic properties of the studied material (residual doping, defects...).

Figure II.1 summarizes the possible responses of an optically excited structure: reflection (reflectivity and ellipsometry) or transmission of photons (transmission) but also emission of photons by radiative de-excitation of the semiconductor (photoluminescence) or phonons from non-radiative de-excitation (thermally detected optical absorption).

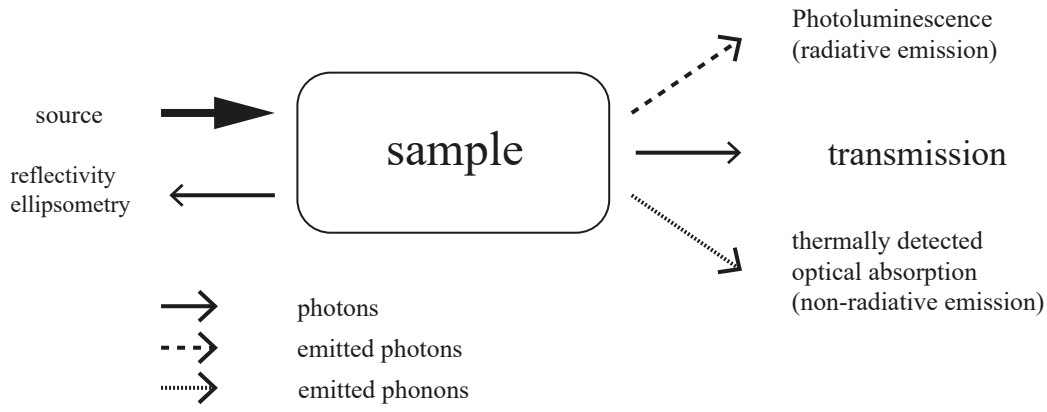


Figure II.1 – Response of a sample to an optical excitation: the different optical spectroscopy techniques available as well as the studied particles are represented

II.2 Photoluminescence and reflectivity

II.2.1 Photoluminescence principle

Photoluminescence (PL) is the analysis of photons emitted by a sample under light excitation. The semiconductor is excited by a source (laser in the case of optical pumping) whose energy is higher than the band gap energy.

As illustrated in figure II.2, in the case of optical pumping, the absorption of photons creates electron-hole pairs with a large wave vector. The electrons can pass from an initial state of energy E_i to a higher energy state of energy E_f . These pairs will progressively de-excite via non-radiative processes such as phonon emission, allowing them to reach the extrema of the conduction and valence bands by a thermalization process. The de-excitation of the electrons towards their initial level is done by emission of a photon of energy E defined by the relation:

$$E = E_f - E_i = h\nu = \frac{hc}{n\lambda} \text{ and } E(\text{eV}) = \frac{12395.13}{\lambda} \quad (\text{II.1})$$

With h being the Planck's constant, c the speed of light, λ_0 and ν respectively the wavelength in vacuum and the frequency of the radiation associated to the photon and n the index of the air in the conditions of the experiment ($n = 1.000629$). Finally, the photons emitted by the radiative recombination of the thermalized electron-hole pairs are detected.

More precisely, the photoluminescence provides information on the intrinsic and especially extrinsic properties of the material (band gap energy, impurity levels, recombination mechanisms...). This measurement is done by exciting the studied semiconductor with an intense monochromatic light (laser) that have an energy higher than that of the semiconductor band gap and to analyze the re-emitted light. The light sent from the excitation laser is absorbed by the semiconductor according to a process called "photo-excitation". The latter induces the transfer of electrons from a semiconductor to allowed excited states. When these electrons return to their equilibrium state, the released energy can

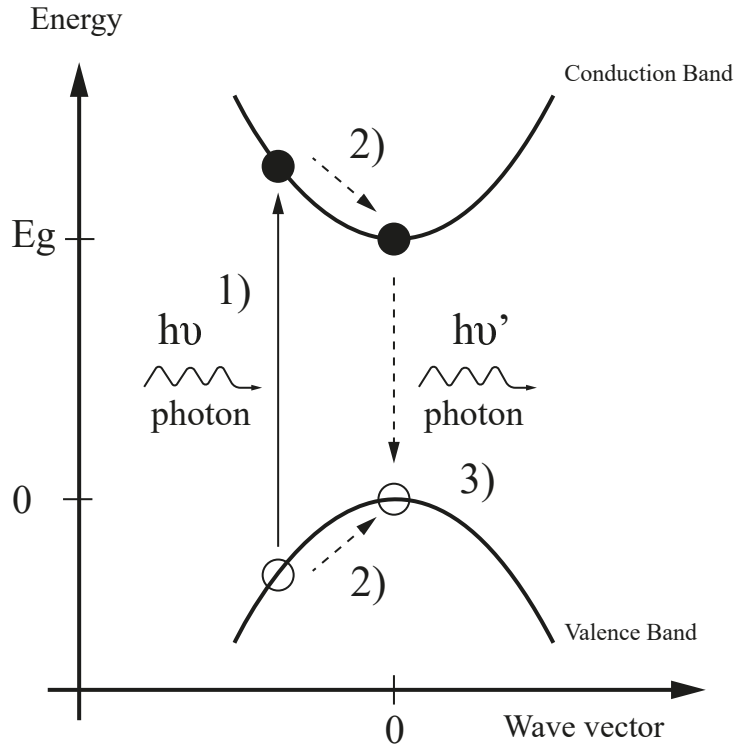


Figure II.2 – Processes involved in photoluminescence: (1) photoexcitation, (2) thermalization and (3) radiative recombination.

lead to the emission of light (radiative process) or to the creation of phonons (non-radiative process). In the case where the energy absorbed by the sample is restored in the form of luminescence, it is called photoluminescence. The intensity of the emitted light is much weaker than that of the radiation used for the excitation. The energy of the emitted light is directly related to the energy difference between the two states of the electron: the equilibrium state and the excited state. Among the applications of photoluminescence, we can mention: - the determination of the band gap energy, - the detection of impurity levels and defects, - the understanding of radiative and non-radiative recombination mechanisms, - the determination of the quality of a material from the measurement of the yield of radiative radiative recombinations.

The analysis of μ PL spectra of semiconductors is rich in property information. If reflectivity gives access to intrinsic properties of materials, photoluminescence gives information on intrinsic (excitons) and extrinsic (impurities) properties. Generally, photoluminescence experiments are performed at low temperatures because of a better radiative efficiency on one hand, and to avoid line broadening due to phonon interactions on the other hand. Nevertheless, temperature-dependent experiments are sometimes necessary to identify certain lines related to impurities on which carriers or excitons (excitonic complexes) can be located.

Concretely, photoluminescence reflects low energy states and does not reflect the density of state. The sample is subjected to a light excitation and the re-emitted photons are analyzed. The light excitation leads to the creation of electron-hole pairs with large wave vector. These pairs relax by non-radiative processes, such as phonon emission to the conduction and valence band extremes where they

emit photons by radiative recombination. Two types of photoluminescence can be measured, either as a function of the excitation energy with a fixed detection energy (excitation of photoluminescence), or as a function of the emission energy with a fixed excitation energy. It is this last method that we will use.

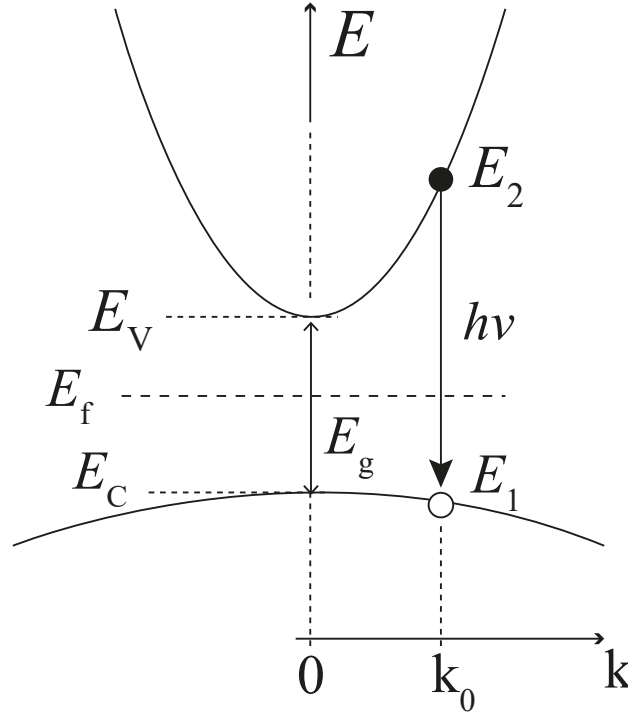


Figure II.3 – Free electron–hole recombination in a direct bandgap semiconductor from [100]

The intensity of the spontaneous emission I_{sp} depends on $f(v)$, the probability given by the product of the probabilities that an electron occupies a state of energy E_2 and that a hole occupies the corresponding state of energy E_1 of the same wave vector, on $|P_{cv}|^2$, the squared modulus of the optical matrix element expressing the probability of this transition and on $\rho(v)$ the joint density of state.

$$I_{sp}(hv) = f(v) |P_{cv}|^2 \rho(v) \quad (\text{II.2})$$

Where the probability $f(v) = f(E_2)[1 - f(E_1)]$ with $f(E) = \frac{1}{1 + \exp\left(\frac{E - E_{\text{Fermi}}}{k_b T}\right)}$. Assuming that $E_2 - E_{\text{Fermi}} \approx E_{\text{Fermi}} - E_1 \approx \frac{E_g}{2} \gg k_b T$, the Fermi function of the previous equation is replaced by a Boltzmann function $f(v) = \exp\left(\frac{-hv}{k_b T}\right)$ where T is the carrier temperature and E_{Fermi} the energy of the Fermi level. The optical matrix element P_{cv} is a term that does not depend on energy. The joint density of states $\rho(v)$ is proportional to $(hv - E_g)$. The approximate luminescence shape corresponding to the band-to-band transition of a direct-gap semiconductor (in the case of parabolic dispersion of valence and conduction bands as shown in figure II.3) is proportional to :

$$I_{sp}(hv) \approx D_0 (hv - E_g)^{1/2} \exp(-(hv - E_g)/k_b T) \quad (\text{II.3})$$

where $D_0 = \frac{(2m_r)^{3/2}}{\pi \hbar^2 \tau_r} \exp(-E_g/k_b T)$, this term does not depend on the energy. The approximate form of luminescence corresponding to the band-to-band transition of a direct-gap semiconductor is finally described by :

$$I_{sp}(h\nu) \equiv (h\nu - E_g)^{\frac{1}{2}} \exp\left(\frac{-(h\nu - E_g)}{k_b T}\right) \quad (\text{II.4})$$

II.2.2 Optical recombinations

The study of photoluminescence spectra is done by analyzing the peaks, recorded during photoluminescence experiments. These peaks represent optical transitions whose origin corresponds to different processes of radiative recombination and will be detailed in this part.

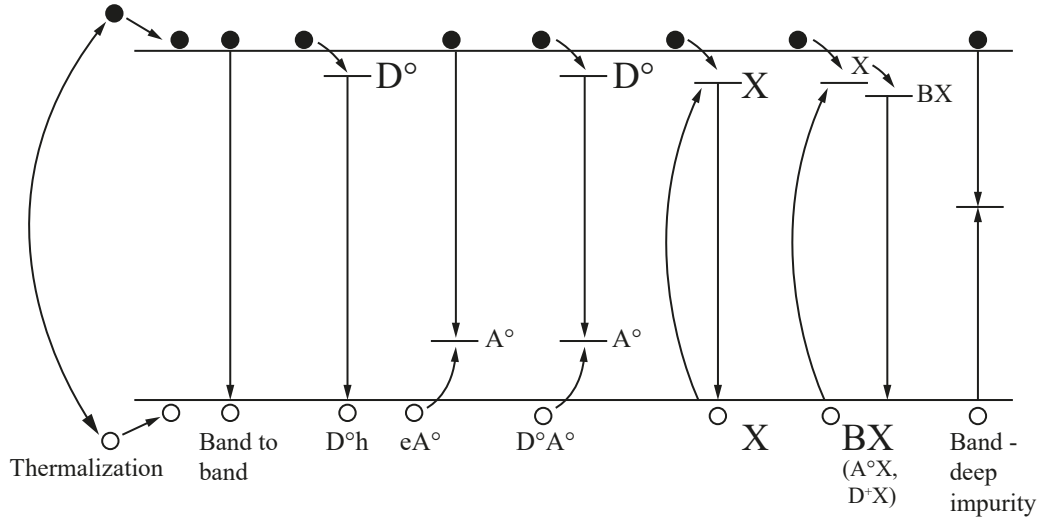


Figure II.4 – Scheme of the main optical recombinations encountered in optical spectroscopy.

The main optical transitions encountered during the different experimental campaigns are presented on the figure II.4:

- The band-to-band recombination is that of an electron from the bottom of the conduction band with a hole from the top of the valence band, as previously detailed.
- The free electron-neutral acceptor (eA^0) and free hole-neutral donor (D^0h) transitions correspond to the recombination of a free carrier with a carrier of opposite charge trapped on an impurity.
- Neutral donor-neutral acceptor recombinations (D^0A^0) involve an electron bound to a donor $D^0 = (D^+, e^-)$ and a hole bound to an acceptor $A^0 = (A^-, h^+)$.
- X represents a free exciton (electron-hole pair in coulombic interaction which can recombine).
- The free excitons can be localized on neutral impurities and form complexes with three or even two particles (notation D^0X , A^0X , D^+X). They can also bind to isovalent centers.
- Radiative recombination processes involving deep centers are often in the minority compared to non-radiative processes involving them.

II.2.2.1 Localized level-band recombinations

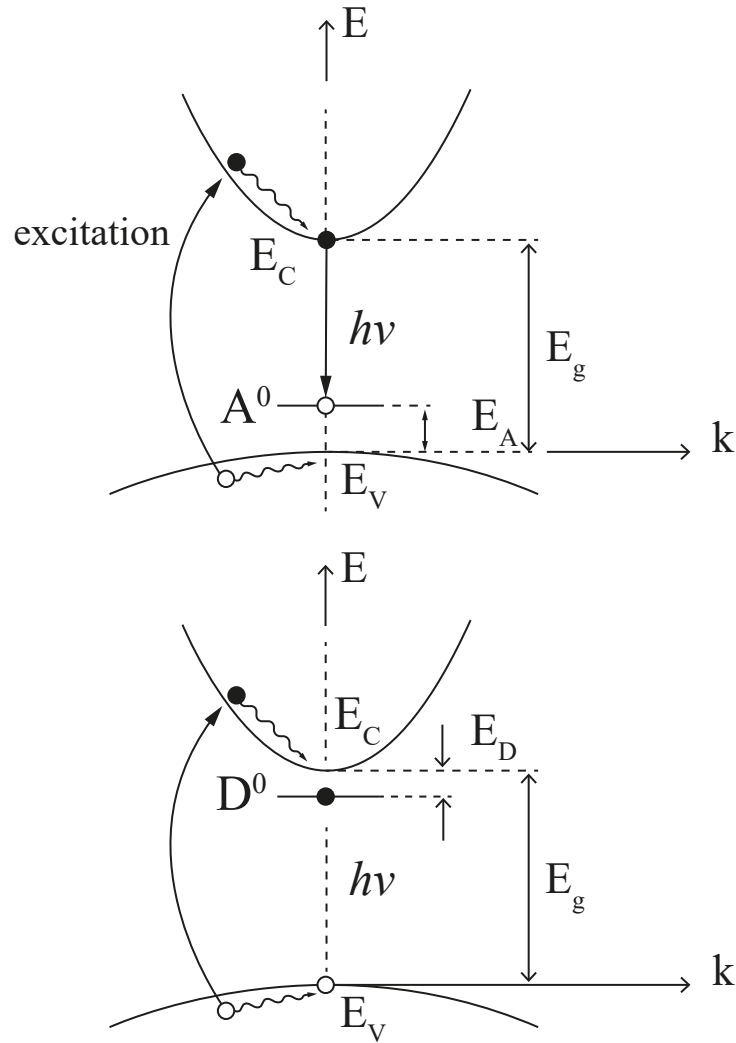


Figure II.5 – (eA^0) recombination (top panel) and D^0h recombination (bottom panel) in a direct-bandgap semiconductor. [100]

This transition is due to the presence of an impurity in the semiconductor crystal and is mostly found as a recombination with the radiative free electron-neutral acceptor (eA^0) and free hole-neutral donor (D^0h) recombinations. An impurity atom in a semiconductor, whose valence is smaller (larger) by one electron than that of the main constituent of the crystal lattice, is referred to as a shallow acceptor (donor). The additional holes or electrons induced by the impurities in the crystal are usually weakly bound and can be thermally excited in the valence band (acceptor) or in the conduction band (donor), for example in GaN shallow acceptor (donor) are magnesium [101] (Oxygen or Silicon) atoms [102].

The corresponding amount of energy needed for the release of the hole or electron is referred to as the ionization (binding) energy of the acceptor E_A or donor E_D . The acceptor and donor states are usually represented in the band structure diagram by short segments drawn inside the bandgap, just above the maximum of the valence band or below the minimum of the conduction band.

Their lower energy thresholds are respectively :

$$h\nu = E_g - E_A \text{ and } h\nu = E_g - E_D$$

The shape of the luminescence spectrum at the recombination level (eA^0 and D^0h) is approximately given by :

$$I_{sp}^{(eA^0)} \approx [h\nu - (E_g - E_A)]^{1/2} \exp\left(-\frac{h\nu - (E_g - E_A)}{k_B T}\right) \quad (\text{II.5})$$

$$I_{sp}^{(hD^0)} \approx [h\nu - (E_g - E_D)]^{1/2} \exp\left(-\frac{h\nu - (E_g - E_D)}{k_B T}\right) \quad (\text{II.6})$$

II.2.2.2 Recombination of donor-acceptor pairs

It is the recombination of an electron trapped on a donor (D^+ center) with a hole trapped on an acceptor (A^- center). In the initial state, the two impurities are neutral, and in the final state, after recombination, they are ionized and thus in coulombic interaction as shown in the figure II.6. This phenomenon is related to the passage of an electron belonging to a binding orbital of the donor to a vacant orbital of the acceptor. When the mobile charge carriers are recombined, the two types of ionized impurities are then in coulombic interaction. The photon produced during this transition has an energy:

$$h\nu = E_g - E_D - E_A + \frac{e^2}{4\pi\epsilon_0\epsilon_r R} \quad (\text{II.7})$$

The last term of the above formula is the term of coulombic interaction of the ionized donor-acceptor pair, R being the distance between a donor and an acceptor.

II.2.2.3 Bound excitons recombination

Excitons can bind to impurities and give rise to the following complexes: - exciton bound to a neutral donor or acceptor: (D^0X) or (A^0X) - exciton bound to an ionized donor or acceptor: (D^+X) or (A^-X) - exciton bound to an isovalent center (uncharged center). When the exciton recombines radiatively from one of these centers, the energy of the emitted photon is $h\nu = E_g - E_X - E_{loc}$ where E_{loc} denotes the localization energy of the exciton on the impurity.

When the exciton recombines radiatively from one of these centers, the energy of the emitted photon is:

$$h\nu = E_g - R_{ex} - E_{loc} \quad (\text{II.8})$$

R_{ex} being the ionization energy of the free exciton in its ground state given by the following relation:

$$R_{ex} = -\frac{1}{n^2} \frac{\mu}{m_0 \epsilon_r^2} R_y \quad (\text{II.9})$$

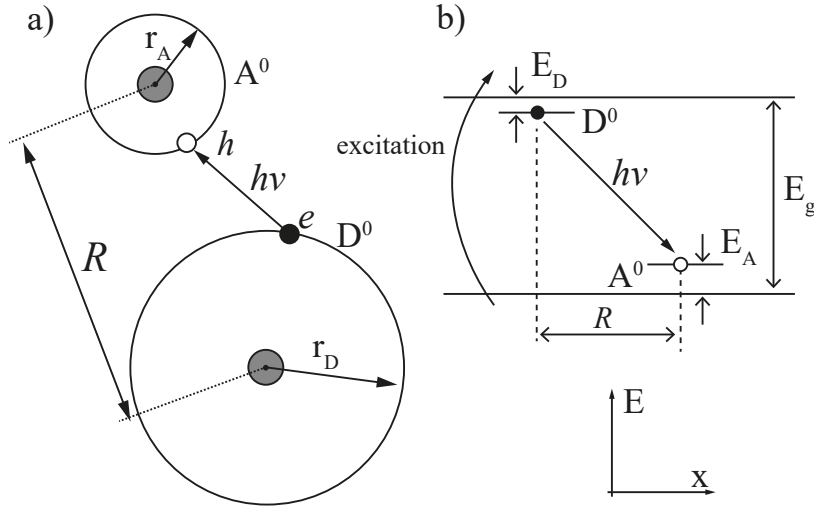


Figure II.6 – The concept of luminescence arising from the recombination of donor–acceptor pairs (D^0A^0): (a) in real space, (b) in the electron energy band structure as a function of the real-space coordinate x . Donor and acceptor atoms are located at different positions of the crystal lattice, separated by the distance R . [100]

In the case of excitons bound to a neutral donor or a neutral acceptor (D^0X) or (A^0X) the localization energy of the exciton on the impurity is related to the ionization energy of this impurity by the rule of Haynes [103] according to which the localization energy of the exciton on a neutral impurity is an affine function of the ionization energy of the impurity. In the case of an exciton bound on a neutral donor (D^0) this rule is written as following:

$$E_{\text{loc}} = a + bE_D$$

The parameters a and b depend on the semiconductor. In the case of GaN, the localization energy of the exciton on the complex increases according to the inequality and thus :

$$E_{\text{loc}}(D^+X) < E_{\text{loc}}(D^0X) < E_{\text{loc}}(A^0X)$$

II.2.2.4 Free excitons recombination

The excitons have an energy slightly lower than that of the band gap. Once created, the electron recombines with the hole it had generated in the valence band. In general the excitons recombine at the vicinity of $\vec{k} = \vec{0}$. The energy of a photon emitted during such a transition is given by:

$$E = E_g - E_X + \frac{\hbar^2 K^2}{2(m_e + m_h)} \quad (\text{II.10})$$

$$E_X = \frac{\mu/m_0}{\epsilon_r^2} \times \frac{13,6}{n^2} (\text{eV}) \quad (\text{II.11})$$

ϵ_r is the static dielectric constant (at zero frequencies) and μ is the reduced mass of the electron-hole pair and n the carrier density and m_0 is the electron mass. $\frac{\hbar^2 K^2}{2(m_e + m_h)}$ is the kinetic energy of the

center of mass and finally the Bohr radius of the exciton is given by, for ($n = 1$) :

$$a_{exc} = \frac{\varepsilon_r}{(\mu/m_0)} a_H; a_H = \frac{\varepsilon_0 \hbar^2}{e^2 \pi m_0} = 0,529 \text{Å} \quad (\text{II.12})$$

II.2.3 Reflectivity

Reflectivity spectroscopy constitutes the analysis of the intensity of the light reflected from the sample as a function of its wavelength. It is a classical technique complementary to photoluminescence to determine excitonic parameters, such as resonance energies, homogeneous or inhomogeneous broadening. Generally, the parameters are obtained after comparison between experimental measurements and calculated reflection spectra based on a theoretical response model.

The reflectivity of a material depends strongly on the intrinsic transitions through the dielectric function, thus being an ideal technique to characterize the excitonic properties of GaN. In addition to a very slow monotonic variation of the latter when the wavelength varies over a large range (variation of the material index due to dispersion), reflectivity spectra often show small more localized variations, as shown in the figure below, when the incident photon energy is slightly lower than the band gap energy. This phenomenon is explained by the absorption of a photon and the creation of an electron and a hole linked by their Coulombic interaction, resulting in the creation of an exciton. In the vicinity of an excitonic resonance, the interaction between the exciton and the incident photon is strong, causing significant variations in the dielectric constant, refractive index and consequently reflectivity spectra.

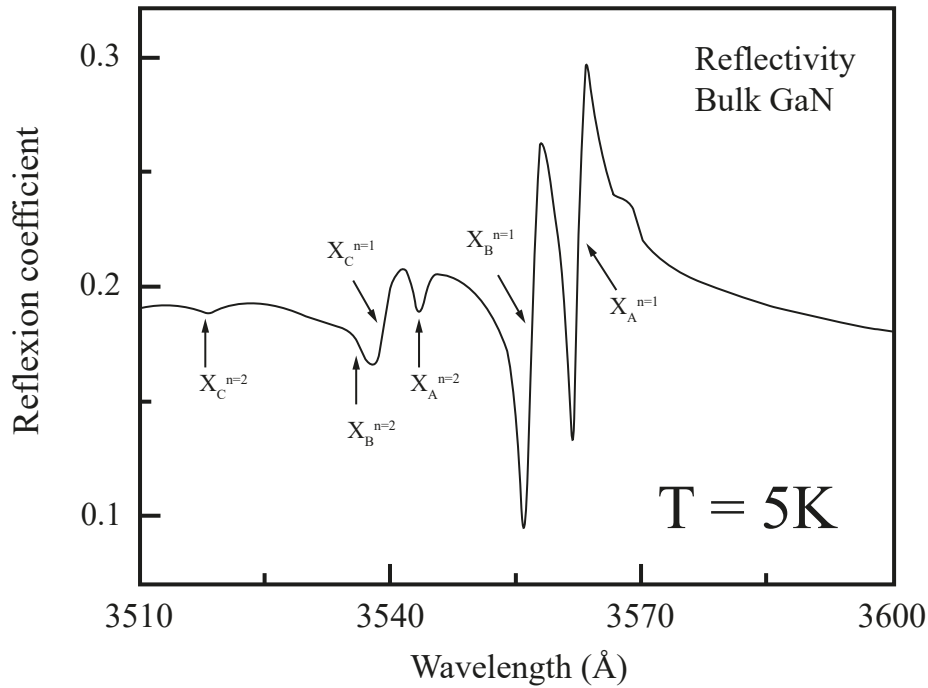


Figure II.7 – Example of reflectivity spectrum of bulk GaN highlighting excitonic transitions near the gap [104]

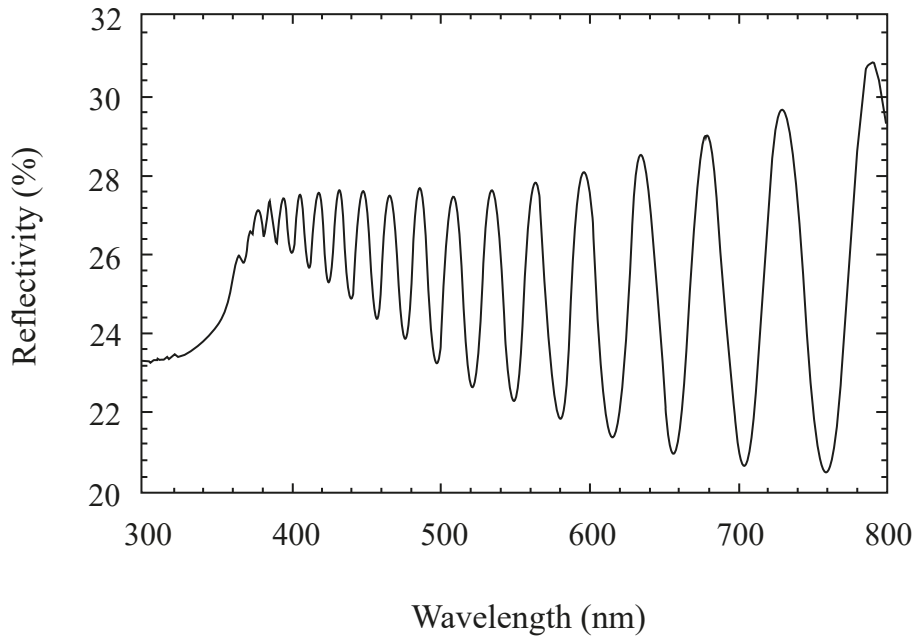


Figure II.8 – Reflectivity of GaN in the 300—800 nm wavelength range. [105]

Figures II.7 and II.8 show a typical spectra obtained on a GaN sample epitaxial on sapphire. Three different behaviors are observed:

1. Beyond the wavelength corresponding to the band gap of GaN (around 358nm) the material is transparent and the light is partially reflected at the interface with the substrate. If the thickness of the layer is smaller than the coherence length of the light, we observe constructive interference in the form of oscillations as can be seen on II.8.
2. At the excitonic transitions, the reflectivity is mainly sensitive to free excitons as they have a large density of states. In a heavily doped semiconductor, a signal related to bound excitons can also be detected. The important modification of the optical index by the excitonic resonances induces a strong variation of the reflection coefficient. The shape and the amplitude of the signal corresponding to the excitons strongly depend on the broadening and the intensity of the transition (oscillator strength) as well as on the parameters of the studied structure (thickness and nature of the layers).
3. For short wavelengths (UV), GaN is strongly absorbing and the light can only probe a small thickness. The reflection spectrum presents a quasi-constant value since the real (refractive index) and imaginary (extinction coefficient) parts of the optical index do not vary significantly.

II.3 Experimental setup

The light beam, after focusing, is detected by a CCD camera coupled to a HR-640 spectrometer. A beam expander can be added in the laser path to increase the illuminated area on the objective and reform a beam of parallel rays. It allows to obtain a better focalization of the beam onto the sample.

Finally an optical density is used to attenuate the power density on the sample. For low temperature observations, the cooling of the sample is ensured by a closed loop helium circulation cryostat.

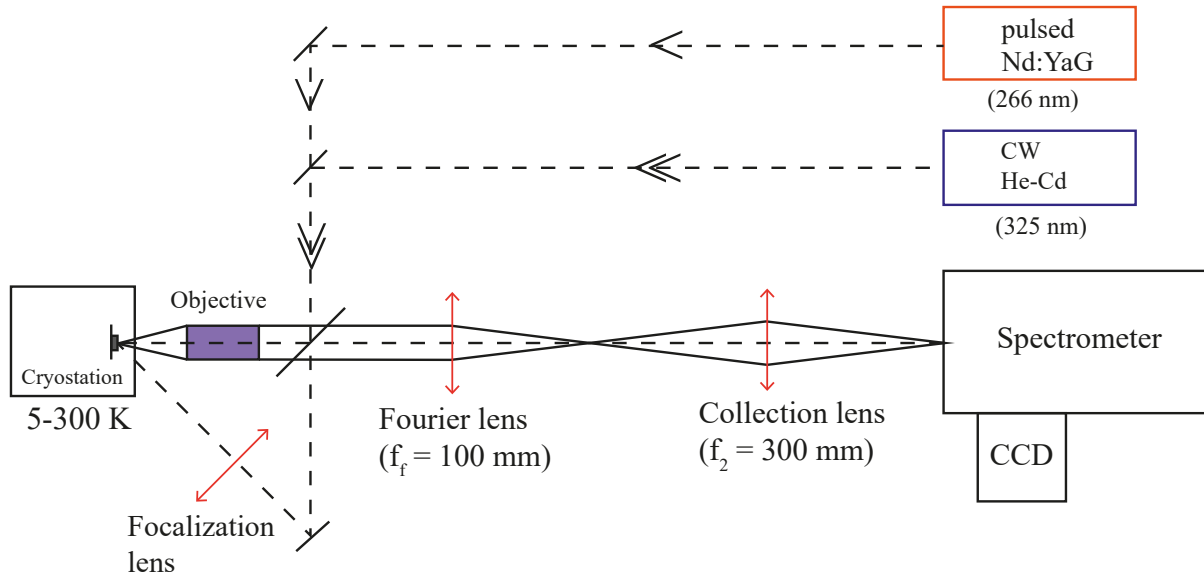


Figure II.9 – Schematic presentation of the available optical elements including excitation sources, beam splitters, lenses separators, lenses, an objective, the sample in the cryostat and the spectrometer associated with a CCD camera. The experimental setup including the removable Fourier lens allows to perform Fourier imaging and by removing it, the real space imaging can be obtained as explained on part II.3.3.

This setup is also used for reflectivity since a white light can illuminate the sample through the objective. This setup is well adapted to position-dependent measurements because it is possible to finely move the sample holder laterally and vertically with a piezoelectric controller while keeping an excitation and a detection at normal incidence. The use of a diaphragm allows to select the detection angle if necessary.

II.3.1 Micro-photoluminescence

Because of its high absorption coefficient at low wavelengths (for an energy higher than the band gap energy: $\alpha \approx 1.5 \cdot 10^5 \text{ cm}^{-1}$), GaN is not well suited for transmission measurements. Only thin layers (of the order of less than hundred nanometers) transmit enough light for detection. This technique is therefore reserved for transparent materials such as dielectrics. It is necessary to specify that the spectroscopy techniques used for bulk and nanowires requires measurements as a function of the angle of detection (photoluminescence) or incidence (reflectivity). Finally, the study of samples at low temperature is also useful to avoid lattice vibrations (phonons) which cause an important homogeneous broadening of the optical transitions. Each experimental setup is associated with a cryostat in order to lower the temperature to 5K.

Our setup, allows to perform microphotoluminescence and micro-reflectivity experiments. The

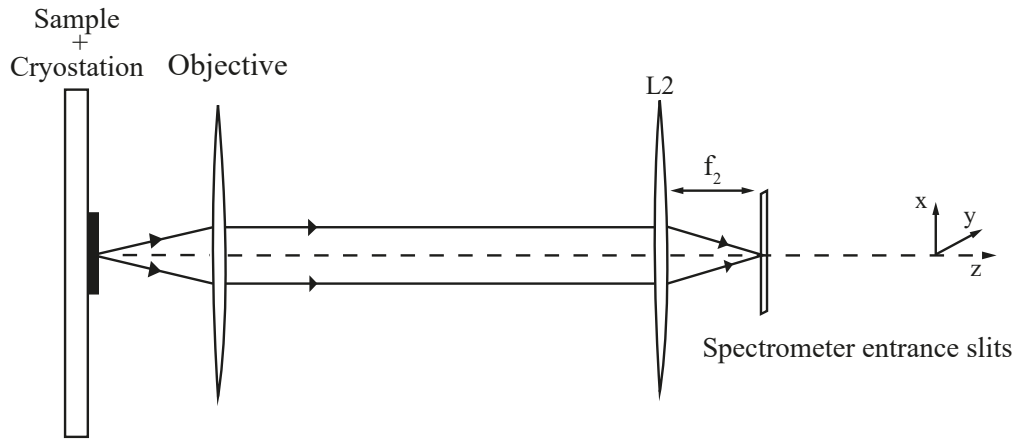


Figure II.10 – Scheme of micro-photoluminescence

laser beam is focused on the sample through a microscope objective of very short focal length in order to reduce the diameter of the spot on the sample to $1\ \mu\text{m}$.

II.3.1.1 Objectives

Two objectives, Thorlabs or Mitutoyo, are used, the first for direct excitation and the second for lateral excitation obtained through an aspherical lens. Their transmission is presented below. Both objectives can be used for visible light imaging. But only the Thorlabs has a correct transmission in the excitation range (266nm for Q-switched and 325nm for HeCd). The characteristics of the two objectives are detailed in the table II.1.

Objective	f_{obj} (mm)	NA	Resolution pwr (nm)	Magnif. (f_2/f_{obj})	Spatial resolution (nm)
Thorlabs	10	0,4	549	30	867
Mitutoyo	2	0,5	439	150	173

Table II.1 – Characteristics of Thorlabs and Mitutoyo objectives, in order the focal length of the objective, the numerical aperture (NA) and the resolving power (all three at 360nm), the magnification of the system by combining the objective and the collection lens (L2) and the theoretical spatial resolution obtained with the CCD ($1\text{pixel} = 26 \times 26\ \mu\text{m}^2$)

The resolution power is obtained by taking the expression of an Airy function describing the intensity expression of a classical diffraction pattern and applying the Rayleigh criterion. Two diffraction spots are distinct provided that the maximum of one corresponds to the minima of the other. This leads to a resolving power $\Delta_x = 1.22 \frac{\lambda}{a} f_{\text{obj}}$. The spatial resolution corresponds to the size of a pixel (26m) divided by the magnification of the system. In the case of the Mitutoyo, the spatial resolution of (173nm) is certainly better than that of the Thorlabs (867nm) but it is actually limited by its resolving power (only 439nm and 549nm for the Thorlabs).

II.3.1.2 Spectrometer

The spectrometer and the CCD camera are essential parts in the acquisition of our results. The spectrometer will allow us to obtain the spectral resolution on the image while the CCD camera will transform the light signal into an analog signal and make the acquisition.

The collection of the photoluminescence or reflectivity signal is focused on the entrance slit of a Jobin-Yvon spectrometer with a focal length of one meter, equipped with a 1200 or 2400 lines/mm grating (blasted at 330 nm), associated with a CCD camera featuring 1024×256 pixels; the surface of each pixel is $26\mu\text{m}^2$.

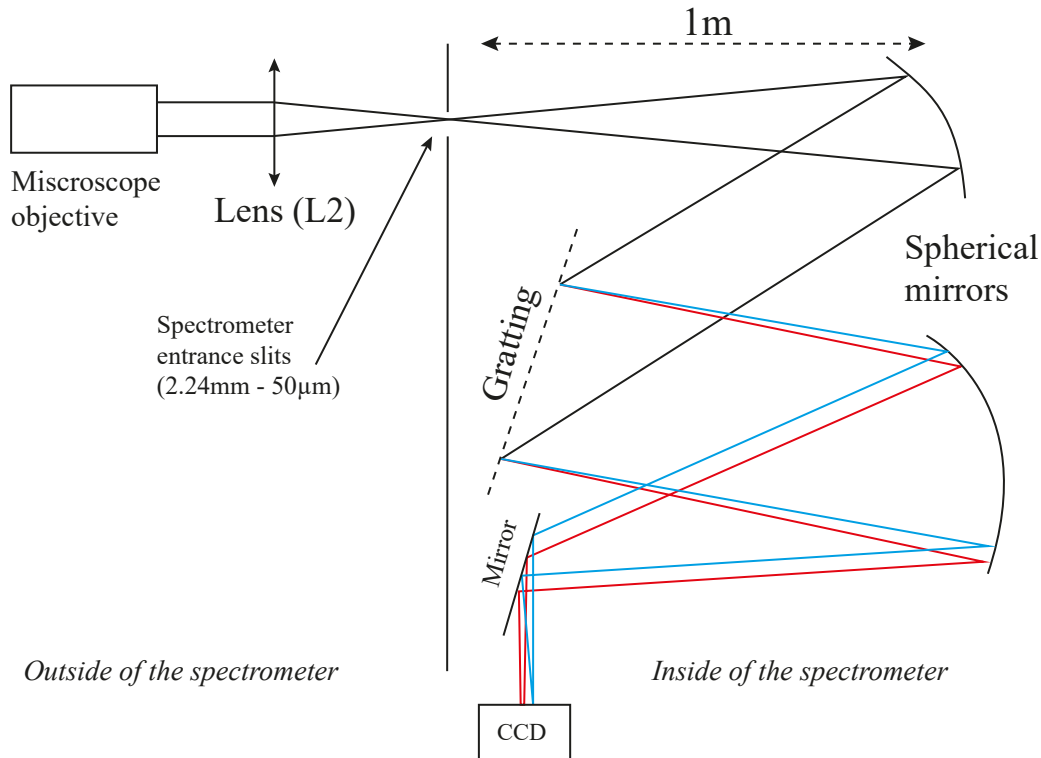


Figure II.11 – Schematic representation of a spectrometer

The image of the luminescence enlarged by the microscope objective is focused at the entrance slit of the spectrometer (which is of variable width to increase the amount of collected light or spectral resolution). As it is depicted in Figure II.11, one meter away, the rays are reflected on a spherical mirror which will form a beam of parallel rays to a grating. This will deflect the different wavelengths to a greater or lesser extent. Thanks to another spherical mirror, the identical wavelengths will be focused at a point at the output slit of the device. At the end of the optical path a plane mirror reflect the focused image on the CCD camera.

II.3.1.3 Laser sources

Two laser excitation sources were used for the photoluminescence experiments, a continuous and a pulsed laser, these two lasers allow to measure a wide range of power densities. These sources are

listed below: - Continuous He-Cd laser emitting at 325 nm. - Q-switched Nd YAG laser, quadrupled in frequency at 266 nm, with pulses of 400 ps length and a repetition rate of 20kHz.

II.3.2 Gaussian spot size determination

The spot shape and size is essentially dependant of the objective and the excitation laser configuration. The spot surface determination is straightforward in our confocal setup as the full 2D image of the spot is measurable. However the objective is not usable in some case (the optical transmission of the confocal objective does not allow to excite at 266nm), and excitation from the side is required. The shifted spot then takes the shape of an elliptical Gaussian spot.

In order to determine the area of a spot formed by a Gaussian beam, it is necessary to define a diameter by fixing a minimum intensity marking the edge of the spot. The two extremities of the diameter are those for which the intensity value is equal to the maximum intensity I_{\max} at the center of the Gaussian [106] divided by e^2 . For a Gaussian beam propagating in a given direction, the intensity profile is given by:

$$I(x, y) = I_{\max} e^{-\frac{2x^2}{w_x^2}} e^{-\frac{2y^2}{w_y^2}} \quad (\text{II.13})$$

where w_x and w_y are the half-axes of the elliptical spot defined at $\frac{1}{e^2}$. The surface intensity is then calculated from the power P_P of the beam as detected by the power meter divided by the surface S_e of the excitation spot given by :

$$P_P = I_{\max} \int_{-\infty}^{+\infty} e^{-\frac{2x^2}{w_x^2}} dx \int_{-\infty}^{+\infty} e^{-\frac{2y^2}{w_y^2}} dy = I_{\max} \frac{\pi}{2} w_x w_y = I_{\max} S = I_{\max} \frac{S_e}{2} \quad (\text{II.14})$$

where S_e is the ellipse surface, i.e. $S_e = \pi W_x W_y$.

II.3.3 Real-space imaging

The main interest of our equipment lies in its versatility, it is possible to adapt the setup at will in order to collect precise information. The luminescence emitted from the sample passes through an objective and is focused through an other lens so that the image of the sample is made on the entrance slit of the spectrometer. The collected luminescence is then dispersed by the grating and finally measured on the CCD. By using this image mode, the zero order of the grating is used thus behaving like a mirror. The measurement gotten from this setup features spatially resolved length on both axes, imaging the real space.

This technique is notably convenient to observe the surface behavior of the sample under the spot as well as to measure the size of the spot, a critical parameter that confers various physical effects such as the power density to which the sample is subjected. The maximum aperture of the entrance slit of the spectrometer is 2.24 mm and ultimately limits our observation of the sample.

Experimentally, the alignment of the detection line is carried out before the excitation line thanks to a green laser entering by a side slit of the spectrometer and emerging from the entry slit of the spectrometer, at the place where the luminescence and reflectivity beams will be focused. Whatever the detection configuration, a collecting lens of focal length $f_2 = 300$ mm focuses the photoluminescence or reflectivity on the entrance slits of a 1200 line/mm grating (blazed at 330nm). Thanks to a motorized support, the collection lens can be moved horizontally which allows to change of the spectrometer the zone of the sample analyzed on the slits. In the configuration presented in figure II.12, a Thorlabs objective of focal length $f_{obj} = 10$ mm is used, having a numerical aperture $NA = 0.4$, which corresponds to an angle of detection with respect to the optical axis of the system of 23.6° .

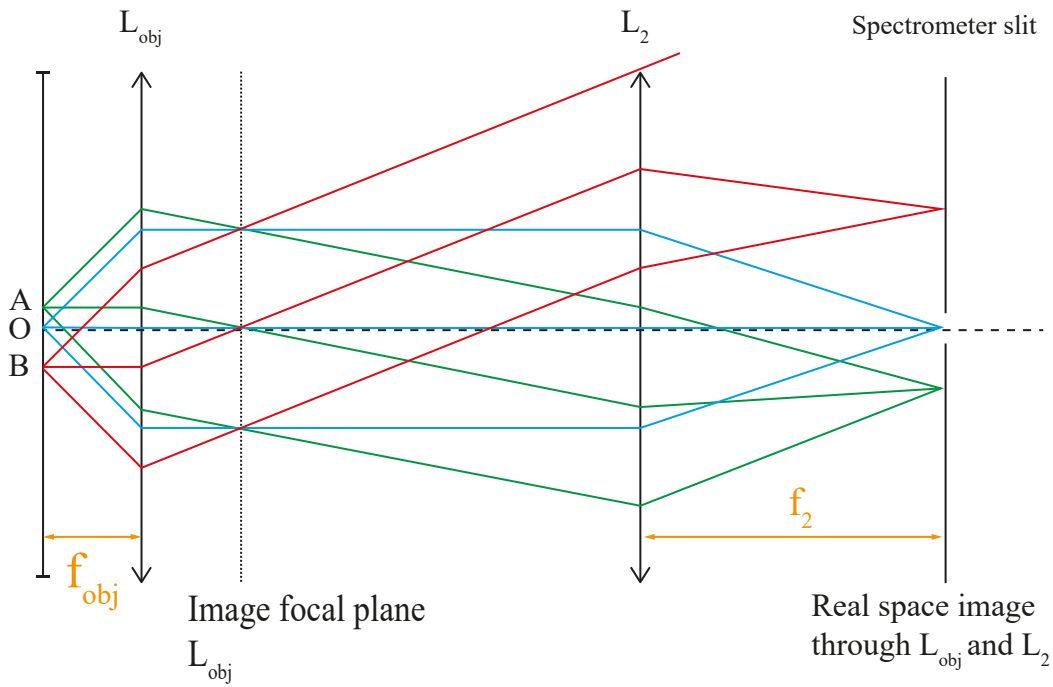


Figure II.12 – Principle of real space imaging with a focal length f_{obj} objective and collection lens with a focal length f_c . The rays coming from the same point on the sample surface are focused on the spectrometer slit. For points O and A , all rays are collected by the spectrometer while for point B , part of the emitted rays are lost which decreases the intensity detected by the spectrometer.

The luminescence of the sample is collected by the same objective and then focused by the collection lens L_2 on the entrance slit of the spectrometer. The magnification G of the system is given by the following equations:

$$G = \frac{f_2}{f_{obj}} \quad (\text{II.15})$$

Thus for the Mitutoyo lens and the Thorlabs lens:

$$G_{\text{Mitutoyo}} = \frac{300}{2} = 150; G_{\text{thorlabs}} = \frac{300}{10} = 30 \quad (\text{II.16})$$

As equations II.16 shows, imaging with the Mitutoyo lens results in a much higher magnification.

II.3.4 Fourier imagery

Fourier imaging gives access to the angular dispersion of polaritons as a function of wavelength and thus access to the polariton dispersion relation which is rich in information on the type of coupling, the condensation of polaritons and can even be used to determine the oscillator strength at a given power. In this setup, all the rays emitted with an angle θ are focused at the same point on the vertical entrance slit of the spectrometer. In order to locate the Fourier plane, a sheet of paper is moved until the most focused light spot is observed. With the help of the collecting lens, the image of the Fourier plane is formed on the entrance slit of the spectrometer. The amplitude at the entrance slit is given by the Fourier transform of the amplitude in the Fourier plane. The focal plane image of the objective and the focal plane object of the Fourier lens are merged and form a plane called Fourier plane.

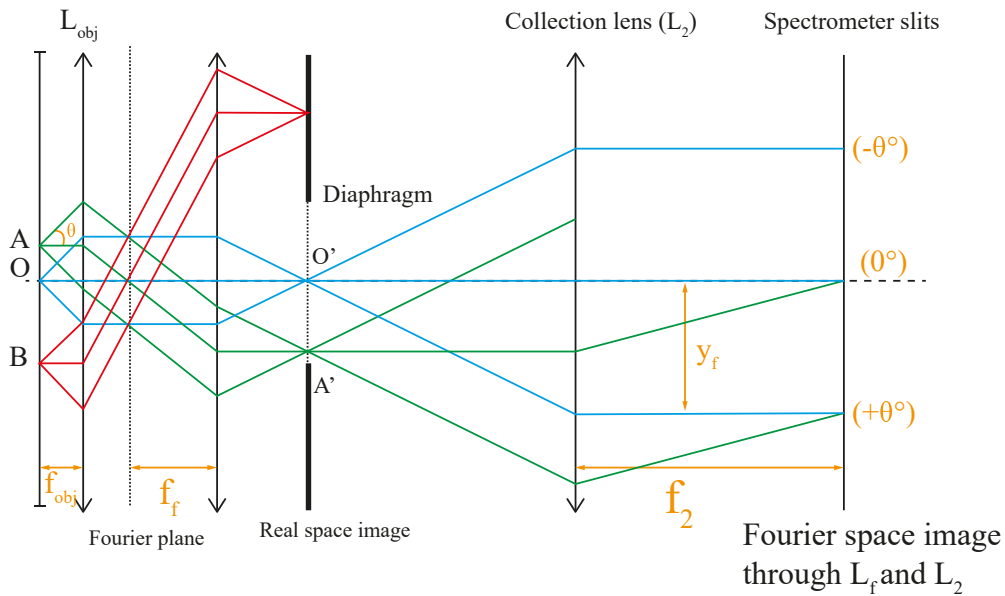


Figure II.13 – Fourier imaging with spatial filtering applied to the rays coming from 3 points (O, A and B) located at the surface of the sample with an objective of focal length f_{obj} , a Fourier lens of focal length f_f and a collection lens of focal length f_2 . For each point, one ray is emitted parallel to the optical axis and two others with an angle $\pm\theta$. The rays emitted with an angle θ whatever the point of origin are focused on the spectrometer slit at a height y_f . Spatial filtering allows to select a spatial area (circle of radius OA) where point O is located on the optical axis and point A corresponds to the limiting case where the rays (in green) pass the diaphragm. The rays coming from B (in red) further away from the optical axis are blocked by the diaphragm.

In our experimental setup, the configuration, as shown in figure II.13 uses in detection a Mitutoyo objective of focal length $f_{obj} = 2$ mm having a numerical aperture $NA = 0.5$, which detects the angles included between $\pm 30^\circ$ with respect to the optical axis of the system. This objective will be preferred to the Thorlabs one because it allows to collect a wider range of angles. In order to access the angular distribution of the emission, a second lens, called Fourier lens, of focal length $f_f = 100$ mm is placed between the collection lens of focal length $f_c = 300$ mm according to a configuration respecting two

conditions as illustrated on figure II.9.

II.4 Time-resolved optical spectroscopy

II.4.1 Principle

In optoelectronic devices, the relaxation dynamics of the carriers plays a crucial role for the light emission effects and their efficiency. The mechanisms involved are related to radiatives and non-radiative recombination between electrons and holes, as well as to the diffusion of charges to other energy states of the system. The emission of light in a semiconductor is directly related to the lifetime of the excited state. This time, also called radiative recombination time (τ_R), can be estimated from the probability of optical transition between the excited state and fundamental level of a two-level system, for a bound state is written:

$$\tau_R = \frac{2\pi\epsilon_0 m_0 c^3}{n e^2 \omega^2 f_{\text{osc}}} \quad (\text{II.17})$$

where f_{osc} is the oscillator strength of the optical transition, n the refractive index of the semiconductor material, ω the energy of the optical transition. The presence of crystalline defects, makes that electrons and holes do not only recombine radiatively, but that a non-radiative path is possible. The effective decay time of the measured photoluminescence is the result of a combination of these two competing processes (τ_R being the radiative lifetime, and τ_{NR} the non-radiative lifetime) giving of global lifetime (τ):

$$\frac{1}{\tau} = \frac{1}{\tau_R} + \frac{1}{\tau_{NR}} \quad (\text{II.18})$$

II.4.2 Experimental setup

II.4.2.1 Laser source

We have at our disposal a femtosecond chain allowing us to make time resolved photoluminescence (TRPL) experiments. In this paragraph we will only present the components of the femtosecond chain. The VERDI V10 laser can deliver pulses with a width of less than 150fs and a repetition rate of 76MHz. A sapphire crystal doped with titanium ions is used as the amplifying medium in a wide wavelength band ([700 nm, 1000 nm]). The focusing of the beam in the crystal by non-linear effect (Kerr lens) for high peak powers allows the formation of pulses (mode locking). In order to maintain the operation in pulsed mode, it is necessary to keep the beam in phase inside the cavity. To compensate for the positive phase shift of the mirrors, a negative phase shift is introduced by the use of two prisms. The "pulsed" operation requires the contribution of an initial pulse by the starter (oscillating

element). The Verdi laser is used as an optical pump of the femtosecond laser MIRA 900 F. This laser features a maximum output power of 1.5 W. The adjustment of the device requires the alignment of the different mirrors but allows to work on a large range of wavelengths without additional constraints. The beam can then be doubled or tripled in frequency thanks to a non-linear crystal to reach the UV range (ranging from 400nm to 250nm). This type of laser is useful both to probe phenomena with a short time scale (radiative de-excitations) but also to obtain high peak power with an adjustable wavelength.

II.4.2.2 Streak camera

The streak camera is a device which converts temporal information, originating in a light-emission event, to spatial information. The principle of a streak camera is shown in figure II.14. The light coming from the sample, passes through the entrance slit of the streak camera and through the optical system which forms the image of the slit on the photocathode of the streak camera tube. At the entrance of the tube, the intensity of the light signal has a temporal distribution in the direction of propagation and a spatial distribution in the direction of the slit that corresponds to the spectral decomposition of the signal. The light incident on the photocathode is then converted into a number of electrons proportional to the intensity of the light. The optical pulses on the photocathode are thus converted sequentially and proportionally to the intensity of the light into electrons, while keeping the temporal shape of the incident signal [100].

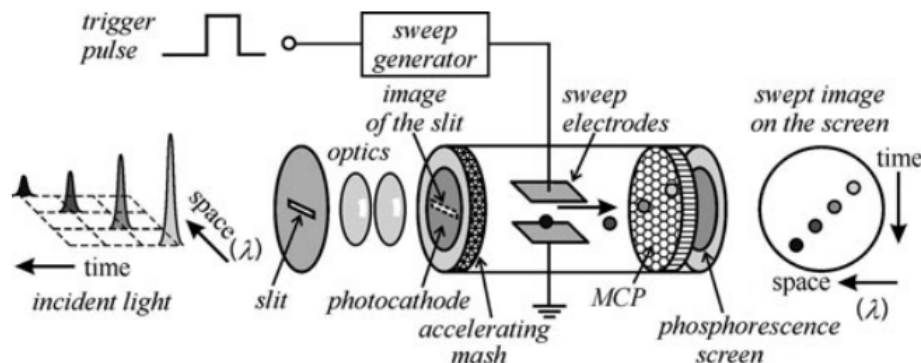


Figure II.14 – Operation schematic of a streak camera. The light pulse passing through the entrance slit and hitting a photocathode induces emission of photoelectrons inside an evacuated tube. Photoelectrons are accelerated along the horizontal direction (i.e. the direction of the incoming light) by a voltage applied between the photocathode and a metal mesh and subsequently deflected by a high voltage in the vertical direction. Upon impinging on a phosphorescence screen, the photoelectrons produce a phosphorescent trace with spatial distribution of intensity corresponding to the temporal profile of the incoming pulse. After [100]

The electrons are accelerated in an electric field produced by the sweep electrodes. Electrons are thus deflected by a high sinusoidal voltage in the direction perpendicular to the streak camera slits. A trigger signal from a picosecond pulse laser, which produces the excitation of the sample,

will trigger the application of a high voltage field on the electrodes. This deflection voltage is applied synchronously with the incoming light pulses and varies in time so that electrons arriving at different times are scattered at different angles in the vertical direction. We thus have a deflection of the electrons according to their time of arrival between the electrodes. In their way towards the phosphorescent screen, electrons undergo multiplication via secondary electron emission in the micro-channel plate, then on the cathode screen are reconverted into luminous spot. The spot on the screen corresponding to the earliest arriving optical pulse is placed in the highest position, the other spots being arranged in sequential order from top to bottom. In other words, the vertical direction on the phosphorescent screen serves as the time axis. The brightness of the various spots on the screen is proportional to the intensity of the incident optical pulses. The position in the horizontal direction of the image on the screen corresponds to the horizontal position of the incident light from the monochromator. The phosphorescence image is then recorded (e.g. by a photodiode array or a CCD detector). By calibration, we find the correspondence between the horizontal position and the wavelength. In this way, the streak camera can be used to measure the temporal and spectral characteristics of the emerging optical pulses of the samples (time resolved photoluminescence, time resolved reflectivity etc.). The limits of such a device are given by the scanning speed of the electrons in the tube (the resolution limit of our equipment is 0.9ps), by the size of the entrance slit and by the focusing optical system on the photocathode.

The temporal resolution is also directly affected by the grating used in the experiment since the optical path is deviated differently depending on the number of grooves, causing a temporal dispersion. The relationship between the temporal dispersion and the grating is given by the following equation:

$$\delta t = \frac{W}{c} \times \frac{k\lambda}{d} \quad (\text{II.19})$$

with W the effective length of the grating, c the speed of light, k the order of diffraction and λ the wavelength of diffraction. We see with the previous equation that the more the grooves number (in mm) is large, the more the temporal deviation will be important. Our experimental setup is equipped with three gratings of 300, 600 and 2400 lines. The ultimate resolutions for a wavelength of 350nm are respectively 3, 6 and 13ps.

II.5 Conclusion

To conclude this chapter, the main experimental techniques were presented as well as all our equipment. This chapter introduced the micro-photoluminescence and TRPL techniques with their typical expected results (i.e. μ -PL spectra and decay time measurements): the study of the different optical recombinations on the samples will constitute the major part of the expected and studied results.

The realization of advanced spectroscopy campaigns and the processing of results in order to further increase knowledge in the optical characterization of the various samples requires a perfect

control of the experimental conditions. The diameter of the spot, the type of objective and their transmission are the most important as they directly influence the zones probed in the samples and are essential parameters for the analysis of the results (power density, calculation of carrier density). It has been seen in this chapter that our equipment brings a great flexibility to the studies carried out with the possibility of imaging in real space, in Fourier space but also to study the temporal decay of the carriers thanks to the streak camera. The results of the different experimental campaigns will be presented in the next chapter and are the result of many optimizations of the spectroscopy benches whose equipment has been presented.

Determination of the excitonic Mott density in a GaN bulk sample

III.1 Context: excitonic binding energy scaling law

To recall the introductory part on the Mott transition (I.7.3) with the increase of the excitation density several competing many-body effects need to be taken into account, as large exciton or electron-hole densities reveal the composite nature of excitons. Coulomb exchange interaction and band filling, arising from the Pauli exclusion principle, lead to a lowering of the overall electrostatic energy and a blueshift of the excitonic transition energy. Secondly, the screening of the Coulomb interaction results in a bandgap red-shift and a decrease of both exciton binding energy and oscillator strength. In the case of a 3D material with non-resonant excitation, the screening of the Coulomb interaction is the most efficient effect and the bandgap shift induced by the screening compensates nearly exactly the reduction of the exciton binding energy [107]. Therefore, it is observed that the exciton transition energy remains locked for densities ranging from zero up to the Mott density. The oscillator strength decreases progressively and excitons are dissociated into an electron-hole plasma [108]. This phenomenon referred as the Mott transition is not abrupt and depends upon the temperature. At the critical Mott density, excitons are no longer present in the material.

Experimental, in cm^{-3}	Reference
2.2×10^{19}	Hess[109]
$6 \times 10^{18} - 5 \times 10^{19}$	Khym[66]
1×10^{18}	Fischer[110]
$1.8 - 3.8 \times 10^{18}$	Binet[111]
6×10^{16}	Present work

Table III.1 – Overview of experimental and theoretical Mott densities at low lattice temperatures equal or smaller than 10K. Estimations of Mott densities obtained from the data provided by each source.

Table III.1 summarizes the experimental values of the Mott densities reported in the literature for GaN with lattice temperatures lower than 10K [109, 66, 110, 111]. The reported data for GaN Mott transitions varies from 1×10^{18} to $5 \times 10^{19} \text{cm}^{-3}$. The value obtained from the current experiments is also indicated. It is interesting to establish a comparison between ZnO and GaN experimental values, as a scaling law between those two materials can be established thanks to their excitonic Bohr radii. Versteegh et al. have carefully studied the exciton screening in ZnO at 300K through pump-probe reflectivity measurements[68]. In order to obtain an homogeneous carrier density within the penetration of the reflected probe, they induced in the material a three-photon absorption with the 800 nm laser pulses of a Ti-sapphire laser. The Mott density in ZnO deduced from the experiments is $1.5 \times 10^{18} \text{cm}^{-3}$. In addition, previous work by Klingshirn et al. leads to the conclusion that the ZnO excitonic Mott density is equal to $5 \times 10^{17} \text{cm}^{-3}$ and displays a weak temperature dependence [49].

It thus appears that the reported values for GaN Mott transition are equal to or higher than those of ZnO. However the latter exhibits a larger excitonic binding energy in comparison with that of GaN (60 meV versus 25 meV). Furthermore, it should be noted that because of the GaN larger Bohr radius (4.2 nm for GaN versus 1.8 nm for ZnO), the excitonic Coulomb interaction screening with the increase of the excitation intensity should be more efficient in GaN than in ZnO. In view of these results, it can be concluded that the excitonic Mott density in bulk GaN needs to be revisited. This chapter will present the experimental methodology used to determine the excitonic Mott transition: first, the optical characterization is done on the reference sample with temperature and power studies campaign. A focus will be presented on the time-resolved photoluminescence campaign and the exploitation of its results in order to calculate experimental carrier concentration. Finally, the results will be discuss in regard to the literature and their physics interpretation.

III.2 Sample presentation

In the following paragraph the reference sample used in our experimental campaign is presented. A first study is shown in order to consider the different optical transitions that can be observed by photoluminescence before going into more detail in the fine optical characterization part.

III.2.1 Bulk GaN reference sample : H46-2

The sample is a $350 \mu\text{m}$ thick freestanding GaN layer, unintentionally doped, which has been grown by hydride vapor phase epitaxy (HVPE). It is of high crystalline quality, with a dislocation density between 10^6cm^{-2} and 10^7cm^{-2} [112, 104]. As it will be presented in the following chapter, this simple reference structure exhibits nicely sharp photoluminescence spectra and display neatly the free excitons optical transitions. The estimated residual donor concentration inherited from the grown process is of the order of 10^{17}cm^{-3} [113]. This sample has already been studied by Ouloum Aoudé [62] and figures III.1 and III.2 are taken from this work.

III.2.2 Temperature study

The temperature study allows to follow the evolution of the different optical transitions for a given power density as a function of the temperature of the sample. This study is conducted on a single identified area using by identifying a characteristic defect as a reference position in the sample, far enough to avoid any impact on the measurements. This identification is made in order to ensure that the results are effectively given from the sample and not generated from an inhomogeneity. The H46-2 sample was studied by photoluminescence as a function of the temperature between 5 and 300 K. The spectra measured are presented in the figures III.1 and III.2. The identification of the different peaks requires the superposition of the photoluminescence spectra with those of reflectivity. First the analysis of the PL spectra at low temperature is made in order to introduce the optical transitions to be finally presented with different temperatures.

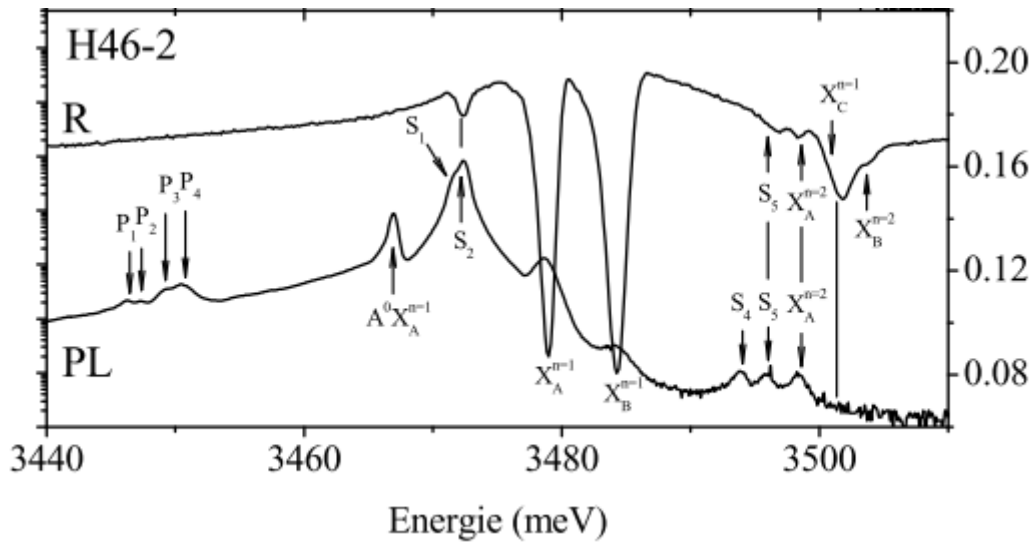


Figure III.1 – Reflectivity (R) and photoluminescence (PL) spectra of H46-2 sample, from [62]

We observe very clearly the presence of the two excitons $X_A^{n=1}$ and $X_B^{n=1}$, these two excitons are located around 3478.5 and 3484 meV respectively on the reflectivity and photoluminescence spectra of figure III.1. The split-off valence band exciton $X_C^{n=1}$ is also visible on the reflectivity spectra around 3501 meV but hardly observed on the photoluminescence spectra; its absence at low temperatures is attributed to the thermalization of excitons on the low energy states. Indeed, the PL spectra are essentially dominated by excitons bound to impurities.

On figure III.1, between 3471 and 3472 meV, two peaks S_1 and S_2 are observed. S_2 is also observed on the reflectivity spectra. By increasing the temperature, these peaks maintain an almost constant intensity ratio while attenuating compared to the $X_A^{n=1}$ excitonic peak. Having the same behavior, S_1 and S_2 are associated with two donors of different nature trapping $X_A^{n=1}$ excitons. Their identities have been discussed by several authors. They would be neutral donors attributed respectively to oxygen and silicon according to Wyszomolek et al [114] and they would be respectively an ionized donor and a neutral donor attributed to oxygen according to Freitas et al [115]. Having the

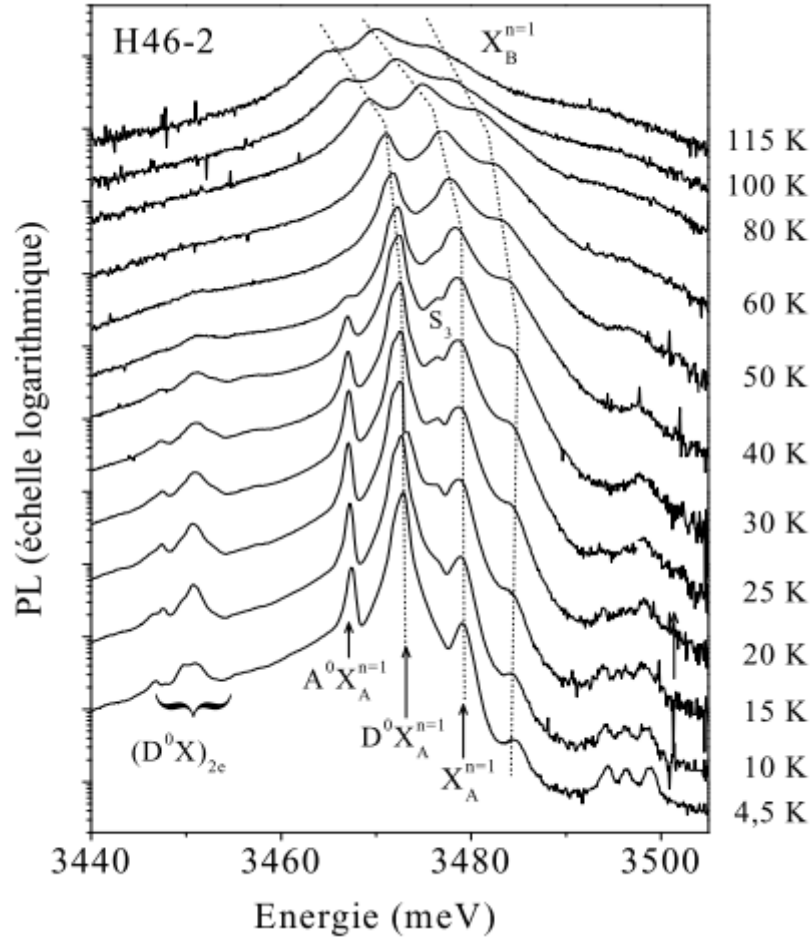


Figure III.2 – Photoluminescence spectra of sample H46-2 as a function of temperature, from [62]

energy of $X_A^{n=1}$ and the energies of the two peaks S_1 , S_2 , we can calculate the localization energies of $X_A^{n=1}$ on these two impurities. We find 7 to 8 meV for S_1 and 6 to 7 meV for S_2 . Between S_2 and $X_A^{n=1}$, one localizes a small peak S_3 in luminescence (around 3476 meV) which intensifies by increasing the temperature and disappears quickly starting from 50 K as shown in figure III.2; this peak is a priori a donor trapping an exciton with a localization energy of approximately 3 meV compared to $X_A^{n=1}$. The identification of this peak is also discussed in the literature. It is thought to be the $X_B^{n=1}$ exciton trapped on a neutral $D^0X_B^{n=1}$ donor according to Fischer and Pakula et al [116, 117], it would be the excited state of a $D^0X_A^{n=1}$ according to Teisseyre et al. [118], and finally it would be the $X_A^{n=1}$ exciton trapped on a neutral surface donor $D^0X_A^{n=1}$ of energy of the order of 14-19 meV according to Volm and Calle et al. [119, 120].

At the highest energies, we observe three peaks S_4 , S_5 and $X_A^{n=2}$ around 3493.6, 3495.8 and 3498 meV respectively. By increasing the temperature, the peak with the highest energy becomes wider and relatively more intense than the other two neighbors. This peak is identified with an intrinsic excited transition that is attributed to the $X_A^{n=2}$ exciton. On the other hand, the two other peaks S_4 and S_5 disappear progressively with temperature, this disappearance being explained by the release

of bound excitons activated by temperature. Therefore, we can say that these two peaks probably correspond to neutral (or ionized) donors trapping free excitons that would be $X_A^{n=2}$ [121].

The figure III.1 also shows several peaks $P_1, P_2 \dots P_6$ at lower energy. They correspond to two-electron replicas that occur when the hole and the electron of an exciton trapped on a neutral donor (D^0X) recombine leaving the donor in an excited state. Their appearance confirms the presence of shallow donors in the material and also has been observed in GaP [122], CdS [123], CdSe [124], ZnO [125] and InP [126], as well as in epitaxial GaN on sapphire [121] and self-supported GaN [46, 114].

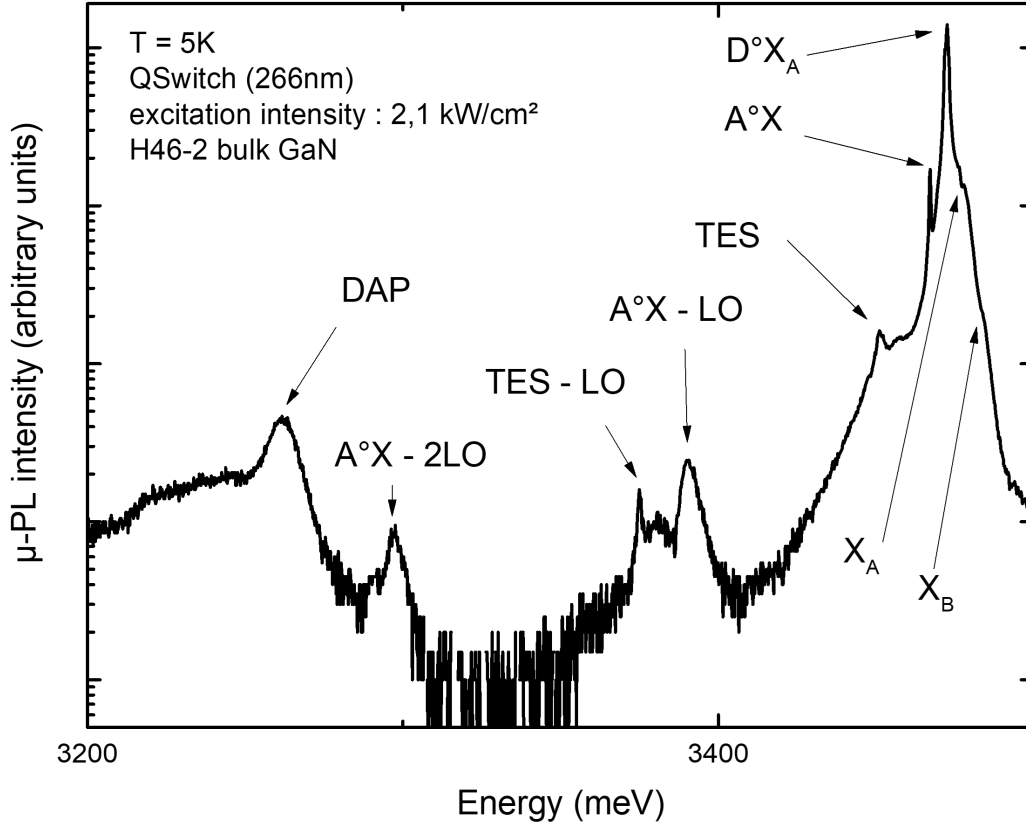


Figure III.3 – Photoluminescence spectrum of H46-2, reference GaN bulk sample at 5K.

The energy of this two-electron transition is lower than that of D^0X , as it is equal to the energy of D^0X deduced by the energy difference between the excited state and the ground state of the neutral donor. The peaks P_1, P_2 are respectively located around 3446.9 and 3447.7 meV, they constitute the two-electron transitions 1s-2s and 1s-2p related to S_1 ($D_1^0X_A^{n=1}$). Their energy differences are 24.1 and 23.3 meV respectively. The peaks P_3, P_4 are respectively located around 3449.5 and 3450.5 meV, their energy differences with S_2 ($D_2^0X_A^{n=1}$) are 22.5 and 21.5 meV respectively. These peaks are attributed to the two-electron transitions 1s-2s and 1s-2p relative to $D_2^0X_A^{n=1}$. As for the last peaks P_5 and P_6 , they are located around 3454.2 meV and 3456.2 meV respectively. According to Wysmolek et al. [114], P_5 must be a two-electron replica of the $D^0X_B^{n=1}$ transition while P_6 would be the result of the de-excitation of free excitons trapped on undetermined donors while yielding their energy to the latter which switch to excited states. By applying the hydrogen model on neutral donors,

we deduced the binding energies of the latter from the 1s-2s transition, they are 32.1 meV for S_1 and 30 meV for S_2 and these values are relative to oxygen and silicon respectively [114].

All the mains optical transitions with their associated phonon replica are also observed on the photoluminescence spectrum of figure III.3 [29]. They are listed below:

- Excitonic transitions: the B exciton is less observable while for the A exciton the luminescence intensity is relatively intense.
- The phonon Two Electron Satellites replica (TES).
- The transition associated with the donor-acceptor pairs.

The energies at which the phonon replicas are located are in agreement with the LO phonon energy found in the literature (≈ 91 meV).

III.3 Excitonic Mott transition

This part describes our experimental approach to determine the excitonic Mott transition in GaN. The first part was useful to characterize excitonic optical transitions in a good quality GaN bulk sample and the donor bound and free excitons transitions will be used later on as a reference. Micro-photoluminescence (μ -PL) and time resolved photoluminescence experiments (TRPL) are used to measure the carrier density in our sample. This carrier density measurement will be correlated to the optical characterization in order to estimate the Mott density.

III.3.1 Photoluminescence as a function of excitation intensity

Figure III.4 displays μ -PL spectra measured at a cryogenic temperature of 5 K with continuous (HeCd laser) and quasi-continuous (Q-switched laser) excitations. Only one spectrum (purple curve at the bottom) recorded with the HeCd laser is reported in this figure: it corresponds to a weak excitation of 0.66 W.cm^{-2} . Other spectra have been obtained with the Q-switched laser and excitation intensities were varying from 0.426 to 4200 kW.cm^{-2} .

The main optical transitions are clearly identified at low excitation levels. The recombination of excitons bound to neutral acceptors $A^\circ X$ and neutral donors $D^\circ X$ are found at 3467.2 meV and 3472.5 meV respectively. The energies of the free exciton (X_A and X_B) recombinations (3478.5 meV and 3484.3 meV) indicate that no residual strain is present in the sample [121]. The first excited state of X_A exciton ($n=2$) is also detected at higher energy (3497.5 meV).

As illustrated by the PL spectra in Fig III.4, the free-exciton lines progressively disappear with the increase of the excitation intensity and the $D^\circ X$ line peak shifts towards the low energy side. The redshift of the main luminescence peak (initially the $D^\circ X$ transition) is concomitant with the disappearance of the excitonic signature. Both features allow us to conclude that the Mott transition occurs for an excitation intensity between 10.6 and 21.2 kW.cm^{-2} . The redshift evidences the bandgap

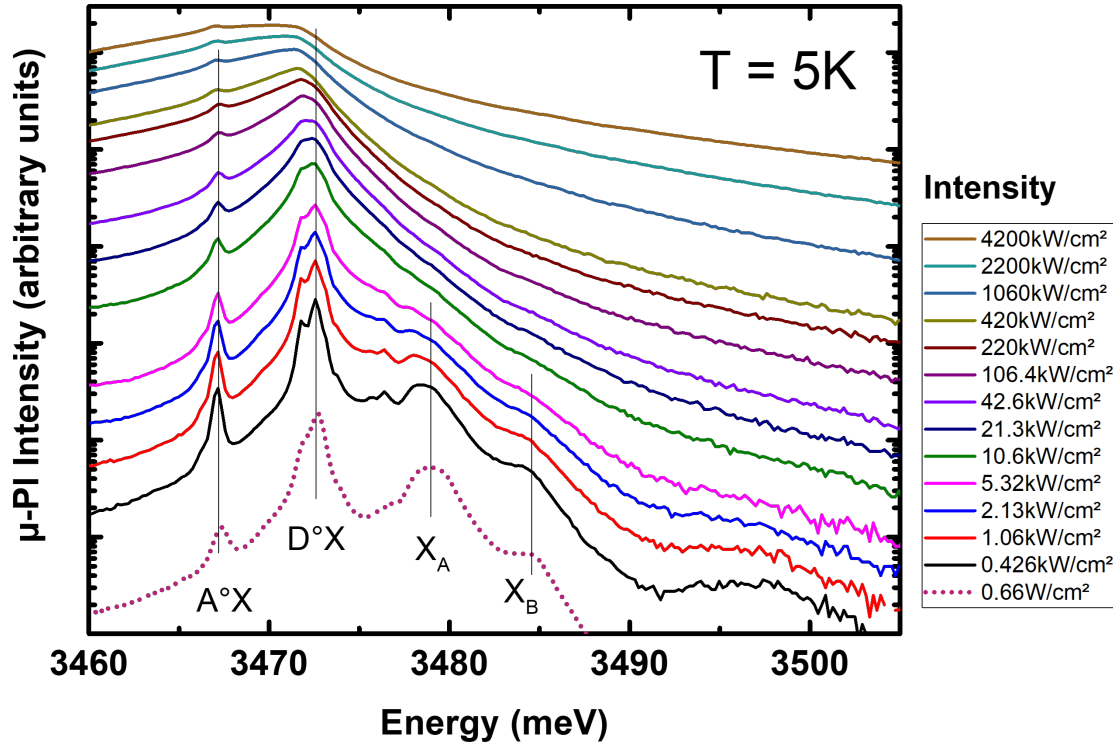


Figure III.4 – Photoluminescence spectra at 5K of the H46-2 free-standing GaN reference sample. The bottom dotted curve was measured with a HeCd laser (325nm) for a power density of $0.66\text{W}/\text{cm}^2$. The solid curves were measured with a Q-switched laser (266nm) for excitation intensities ranging from $0.42\text{kW}/\text{cm}^2$ to $4200\text{kW}/\text{cm}^2$. The main peak corresponds to the recombination of an exciton bound to a neutral donor (D°X) at 3472.5meV . The other optical transitions are identified as the recombination of excitons bound to neutral acceptors A°X at 3467.2meV , of free excitons X_A and X_B at respectively 3478.5meV and 3484.3meV . At higher energy $\text{X}_\text{A}^{n=2}$ at 3497.5meV is also detected.

renormalization with increasing carrier density. The energy of the bandgap decreases until the point where it passes below the energy of the excitons. This phenomenon occurs near the surface of the sample where the carrier density is the highest as it will be discussed in the following.

III.3.2 Electronical temperature

The electronic temperature determines the distribution of off-equilibrium carriers, as given by Boltzmann's statistics [37]. Free excitons, as free carriers are sensitive to the thermal activation of free carriers and consequently the excitonic Mott transition on the electronic temperature. Meanwhile, the crystal temperature (or lattice temperature) remains equal to 5K, given the thermal exchange between the sample and its support. The variation of the bandgap with the lattice temperature is associated with the variation of the lattice parameters and of the population of phonons, but not with the electronic temperature as it is only devoted to free carriers.

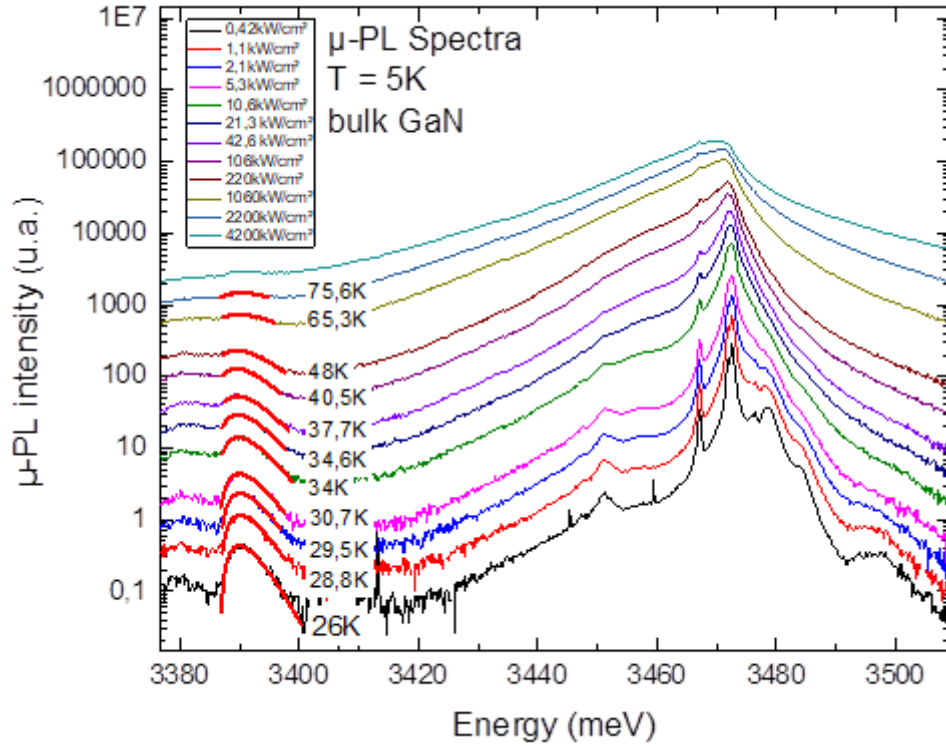


Figure III.5 – Electronic temperature extracted by fitting the first-LO replica for different power densities.

To ensure that the bandgap energy reduction followed by the redshift of D^0X line is indeed a density-dependent process induced by the optical excitation, electronic temperatures for excitation intensities below and above the vanishing of excitonic lines were extracted. Since for the lowest excitation intensities the electronic temperature (T_e) can not be extracted from the high-energy tail as commonly done [111], due to the presence of the free exciton emission, an alternative method has been employed. This method requires the fitting of the shape of the first excitonic (X_A) LO-replica by the following expression [37, 127]:

$$I_1^{lum}(\hbar\omega) \propto E_{kin}^{3/2} \exp(-E_{kin}/k_B T_e) \quad (\text{III.1})$$

with $\hbar\omega = E_{X_A} - \hbar\omega_{LO} + E_{kin}$ and where E_{X_A} is the energy of the X_A line, E_{kin} the excitonic kinetic energy and $\hbar\omega_{LO}$ the energy of the LO phonon.

The extracted electronic temperature remains near the cryostat temperature (5K), as it is equal to 26-28K for the first lowest excitation intensities obtained with the Q-switched laser. The electronic temperature calculated for continuous excitation for an excitation intensity of 0.66W/cm² (plotted in figure III.4 and not shown in figure III.6) is 31K. This value is higher than the results obtained with the pulse laser. This is due to the fact that the heat generated continuously by the HeCd excitation is more difficult to dissipate than that of the Qswitch laser as the repetition rate allows the lowering of the temperature. The electronic temperature increases to 32K for an excitation intensity of 10.6 kW.cm⁻² where the free-exciton lines are no more distinguishable.

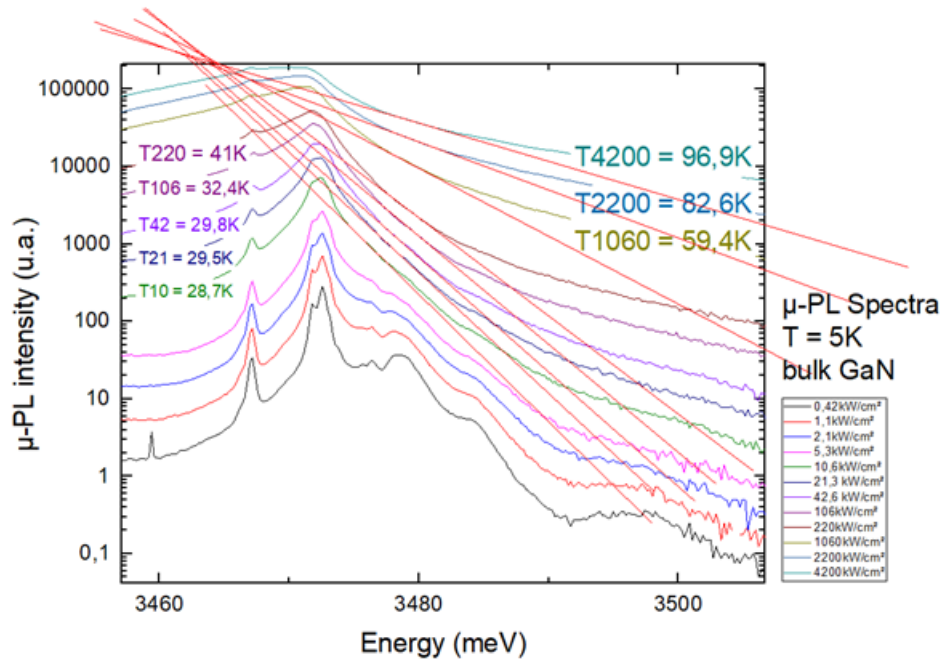


Figure III.6 – Electronical temperature fit of the high energy tail.

Power density (kW.cm^{-2})	High energy fit (K)	1-LO replica fit (K)
0.42	-	26
1.1	-	28.8
2.1	-	29.5
2.3	-	30.7
10.6	29	34
21.3	30	34.6
42.6	30	37.7
106	32	40.5
220	41	48
1060	59	65.3
2200	83	75.6
4200	97	-

Table III.2 – Electronical temperature for high energy fit and 1-LO replica fit as a function of power densities (Q-switched).

We also compare the carrier temperatures extracted by fitting the 1st phonon replica, as well as by fitting the high-energy tail in the free-exciton spectral region to verify that the 1-LO replica fit remain accurate after the vanishing of the excitons and correctly follow the heating resulting of the high excitation densities. The fit are shown on Figure III.6 and correctly match the high energy tail.

This second approach can only be implemented when free-exciton emission vanishes due to exciton bleaching (particularly above the Mott transition). As shown in table III.2, the carrier temperature

extracted from each analysis differs by, at most, 8K, and this even for excitation intensities well above the Mott transition.

III.3.3 Time resolved photoluminescence

The following described experiments are conducted in two steps in order to experimentally determine carrier concentration in our sample. In a first part, time resolved photoluminescence (TRPL) campaigns are made and are later on correlated with quasi-continuous excitation photoluminescence experiments.

Time resolved photoluminescence (TRPL) experiments were performed at 5 K in order to assess the average carrier lifetime (τ) of the electron population, which is assumed to be equal to that of the holes. All radiative and non-radiative recombination channels are grouped in a mean lifetime which depends on carrier density. The τ value is obtained through a mono-exponential fit ($y = y_0 + Ae^{\frac{-t}{\tau}}$) of the TRPL signal and is found to depend on the excitation intensity and the accurate analysis will be presented in the results discussion section. The spectra and the corresponding fits are shown on the figure III.8. The electronic temperatures were measured with the TRPL setup by the same method presented for the quasi-continuous wave experiments and were found to be around 33K. Since for the TRPL measurements the pulse duration ($t_p=150$ fs) is shorter than the carrier lifetime, the corresponding injected carrier density can be estimated at the end of the pulse duration by the following equation:

$$n_{\text{TRPL}} = \frac{I_{\text{TRPL}} \times (1 - R) \times t_p \times \alpha}{h\nu} \quad (\text{III.2})$$

I_{TRPL} , being the excitation intensity, t_p the pulse duration, α the absorption coefficient, $h\nu$ the energy of the Q-switched laser, R the reflection coefficient. The values of these parameters are $(1 - R) = 0.8$, $\alpha = 1.2 \times 10^5 \text{ cm}^{-1}$ [128].

First, the TRPL experiments are performed and the obtained results are associated with the following μ -PL quasi-continuous excitation results in order to determine the injected carriers density.

III.3.4 Determination of the injected carriers density

In this part, results from the quasi-continuous excitation experimentation are correlated with the previous TRPL results. In our case, since the duration of the quasi-continuous excitation laser pulse is larger than the lifetime of the injected carriers, it is possible to calculate the carrier density n in the steady state regime [100, 129]. It supposed that the electron (n) and hole (p) densities remain equal ($n=p$) during the optical excitation. The carrier density, if we neglect in-plane diffusion, is the solution of the following 1D spatial- and time-dependent differential equation [129]:

$$\frac{\partial n(x, t)}{\partial t} = \alpha \Phi e^{-\alpha x} + D \frac{\partial^2 n(x, t)}{\partial x^2} - \frac{n(x, t)}{\tau} \quad (\text{III.3})$$

Equation III.3 is solved for the steady state (i.e. $\frac{\partial n(x,t)}{\partial t} = 0$) and the distribution of carrier density $n(x)$ in the depth of the sample is determined, where ϕ is the photon flux given by $\frac{I(1-R)}{h\nu}$, I is the excitation intensity, τ the carrier lifetime (which depends on the particle density), $h\nu$ the energy of the Q-switched laser, R the reflection coefficient, α the absorption coefficient at this energy and D the carrier diffusion coefficient. The values of these parameters are $(1 - R) = 0.8$, $\alpha = 1.2 \times 10^5 \text{ cm}^{-1}$ and $D = 7 \text{ cm}^2/\text{s}$ [128]. The pulse duration related to the QSwitch laser is compared to the studied time constant τ . As the pulse duration is long compared to the measured τ , the steady-state approximation is valid. This leads to the carrier density expression which corresponds to the carrier density at the sample surface, where the density is largest:

$$n(x=0) = \frac{\phi\tau}{\frac{1}{\alpha} + \sqrt{D\tau}} = \frac{I(1-R)\tau}{h\nu(\frac{1}{\alpha} + \sqrt{D\tau})} \quad (\text{III.4})$$

Surface recombination is not included in this calculation since it is taken into account implicitly through the carriers lifetime, which is measured experimentally. This procedure could overestimate carrier density as the lifetime measured is not negligible compared to the pulse duration.

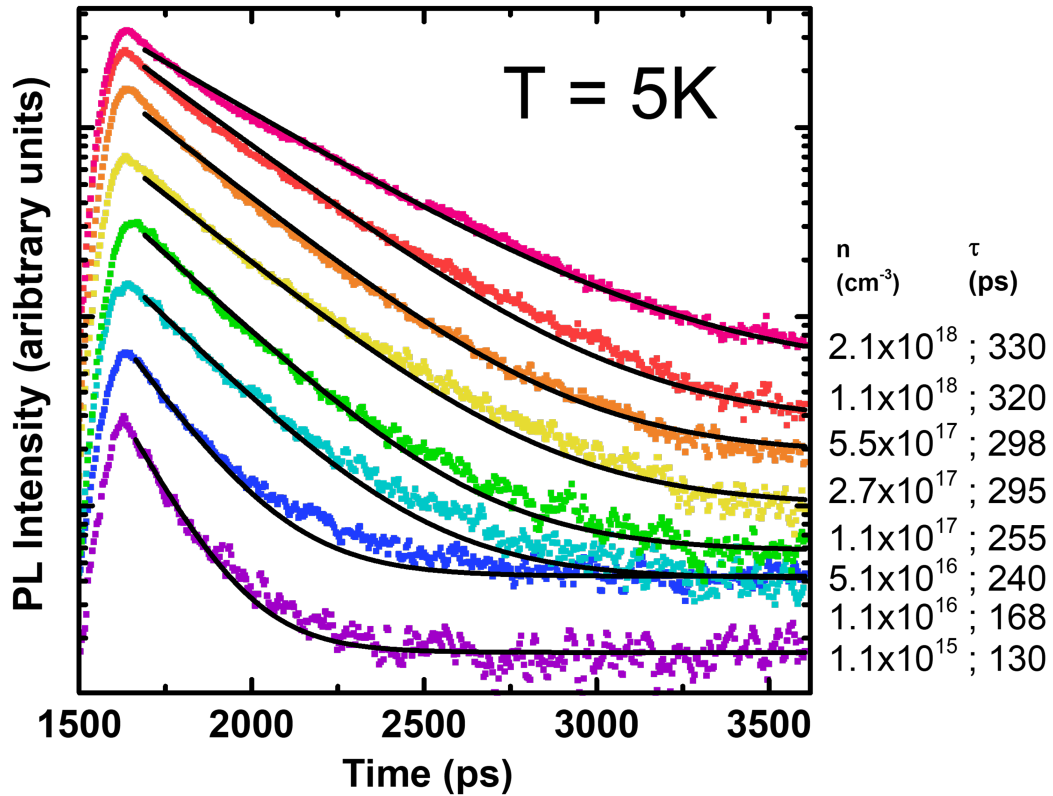


Figure III.7 – Mono-exponential ($y = y_0 + Ae^{-\frac{t}{\tau}}$) PL decay fit at $T = 5K$

n_{TRPL} is identified with the carrier density n in equation III.4 and will be associated to the lifetime τ deduced from the fitting of the PL decay with a single exponential function. By combining equation III.4 with the experimental determination of $n(\tau)$ through the analysis of the TRPL data, it is

possible to extract the carrier density as a function of excitation intensity I in the μ -PL experiments. A graphical approach displayed in figure III.8 is proposed to evaluate n as a function of I , where the experimental data $n_{\text{TRPL}}(\tau) = n(\tau)$ are reported on the figure together with the evolution $n(\tau)$ for various excitation intensities I , as given by equation (III.4).

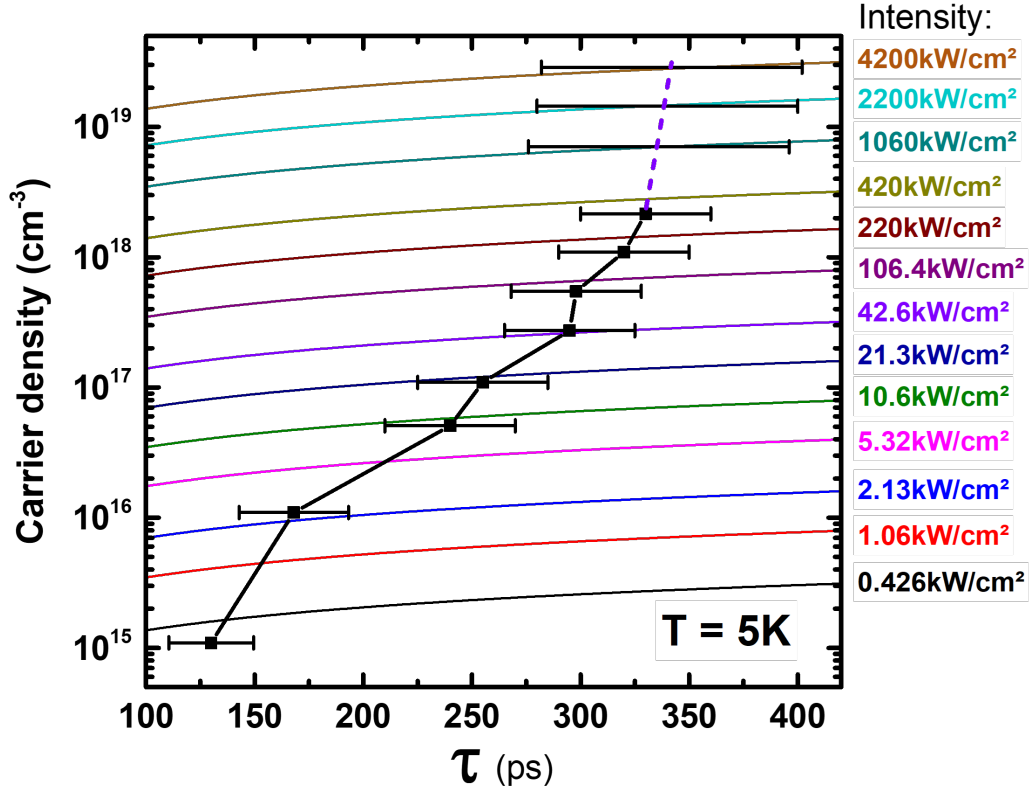


Figure III.8 – Experimental measurements of the carrier lifetime τ are reported as a function of carrier density n at 5K. The use of equation III.4 allows to calculate $n(\tau)$ for various excitation intensities. Intersection of these curves with the set of experimental data provides a correspondence between the carrier density and the excitation intensity. Lifetimes extracted by applying mono-exponential fits to the time-resolved spectra of freestanding GaN at $T = 5K$.

Figure III.8 summarizes the results obtained thanks to the data analysis: τ corresponds to the decay time extracted by fitting the PL decay with a single exponential function, as shown in figure III.7. It is important to note that in the Figure III.8, the carrier density displays a continuous dependence on carrier lifetime. It was not possible to measure the lifetime constant τ through TRPL experiments for high carrier densities owing to the limitation of the available excitation intensity (I_{TRPL}). Consequently, the three last τ values have been extrapolated as shown on figure III.8.

III.3.5 Study of the redshift as a function of the carrier density

The red-shift of the D^0X line is a criterion which has been used previously by Binet et al. to identify the Mott transition in GaN [111]. To do so the energy of D^0X needs to be tracked as a function of the injected carrier density, which has to be precisely evaluated and has been detailed in the previous part. The carrier density corresponds to the total electron density and, thus, includes all species (i.e., electrons, donor and acceptor-bound excitons as well as free-excitons). It is important to note that our experiments have been carried out with a bulk GaN sample and the luminescence signal comes mainly from the surface of the sample where the carrier density is the highest but, the distribution of carriers throughout the sample is not homogeneous.

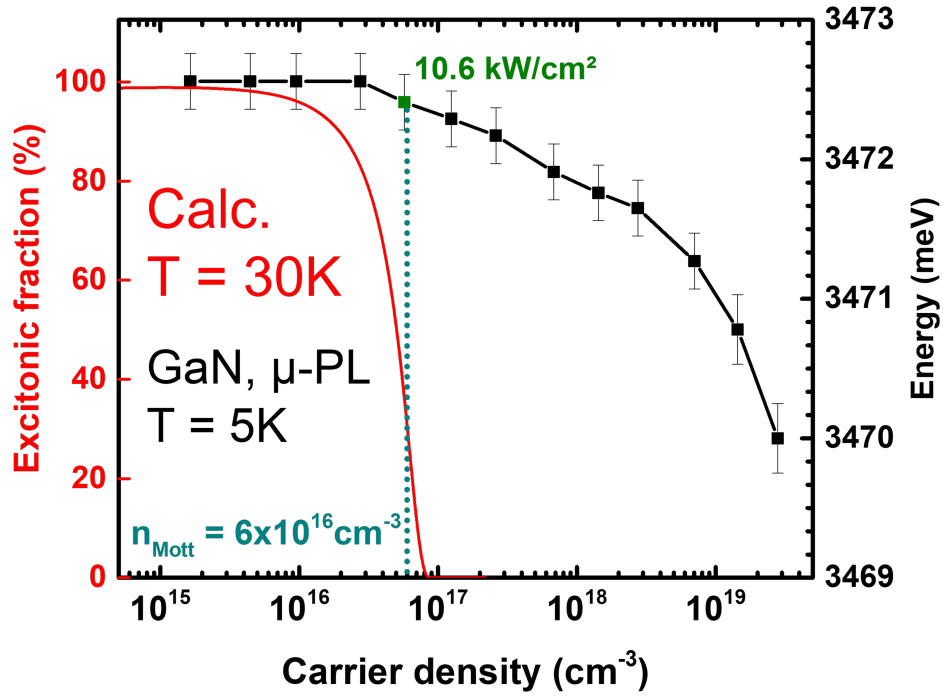


Figure III.9 – The energy of D^0X is plotted as a function of the carrier concentration injected by optical excitation. The red-shift of this transition from 10.6 kW/cm^2 indicates the occurrence of the bandgap renormalization and coincides with the drop of the excitonic fraction. Those phenomenon implies that the Mott transition is occurring which corresponds to a carrier density of $6 \times 10^{16} \text{ cm}^{-3}$. The Mott transition is not abrupt and is included in the $3 \times 10^{16} \text{ cm}^{-3}$ - $9 \times 10^{16} \text{ cm}^{-3}$ range. The calculation of the excitonic fraction for a temperature of 30K is found in good agreement with the experimental observation.

The redshift of the D^0X line as a function of the carrier density n is then reported in Figure III.9. This red-shift, which evidences the bandgap renormalization [130], is observed from a carrier concentration of $6 \times 10^{16} \text{ cm}^{-3}$. Calculations of the excitonic fraction with respect to the whole amount of injected carriers are carried out within the model proposed by Versteegh et al. [68]. The results are reported in figure III.9 for a temperature of 30 K, which corresponds roughly to the measured

electronic temperature. The theoretical Mott transition is evaluated to be about $8\text{--}9 \times 10^{16} \text{ cm}^{-3}$, in good agreement with the experimental observations. As shown by the theoretical curve, this transition is not abrupt since it occurs between $3 \times 10^{16} \text{ cm}^{-3}$ and $9 \times 10^{16} \text{ cm}^{-3}$. The corresponding carrier lifetime as shown in figure III.8 is about 242 ps around the Mott transition.

III.3.6 Bandgap renormalization

The bandgap renormalization is a consequence of the Mott transition and it has been shown that it can be seen through the redshift. The consideration of the bandgap renormalization is needed to explain several effects seen during our μ -PL experiments and will now be detailed.

The different studies cited (Haug [130], Klingshirn [49], Binet [111]) specify that the Mott transition takes place between free excitons and free electron-hole pairs. The parameters of free excitons are used to describe the transition. At low temperature the main emission peak corresponds to D^0X . In our case and like the work of Binet, we follow the evolution of this peak as a function of the excitation density to highlight a redshift occurring beyond the Mott transition. When the carrier density is increased, the gap is reduced: this phenomenon corresponds to the bandgap renormalization [49]. Even if the bandgap energy shifts with increasing carrier density, the energy of the excitons does not change as it has been shown both experimentally and theoretically [8, 49]. Thus, when the carrier density increases, the energy of the gap decreases, the excitonic oscillator strength decreases as well until the energy of the gap falls below that of the excitons. This change is observed experimentally by the redshift as seen on figure III.9.

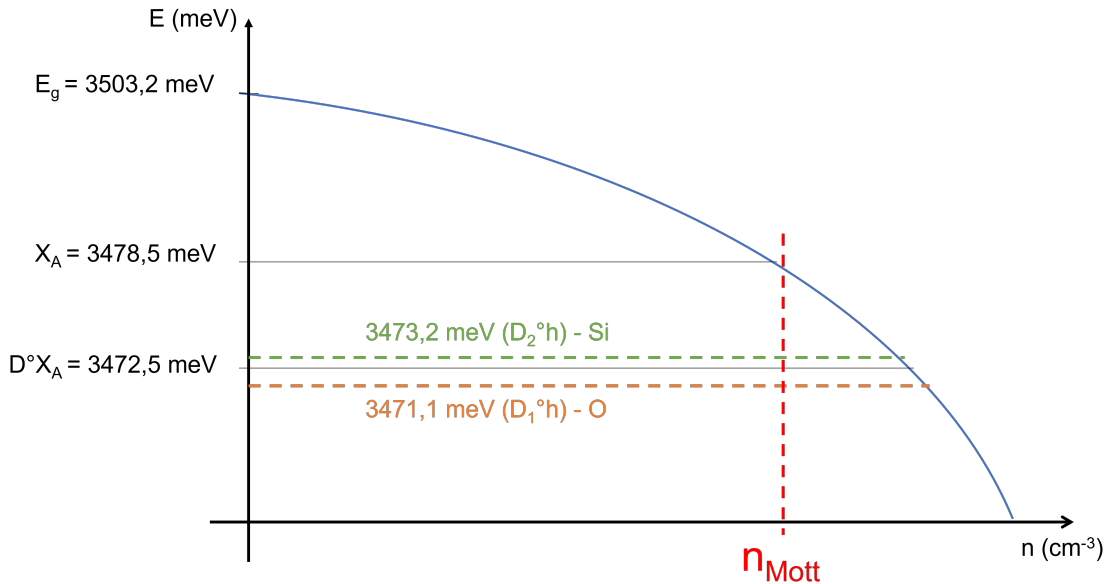


Figure III.10 – Bandgap renormalization in function of carrier density n .

Experimentally, we observe a redshift when the free exciton signature is lost. Before the beginning of the redshift, the measured luminescence of this peak is attributed to the optical transition

of an exciton bound to a neutral donor (D^0X). This excitonic complex consists of an exciton (e^- , h^+) localized on a neutral donor (D^+ , e^-) and has an emission energy different from that of the free excitons A and B.

We follow the evolution of this peak as a function of the excitation density in order to highlight a redshift beyond the Mott transition, (materialized with the red dotted line on figure III.10) due to the gap renormalization: this approach is based on the hypothesis verified experimentally and theoretically [107] for bulk semiconductors according to which the reduction of the binding energy of the free excitons is entirely compensated by the gap renormalization up to the Mott density. To be more precise, reflectivity and photoluminescence measurements on this sample shown earlier on figure III.1 highlights the presence of two excitonic D^0X complexes S_1 and S_2 associated to oxygen and silicon with binding energies of respectively 32.1meV and 30meV [114]. The S_2 peak, at high energy is more intense which suggests that the Si-bound donor concentration is greater than the O-bound one. With the increase in power density, the carrier density at the surface of the sample increases: experimentally a first redshift of 0.7meV is observed on figure III.9 and could correspond to the transition from D^0X to D^0h . Then the shift is associated with the renormalization of the gap. Moreover, in the sample, the inhomogeneous distribution of carriers in the layer allowing the emission of D^0X complexes located deeper even beyond the Mott density, and would limit the redshift explaining the small energy variation at carrier density lower than $3 \times 10^{17} \text{ cm}^{-3}$ as seen on figure III.9.

III.3.7 Versteegh model and excitonic fraction determination

Figure III.11 reports the theoretical evolution of the Mott density (n_{Mott}) calculated from the Versteegh model [68] for various temperatures in the case of GaN and ZnO. To compute n_{Mott} and to compare the theoretical value with our experimental results, we use the approach developed by Versteegh et al. [68], which considers the screening of the excitonic Coulomb interaction through the Yukawa potential [131] characterized by the screening length, λ_s within the approximation of a static screening. This approximation has been verified in the case of GaN. The Mott density corresponds to the density at which λ_s is decreased to the exciton Bohr radius a_0 . λ_s is derived using numerical calculation from the chemical potentials of electrons and holes as function of the carrier density n in the ideal gas approximation.

More precisely, the screening of the Coulomb interaction is described through the Yukawa potential:

$$V(\vec{r}_e - \vec{r}_h) = \frac{e^2}{4\pi\epsilon_0\epsilon_r \|\vec{r}_e - \vec{r}_h\|} e^{-\|\vec{r}_e - \vec{r}_h\|/\lambda_s} \quad (\text{III.5})$$

The latter is characterized by the screening length, λ_s , within the approximation of a static screening, which can be justified by the fact that the Fermi energies $(E_{F,i} = \frac{\hbar^2}{2m_i} (3\pi^2 n)^{2/3})$ are smaller than \hbar times the plasma frequency $\omega_p = \sqrt{\frac{e^2 n}{\epsilon_0 \epsilon_r m_r}}$, where m_r is the reduced mass of the electron-hole pair.

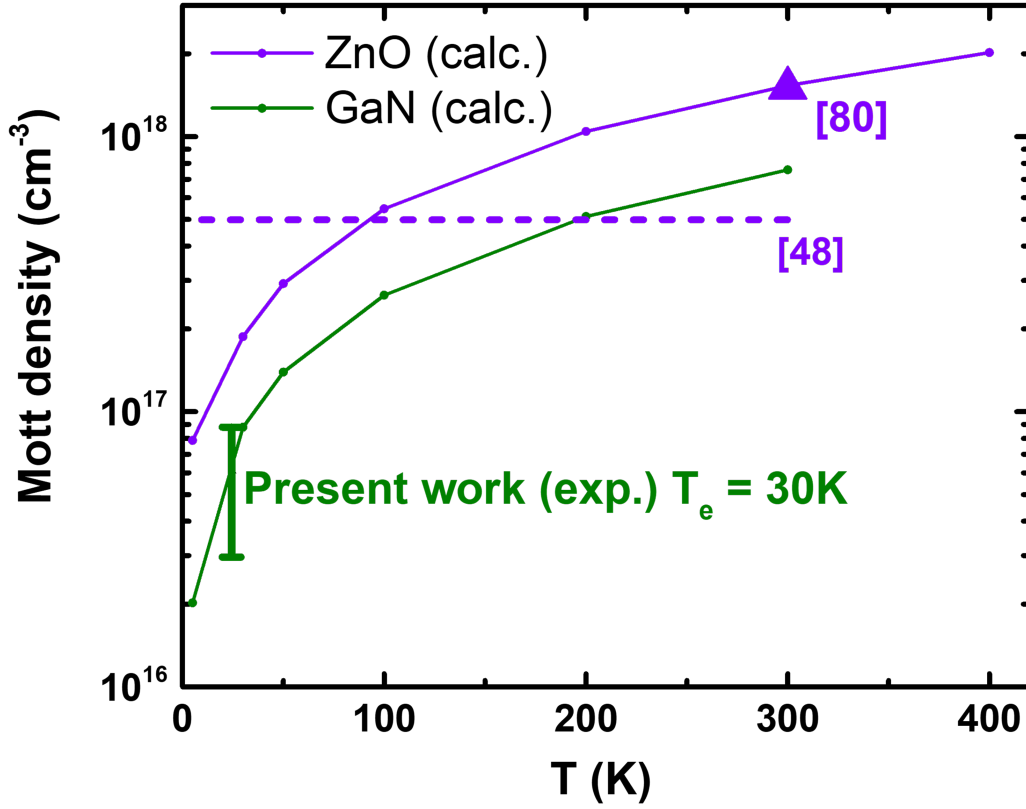


Figure III.11 – Theoretical and experimental values of the carrier density n_{Mott} at the excitonic Mott transition. The excitonic Mott transition are reported in the case of GaN and ZnO for comparison from Klingshirn estimation [49] and from the Versteegh's model [68]. n_{Mott} in GaN is necessarily lower than the one of ZnO owing to the difference of the excitonic binding energies of these materials (25 meV for GaN versus 60 meV for ZnO). Our experimental values for GaN are in good agreement with the calculations given by the model of Versteegh et al. [68].

The Mott density n_M corresponds to the density at which λ_s equals the exciton Bohr radius a_0 . λ_s is derived using numerical calculation of the chemical potentials as function of the carrier density n in the ideal gas approximation:

$$\lambda_{s,e} = \sqrt{\frac{\varepsilon_0 \varepsilon_r}{e^2} \frac{\partial \mu_e}{\partial n}}, \text{ for electrons} \quad (\text{III.6})$$

and $\lambda_s^{-1} = \lambda_{s,e}^{-1} + \lambda_{s,h}^{-1}$. The ideal-gas chemical potential (μ_e, μ_h) is numerically calculated from:

$$p = n = \frac{1}{2\pi^2} \left(\frac{2m_i}{\hbar^2} \right)^{2/3} \int_0^\infty \frac{\sqrt{\varepsilon}}{1 + \exp\left(\frac{\varepsilon - \mu_i}{kT}\right)} d\varepsilon \quad (\text{III.7})$$

with $i = e$ or h . The electron chemical potential μ_e is measured from the conduction-band edge and the hole chemical potential μ_h is measured from the valence-band edge.

Note that the ideal gas approximation slightly overestimates the screening due to the weaker screening by excitons than by unbound carriers. In a self-consistent approach, this calculation can be refined by computing the excitonic fraction n_{exc}/n , which represents the fraction of carriers that are bound into excitons with respect to the total carrier density n :

$$n = n_{\text{exc}} + \frac{1}{2\pi^2} \left(\frac{2m_i}{\hbar^2} \right)^{2/3} \int_0^\infty \frac{\sqrt{\varepsilon}}{1 + \exp\left(\frac{\varepsilon - \mu_i}{kT}\right)} d\varepsilon \quad (\text{III.8})$$

$$n_{\text{exc}} = \frac{1}{\pi^2} \left(\frac{2(m_e + m_h)}{\hbar^2} \right)^{2/3} \int_{-E_s}^0 \sqrt{\varepsilon + E_s} \times f_{\text{exc}}(\varepsilon) d\varepsilon \quad (\text{III.9})$$

with f_{exc} given by Bose-Einstein statistic: $f_{\text{exc}}(\varepsilon) = \frac{1}{\exp\left(\frac{\varepsilon - \mu}{kT}\right) - 1}$ and E_s , the ground-state exciton binding energy. It only slightly overestimates the screening due to a weaker screening by excitons than by unbound carriers. In a self-coherent approach the calculation can be refined by computing the excitonic fraction $\frac{n_{\text{exc}}}{n}$, which represents the fraction of carriers bound together to form excitons with respect to the total carrier density.

The experimental determinations of n_{Mott} reported in previous works are indicated on figure III.11 in the case of ZnO ($5 \times 10^{17} \text{cm}^{-3}$ temperature-independent [49], $1.5 \times 10^{18} \text{cm}^{-3}$, $T = 300\text{K}$ [68]). If a scaling law is assumed between GaN and ZnO, it can be concluded that the n_{Mott} value for GaN is necessarily lower than that for ZnO. It is reminded here that the excitonic binding energy of ZnO is a factor 2.4 larger than that of GaN. The experimental value of the Mott density deduced from the present study is found to be in good agreement with the calculation for a temperature of 30 K.

III.3.8 Temperature influence on Mott transition

Through similar process than previously introduced, it is possible to correlate the measured lifetime with different temperatures and the associated microphotoluminescence power study. Figure III.12 is built exactly in the same way of the figure III.8 with added temperature from 20K to 300K. All the measured lifetimes featured two time contributions, a short one τ_1 and a long one τ_2 . The decay time are fitted with a bi-exponential fit using the following equation:

$$y(\tau) = y_0 + A_1 e^{-t/\tau_1} + A_2 e^{-t/\tau_2} \quad (\text{III.10})$$

In order to exploit the results, it was chosen to weight the contributions of the short and long times giving an average decay time as a function of the excitation density and temperature. The average time was obtained by linear combination of the bi-exponential terms such as:

$$\frac{1}{\tau} = \frac{A_1}{A_1 + A_2} \frac{1}{\tau_1} + \frac{A_2}{A_1 + A_2} \frac{1}{\tau_2} \quad (\text{III.11})$$

This allows us to get an average lifetime weighted by the coefficients A_1 and A_2 of each of the time contributions. With increasing temperature, the lifetime decreases from 150 ps to 50ps in average.

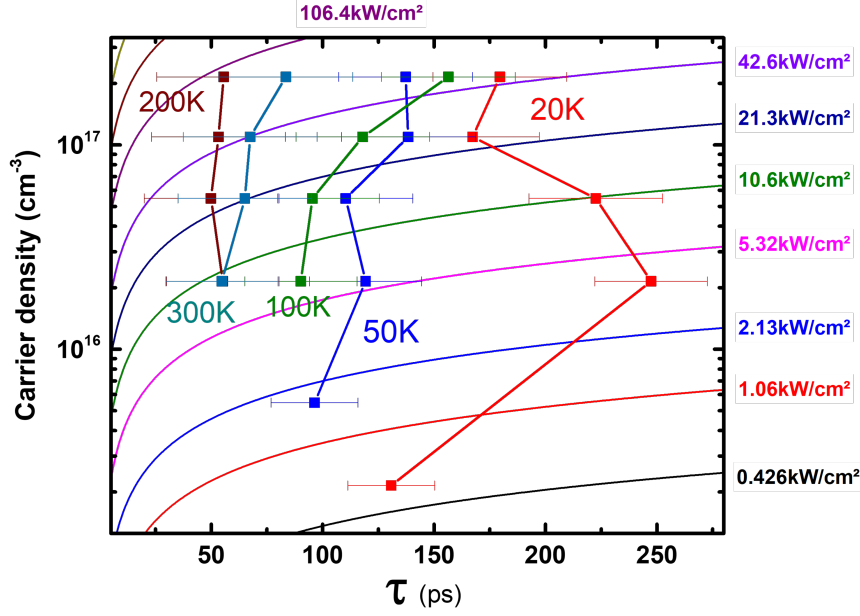


Figure III.12 – Experimental measurements of the carrier lifetime τ are reported as a function of carrier density n for varying temperatures ranging from 20K to 300K. The use of equation III.4 allows to calculate $n(\tau)$ for various excitation intensities. Intersection of these curves with the set of experimental data provides a correspondence between the carrier density and the excitation intensity.

The two μ -PL graphs shows the intensity results with increasing power density for 20K and 100K. We can see that the optical recombination at the excitonic energies are not the same between those two temperatures. The excitation intensity at which it is not possible to distinguish the excitonic transition has been highlighted (13 kW/cm² for the 20K and 5,8 kW/cm² for 100K). It is harder to visually estimate the Mott density after 125K from the μ -PL power study as thermal activation induced broadening conceal the excitonic optical transitions.

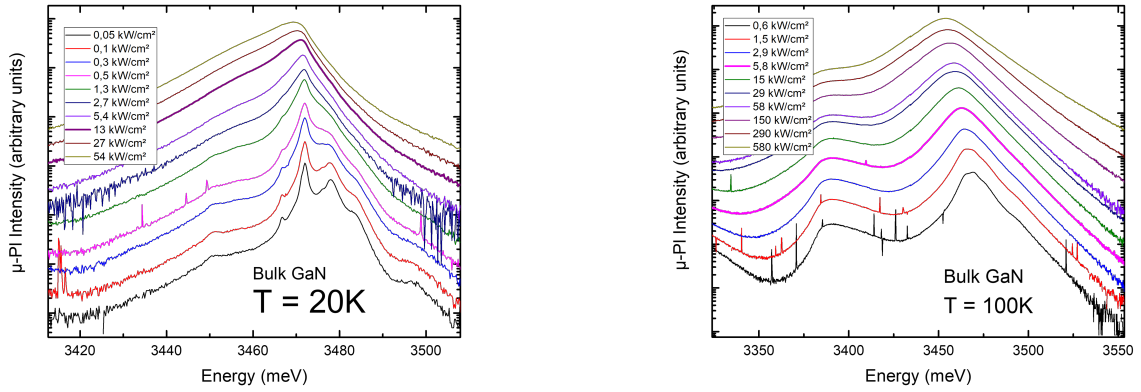
We can see in table III.3 that the Mott density is progressively decreasing with the increase of the temperature. This result can be explained such as the neutral donor bound excitons are ionized with the thermal activation energy and will progressively contribute to the screening of free excitons.

Temperature (K)	5	20	50	100	125	150
$n_{\text{Mott}} (\times 10^{16} \text{ cm}^{-3})$	(6 ± 3)	(6 ± 3)	(6 ± 3)	(2 ± 3)	(1 ± 3)	(1 ± 3)

Table III.3 – Experimental values of n_{Mott} in function of temperature.

III.4 Results discussion

The Mott density determined in this work is more than one order of magnitude smaller than previous measurements and it is worth analyzing the possible origins of this discrepancy.



(a) μ -PL spectra at 20K under quasi continuous excitation (Qswitched pulsed excitation laser at 266 nm). Excitons transitions are no more distinguishable after 13 kW/cm² excitation intensity.

(b) μ -PL spectra at 100K under quasi continuous excitation (Qswitched pulsed excitation laser at 266 nm). Excitons transitions are no more distinguishable after 5,8 kW/cm² excitation intensity.

Figure III.13 – μ -PL spectra at different temperatures under quasi continuous excitation (Qswitched pulsed excitation laser at 266 nm).

III.4.1 Inhomogeneities of the carrier distribution

Before comparing our results with those published in the literature, it is important to discuss physical considerations related to our sample regarding the evolution of the carrier density.

As our sample is a bulk, the experimental observations are mainly from its surface where the carrier density is at the highest but the distribution of carriers across the sample decreases continuously from the surface. At low temperature the main emission peak corresponds to D^0X . Fisher's work reports another detailed analysis of the screening of excitons in a GaN slab through femtoscond pump-probe absorption [110]. Absorption spectra are measured at 5K for various excitations intensities. The authors underline in this paper that the absorption of the pump is not homogeneous since the GaN thickness is equal to 0.38 μ m while the absorption length at the laser energy is considered equal to 0.11 μ m.

Consequently, the Mott density can be reached at the illuminated front face of the sample while excitons remain present at the back side. Our sample also behaves as a semi-infinite system in which the distribution of carriers is necessarily inhomogeneous and, as discussed already, in a quasi-stationary regime it is possible to determine the distribution of carriers (electrons, n) as a function of the depth x of the sample. This distribution can be written, neglecting in-plane carrier diffusion and without considering surface recombination, as:

$$n(x) = \frac{\phi\alpha\tau}{1 - \alpha^2 L^2} (e^{-\alpha x} - \alpha L e^{-x/L}) \quad (\text{III.12})$$

with $L = \sqrt{D\tau}$. Compared to our PL experiments, in this experimental configuration (pump-probe absorption) it is very difficult to estimate reliable carrier densities as both the inhomogeneous spread-

ing of carriers and the variable screening of excitons along the sample have to be considered, which requires time- and spatial-dependent simulations. Indeed, Fisher et al. reported a Mott density of $1 \times 10^{18} \text{ cm}^{-3}$ without indicating precisely the way they followed to estimate it. The evolution of the carrier density is directly influenced by the inhomogeneity of their distribution in the bulk. Moreover, the hypothesis of the preponderance of the monomolecular recombination regime still has to be precisely quantized for all power densities. From the experimental results obtained, we now seek to determine more precisely the effect of the diffusion of the carriers, in depth in the bulk.

III.4.2 Carrier distribution in the presence of a bi-molecular recombination term

According to Pelant and Valenta [100], the monomolecular recombination process is attributed to the de-excitation to the ground state of the excited localized centers. Also, the bimolecular recombination process is attributed to the recombination of electrons and holes. To evaluate the influence of the bi-molecular recombination term means to solve the differential equation about the time dependence of the evolution of the carrier density, described by the following equation:

$$\frac{dn(t)}{dt} = G - \frac{n}{\tau_r} - \frac{n}{\tau_{nr}} - \beta_r n^2 - \beta_{nr} n^2 \quad (\text{III.13})$$

with G the generation term, τ_r and τ_{nr} respectively the radiative and non radiative recombination times, and β_r, β_{nr} the radiative and non radiative bimolecular recombination coefficients [100].

It is possible to solve the carrier distribution equation numerically. The physical reasoning will be detailed from the continuity equation and present the typical solution of differential equation including the diffusion and bimolecular term. Finally, the adaptation of the equation to the numerical solution deduced from the previous reasoning will be introduced.

III.4.2.1 Solution by the numerical method

Through photoexcitation, the generation of excited carriers in excess will diffuse and recombine. The evolution out of equilibrium is governed by the equation of continuity; the rate of generation of carriers is given by:

$$g(x)_n = g(x)_p = \phi_t \alpha e^{-\alpha x} \quad (\text{III.14})$$

ϕ_t , being the photon flux and α , the absorption coefficient. The evolution of the carrier density taking into account only the monomolecular recombination is written [129]:

$$\frac{\partial n}{\partial t} = n \mu_n \frac{\partial E}{\partial x} + \mu_n E \frac{\partial n}{\partial x} + D_n \frac{\partial^2 n}{\partial x^2} + \phi_t \alpha e^{-\alpha x} - \frac{n - n_0}{\tau_n} \quad (\text{III.15})$$

$$\frac{\partial p}{\partial t} = -p\mu_p \frac{\partial E}{\partial x} - \mu_p E \frac{\partial p}{\partial x} + D_p \frac{\partial^2 n}{\partial x^2} + \phi_t \alpha e^{-\alpha x} - \frac{p - p_0}{\tau_p} \quad (\text{III.16})$$

With E the component of the electric field in the x direction, representing the sum of two contributions $E = E_i + E_a$.

E_a is the applied field to the sample by a possible bias voltage and E_i is the internal field resulting from the difference in mobility between electrons and holes.

During the photoexcitation, the electrical neutrality of the semiconductor is preserved and thus results in the following approximation $\Delta n(x, t) \approx \Delta p(x, t)$. The electrons and the holes created in excess by the photoexcitation diffuse together in the so-called ambipolar diffusion process. In addition, the recombination rates of the electrons and holes are necessarily equal since carriers recombine in pairs and if $\Delta n = \Delta p$ then the lifetimes of the carriers are equal $\tau_n = \tau_p = \tau$. Thus one can describe the determination of the carriers by their initial density and according to their evolution we have $n = n_0 + \Delta n$ and $p = p_0 + \Delta p$. The applied electric field E_a is constant so $\frac{dE_a}{dx} = 0$.

From these conditions, we rewrite the continuity equations such that:

$$\frac{\partial \Delta n}{\partial t} = n\mu_n \frac{\partial E_i}{\partial x} + \mu_n (E_i + E_a) \frac{\partial \Delta n}{\partial x} + D_n \frac{\partial^2 \Delta n}{\partial x^2} + \phi_t \alpha e^{-\alpha x} - \frac{\Delta n}{\tau_n} \quad (\text{III.17})$$

$$\frac{\partial \Delta n}{\partial t} = -p\mu_p \frac{\partial E_i}{\partial x} - \mu_p (E_i + E_a) \frac{\partial \Delta n}{\partial x} + D_p \frac{\partial^2 \Delta n}{\partial x^2} + \phi_t \alpha e^{-\alpha x} - \frac{\Delta n}{\tau_n} \quad (\text{III.18})$$

It is shown that $\mu_n E_i \partial \Delta n / \partial x$ are negligible in front of the term $D_n \partial^2 \Delta n / \partial x^2$. By multiplying the first equation by $p\mu_p$, the second by $n\mu_n$ and by summing member by member, with $\mu_n E_i \frac{\partial \Delta n}{\partial x} \ll D_n \frac{\partial^2 \Delta n}{\partial x^2}$:

$$\frac{\partial \Delta n}{\partial t} = \mu_n^* E_a \frac{\partial \Delta n}{\partial x} + D^* \frac{\partial^2 \Delta n}{\partial x^2} + \phi_t \alpha e^{-\alpha x} \quad (\text{III.19})$$

μ_n^* being the ambipolar diffusion mobility such as $\frac{(p-n)\mu_n\mu_p}{p\mu_p - n\mu_n}$ et D^* , the ambipolar diffusion coefficient such as $\frac{(p+n)D_nD_p}{pD_p + nD_n}$. For the following development, the applied field will not be considered, and therefore $E_a = 0$.

In steady state $\frac{\partial n}{\partial t} = 0$ and with consideration of the bimolecular recombination term $-\beta n^2$, the ambipolar equation then becomes:

$$\phi_t \alpha e^{-\alpha x} - D \frac{d^2 n(x)}{dx^2} - \frac{n}{\tau} - \beta n^2(x) = 0 \quad (\text{III.20})$$

In the case where the bimolecular recombination term is negligible, the solution $n_s^0(x)$ meets the requirement where $x = 0$, $\frac{\partial n}{\partial x} = 0$. In order to effectively compare the results with and without the presence of the bimolecular recombination term, the same boundary conditions must be met as when $\beta \neq 0$. For x approaching infinity ($x \ll L$), the term $-\beta n^2$ can be neglected with respect to the term $-n/\tau$ and we finally find the steady state resolution already presented in equation III.4. The general solution of the equation III.20 will be written $n_s^0(x)$.

$$n_s^0(x) = \frac{\phi\alpha\tau}{1 - \alpha^2 L^2} \left(e^{-\alpha x} - \frac{s/D + \alpha}{s/D + 1/L} e^{-x/L} \right) \quad (\text{III.21})$$

with $L = \sqrt{D\tau} > 1/\alpha$ and $0 > 1 - \alpha^2 L^2$

$$n_s^0(x) = \frac{\phi\alpha\tau}{\alpha^2 L^2 - 1} \left(\frac{s/D + \alpha}{s/D + 1/L} e^{-x/L} - e^{-\alpha x} \right) \quad (\text{III.22})$$

with $A_\alpha = \frac{s/D + \alpha}{s/D + 1/L}$,

$$\begin{aligned} n_s^0(x) &= \frac{\phi\alpha\tau}{\alpha^2 L^2 - 1} (A_\alpha e^{-x/L} - e^{-\alpha x}) \\ n_s^0(x) &= \frac{\phi\alpha\tau}{\alpha^2 L^2 - 1} A_\alpha e^{-x/L} \left(1 - \frac{1}{A_\alpha} e^{-\alpha x} e^{x/L} \right) \\ n_s^0(x) &= \frac{\phi\alpha\tau}{\alpha^2 L^2 - 1} A_\alpha e^{-x/L} \left(1 - \frac{1}{A_\alpha} e^{-x(\alpha - 1/L)} \right) \end{aligned}$$

The term $A_\alpha e^{-x(\alpha - 1/L)}$ is a decreasing exponential, negligible for $x \rightarrow +\infty$ before 1.

$$n_s^0(x) \approx \frac{\phi\alpha\tau}{\alpha^2 L^2 - 1} A_\alpha e^{-x/L} \quad (\text{III.23})$$

in the case where $s = 0$, the expression becomes:

$$n_0^0(x) \approx \frac{\phi\alpha\tau}{\alpha^2 L^2 - 1} A_0 e^{-x/L} \quad (\text{III.24})$$

with $A_0 = \alpha L$ and

$$\frac{n_s^0(x)}{n_0^0(x)} = \frac{A_\alpha}{A_0} \quad (\text{III.25})$$

Finally,

$$n_s^0(x) = \frac{A_\alpha}{A_0} n_0^0(x) = K_s n_0^0(x) \quad (\text{III.26})$$

The solution of the global equation including the bimolecular recombination term for large depths is proportional by a factor K_s to the analytical solution $n_0^0(x)$. The proportionality coefficient K_s will define a boundary condition at $x = 0$ which will only be known a posteriori.

Now that the determination of boundary limits has been demonstrating, we want to adapt the general solution of the equation, including the bimolecular recombination term in order to include it in the numerical resolution. First, the equation is transformed by simple approximation with a Taylor series, into a numerical sequence with recurrence which allows from the values X_k and X_{k+1} to calculate X_{k+2} . Then, the initialization of our numerical resolution is possible from the fact that the bimolecular recombination term becomes negligible at large depths in the bulk. The calculation is therefore done in reverse, by an initialization from a deep point from the analytical solution calculated for $\beta = 0$ and then going back to the point at $x = 0$ corresponding to the surface of the sample. The initialization equation is in the following form:

$$\phi_t \alpha e^{-\alpha x} + D \frac{d^2 n(x)}{dx^2} - \frac{n}{\tau} - \beta n^2(x) = 0 \quad (\text{III.27})$$

by dividing on D we obtain:

$$\frac{\phi_t \alpha e^{-\alpha x}}{D} + \frac{d^2 n(x)}{dx^2} - \frac{n(x)}{D\tau} - \frac{\beta}{D} n^2(x) = 0 \quad (\text{III.28})$$

As we have seen earlier in the demonstration, in the absence of the bimolecular recombination process the equation reduces to the ambipolar diffusion equation whose analytical solution is already known with $s = 0$. For simplification reasons, let $a = \frac{1}{D\tau}$, $b = \frac{\beta}{D}$ and $g(x) = -\frac{\phi_t \alpha e^{-\alpha x}}{D}$.

Equation III.28 then becomes:

$$\frac{d^2 n(x)}{dx^2} - an(x) - bn^2(x) = g(x) \quad (\text{III.29})$$

From Taylor series, we have the following approximation:

$$\frac{d^2 n(x)}{dx^2} \approx \frac{n(x_{k+2}) - 2n(x_{k+1}) + n(x_k)}{\Delta^2} \quad (\text{III.30})$$

with k going from 1 to $N + 1$, $x_k = (k - 1)\Delta$ the discretization step and $N\Delta$ the depth of the sample. In the following, we will assume $n(x_k) = X_k$ to simplify the writing. After introducing the approximation, the equation finally becomes :

$$\left[\frac{X_{k+2}}{\Delta^2} + \frac{X_{k+1}}{\Delta^2} - \left(\frac{2}{\Delta^2} + a + bX_{k+1} \right) X_{k+1} \right] = f((K - 1)\Delta) \quad (\text{III.31})$$

The figure III.14 shows schematically how the numerical resolution works. The surface of the sample is positioned at $x = 0$ and is of $x + N + 1$ depth. Numerically, the thickness of the sample is similar to an interval from 1 to $N + 1$ divisible in k sections. It has been shown above that the numerical resolution is based on the analytical resolution in depth when the bimolecular recombination term is zero, so it is necessary to reverse the direction of resolution of the equation from the depth of the sample toward the surface. Thus we have the surface of the sample at the $N + 1$ point and the depth of the bulk starting at point 1 separated in J sections. By the following development, the equation becomes:

$$\left[\frac{X_{j-2}}{\Delta^2} + \frac{X_j}{\Delta^2} - \left(\frac{2}{\Delta^2} + a + bX_{j-1} \right) X_{j-1} \right] = f((N + 1 - j)\Delta) \quad (\text{III.32})$$

we can then isolate the term X_j :

$$X_j = \Delta^2 f((N + 1 - j)\Delta) - X_{j-2} + (2 + \Delta^2(a + bX_{j-1})) X_{j-1} \quad (\text{III.33})$$

The numerical solution starts from the term X_3 initialized from X_2 and X_1 values, analytical solutions for $n(x)_{\beta=0}$, coming from equation III.26, giving the values $X_1 = n(N\Delta)_{\beta=0}$ and $X_2 =$

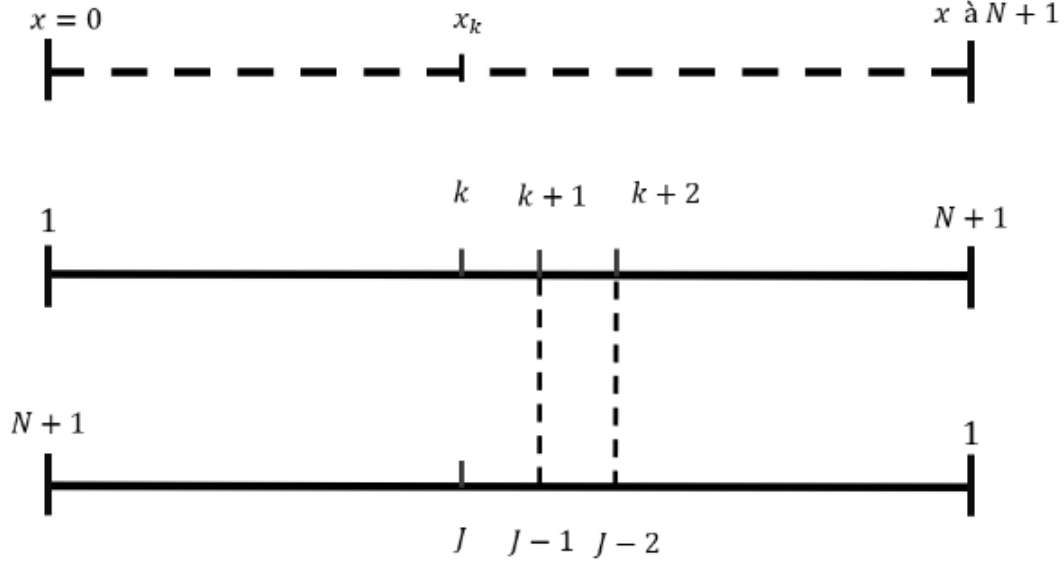


Figure III.14 – Diagram showing the inversion of the points from the depth of the sample $N + 1$ to the surface 1. This procedure is necessary for the numerical solution of the equation with diffusion and taking into account the bimolecular recombination term

$n((N - 1)\Delta)_{\beta=0}$. From this initialization, the numerical solution must respect the boundary condition of the zero derivative at $x = 0$ and is determined thanks to a corrective term named K_s introduced to the equation III.26.

III.4.2.2 Results

We verify on the figure III.15 that the results generated by the numerical calculation are coherent by calculating the general equation without the bimolecular recombination term. The values of carrier densities obtained analytically and numerically are equal and we see graphically that the two drawn curves drawn are equivalent. The calculated values at the surface of the sample are close to a relative precision of 10^{-8} from each other and are therefore consistent with the expected behavior.

Figure III.16 presents the result of the numerical calculation, i.e. the evolution of the carrier density as a function of the depth in the sample. The analytical solution without bimolecular recombination term and the numerical solution with bimolecular recombination term are compared. The variable parameters are the power density, the lifetime, the total thickness of the layer (the number of calculated points multiplied by the chosen step). The coefficient K_s from equation III.26 is the parameter to be varied to obtain in the case of the bimolecular recombination term, a surface recombination equal to 0. The boundary conditions are respected, with an initialization at far depth and the zero derivative at the surface of the sample. We see on the figure III.16 the influence of the bimolecular recombination term at the surface of the sample, where the carrier concentration is $5.917 \times 10^{15} \text{ cm}^{-3}$ while that of the analytical solution is $5.935 \times 10^{15} \text{ cm}^{-3}$ for 1.06 kW/cm^2 power density and

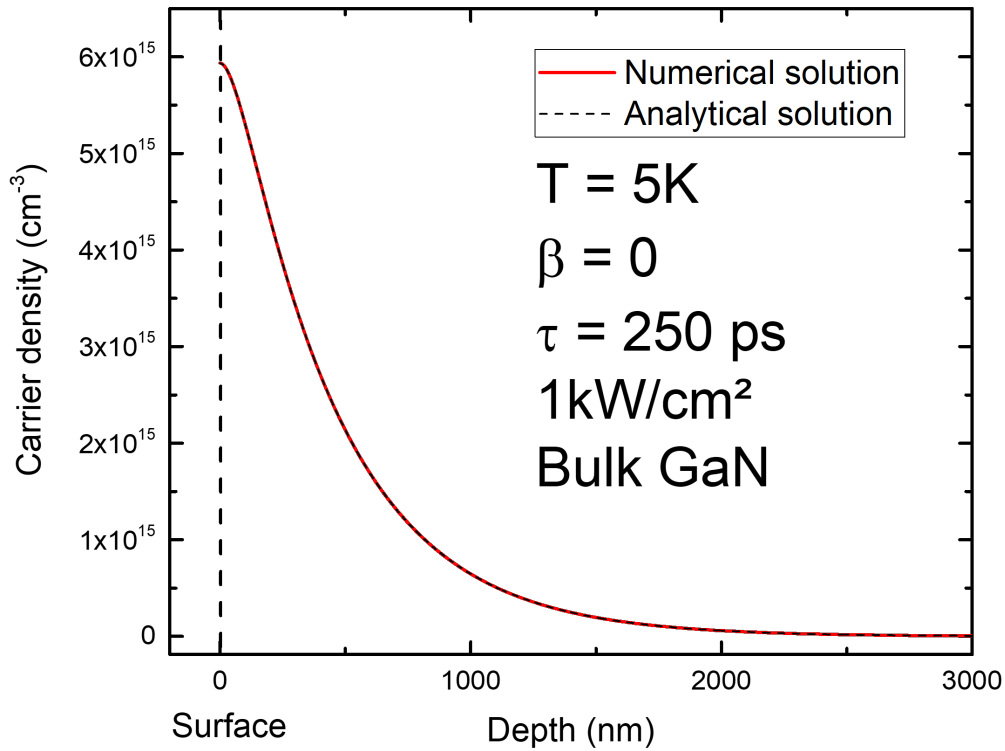


Figure III.15 – Numerical and analytical solutions for the general equation, the bimolecular recombination coefficient is set to 0 as a way to verify the consistency of the result. For this graph: $D = 7\text{cm}^2/\text{s}$, $\tau = 250\text{ps}$

β of $1.3 \times 10^{-8} \text{ cm}^{-3}$.

It is interesting to note that the influence of the recombination term is quite limited for low carrier densities, as explained in the discussion of results published by Binet et al. [111] in the section III.4.1. With the increase of the carrier density and past the Mott transition, an electron-hole plasma is favored to excitons. Concretely, although the screening of excitons and the Mott transition is passed on the surface, there is coexistence between electron-hole plasma and excitons in depth in the bulk resulting in simultaneous monomolecular and bimolecular recombination processes. From then on, we understand that with the increase of the power density and thus the increase of the carrier concentration, the electron-hole plasma progressively replaces the exciton recombination, justifying the preponderance of the bimolecular recombination term. From these results, it will now be interesting to estimate more precisely the influence of the bimolecular recombination term by comparing the results previously obtained by steady state analytical resolution presented earlier in this chapter with those that can now be calculated by taking into account the scattering and the bimolecular recombination term.

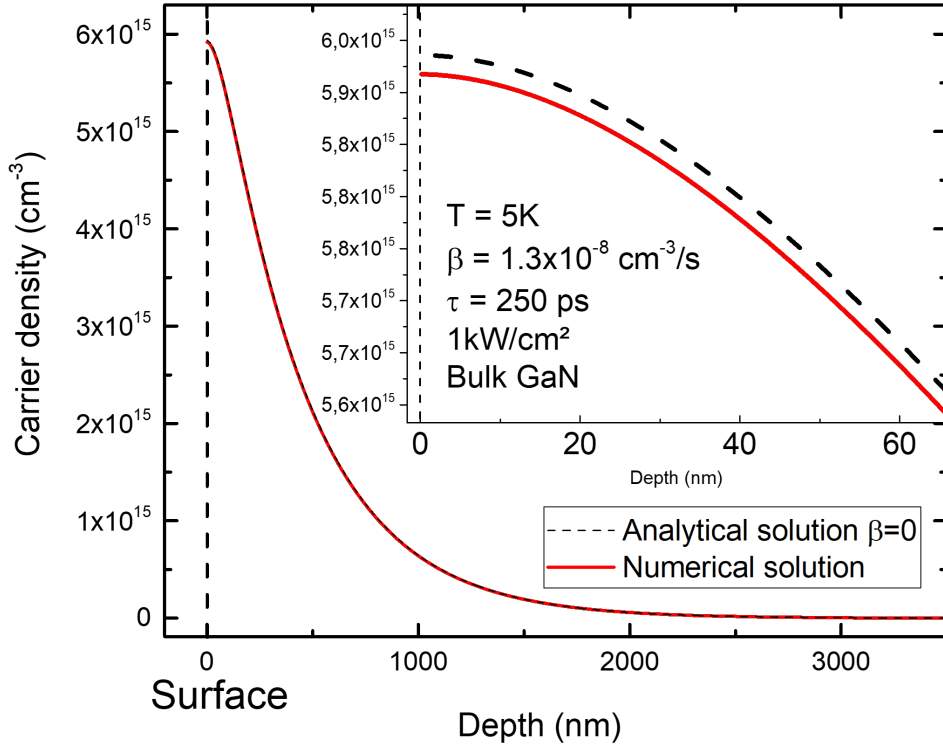


Figure III.16 – Differences between monomolecular analytical result and bimolecular numerical result. For this graph: $D = 7\text{cm}^2/\text{s}$, $\tau = 250\text{ps}$

III.4.3 Influence of the bi-molecular recombination term

III.4.3.1 Context

Binet et al. [111] have carefully analyzed the Mott transition in a bulk GaN sample through PL experiments as a function of power and temperature, under measurement conditions close to ours. The criterion which was used to detect the Mott transition is the red-shift of the emission line. At a bath temperature of 30 K they estimated a Mott density between 1.8 and $3.8 \times 10^{18} \text{ cm}^{-3}$, with an electronic temperature of 120 K.

Compared to ours, in Binet's work[111] the carrier density is evaluated by assuming only a bimolecular recombination, while the mono-molecular term associated to a certain carrier lifetime is not considered. The use of the bi-molecular term previously introduced in equation III.13, $-\beta n^2$ (with $\beta = \beta_r + \beta_{nr} = 1.3 \times 10^{-8} \text{ cm}^3/\text{s}$, n is the carrier density) instead of the mono-molecular one, $-n/\tau$, overestimates for short lifetimes, the evaluation of the carrier density n from the measurement of the excitation intensity [100]. Besides, the high electronic temperature with respect to the bath temperature reported by the authors suggests a short carrier lifetime. The lower τ value is measured, the higher the excitation intensity must be to get high carrier density. As a result, there are more

photo-created carriers with kinetic energy to dissipate. This results in an increase of the electronic temperature. In this case, a high excitation intensity is needed to maintain a sufficiently high carrier concentration so as to detect the Mott transition. If we assumed only a monomolecular recombination, it is necessary to consider a lifetime of about 26 ps to match our theoretical estimation of $n_{Mott} = 4.0 \times 10^{17} \text{ cm}^{-3}$ for an electronic temperature of 123K with a 314 kW/cm^2 power excitation, as used in [111]. Interestingly, carrier lifetimes measured by TRPL in similar samples as those employed by Binet and coworkers displayed values in the order of 24 ps at these temperatures [132], consistent with our estimations. It is worth comparing the contributions of bi-molecular and mono-molecular recombinations in the present work at the Mott transition, for $n = 6 \times 10^{16} \text{ cm}^{-3}$. The monomolecular term is found to be larger than the bi-molecular one by a factor 5.1, thus showing that the bimolecular term can be neglected. Moreover, the determination of the carrier lifetime through TRPL experiments (assuming a monoexponential decay) accounts for the small contribution of the bi-molecular term, since the fitting procedure provides an effective recombination time corresponding to the measured carrier density.

III.4.3.2 Fit with the term bi-molecular recombination

TRPL campaigns are extensive in time and require many precautions both in the measurement and in the results processing. Chronologically, interrogation about the influence of the bimolecular term came early in the discussion but required a secondary campaign and new measurements to ensure a fully optimized experimental setup and to have more experimental points to work on. The second TRPL campaign was also performed on the sample H46-2 with the same experimental setup whose excitation line and spot were optimized. The diameter of the spot is thus better controlled and allows an even more accurate estimation of the power density, at the expense of the maximum power density. This campaign allows to measure again precisely the carrier lifetimes, this time with a fit including the bimolecular recombination term to be compared with the results presented in the chapter III.3.4.

The TRPL measurements were performed with increasing power densities and the carrier lifetimes evolution with mono and bi-molecular processes can be described by the following differential equation [100]:

$$dn/dt = -\beta n^2 - n/\tau \quad (\text{III.34})$$

The formula used to calculate the decay times is the solution of equation III.34 and is of the form :

$$n(t) = \frac{n(0)e^{-t/\tau}}{1 + n(0)\beta\tau(1 - e^{-t/\tau})} \quad (\text{III.35})$$

with $n(0)$ the initial carrier density.

We can see on figure III.17 that the quoted lifetimes are increasing with the increase of the power density with a maximum of 450 ps. In order to fully exploit the deduced carrier densities using mono and bimolecular fits, the carrier densities as a function of the deduced lifetimes are compared in figure III.18. In blue, the measurements obtained by monomolecular fit and in green the new deduced points

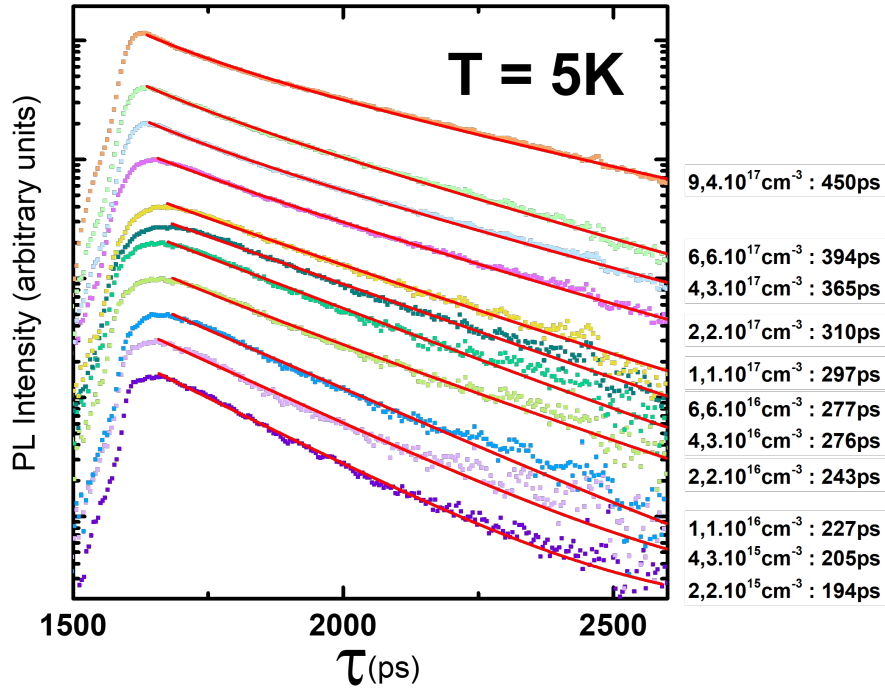


Figure III.17 – Bimolecular fit of measured decay time for several power densities.

including the bimolecular recombination term. The tendency is clearly visible on the figure III.18: at first the values are equivalent as the influence of the recombination term is very low, then with the increase of the power density the two curves separate progressively.

In order to fully characterize the influence of the bimolecular recombination term, it is also necessary to redefine the $n(\tau)$ lines calculated this time taking into account the diffusion and β . On the figure III.18, we distinguish in continuous line the $n(\tau)$ values previously used without β to which are added in dotted lines the new calculated values.

It appears that at low power densities, the differences are small confirming the previous conclusions, the bimolecular recombination term has little to no influence. On the other hand, for a power density of 106 kW/cm^2 , the carrier densities deduced from the simple case of monomolecular recombination overestimates the carrier density at a given τ time. the approximated solution for the monomolecular fit can be read on the full line and will give a carrier density higher than the result read with the dotted line corresponding to a bimolecular fit. For 106 kW/cm^2 the estimated carrier density for a monomolecular fit is around $5 \times 10^{17} \text{ cm}^{-3}$ and for the bimolecular fit, the result is around $3.5 \times 10^{17} \text{ cm}^{-3}$.

Part of the estimated results therefore relies on the value of the bimolecular recombination term and its estimation has not yet been discussed. We note that in the use of the equation III.35 it is possible to isolate the parameter β in the same way as the life time τ . This new "variable" parameter deduced during the fits would allow to determine experimentally the bimolecular recombination co-

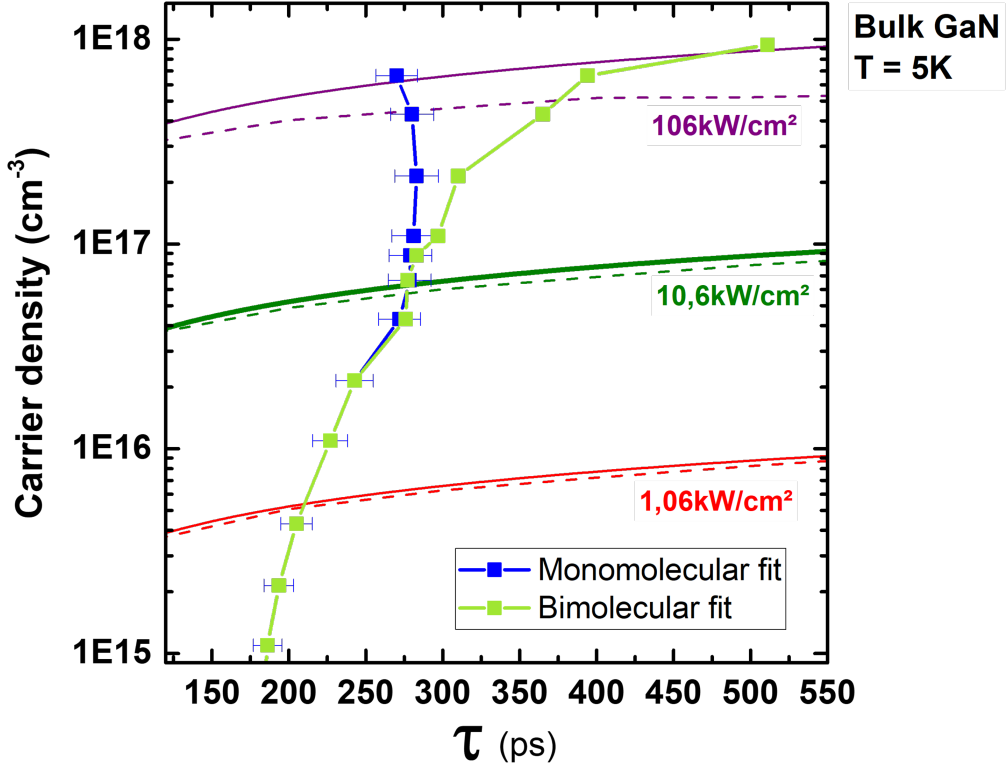


Figure III.18 – Comparative results between monomolecular and bimolecular fits with updated power densities lines. The dotted line were plotted with the influence of the bimolecular recombination term, $\beta = 1.3 \times 10^{-8} \text{ cm}^{-3}/\text{s}$ in this case [111].

efficient. The bimolecular recombination coefficient is a constant that now can be deduced from the variation of the initial carrier density and the lifetime measured in the bulk. We want to verify the values of β obtained by this method.

III.4.3.3 Estimation of the bi-molecular recombination term

Unlike the previous section where only the decay time τ was involved, now two fit parameters, β and τ , are used through coefficients $A1$ and $A2$ as :

$$A1 = n(0)A2 = n(0) \times \beta \quad (\text{III.36})$$

In the use of the decay time fits, the use of the terms τ and β as adjustable parameters modifies the expression initially used, so the equation III.35 becomes so:

$$n(t) = \frac{A1 \times e^{-(x-t_0)/\tau}}{1 + A2 \times \tau(1 - e^{-(x-t_0)/\tau})} + y_0 \quad (\text{III.37})$$

With y_0 the baseline after the time decay, t_0 the origin of the time decay, $A1$ the coefficient

modulating the photoluminescence intensity and $A2$ the fitting parameter composed by the initial carrier density multiplied by the bimolecular recombination term.

We note that τ has been deliberately removed from the parameter $A2$ to avoid redundancy in the fit on the data set. This avoids the compensation of the β term by the τ term. Figure III.19 shows the different values of $A2$ deduced from the fits as a function of the initial carrier density $n(0)$ calculated from equation III.2.

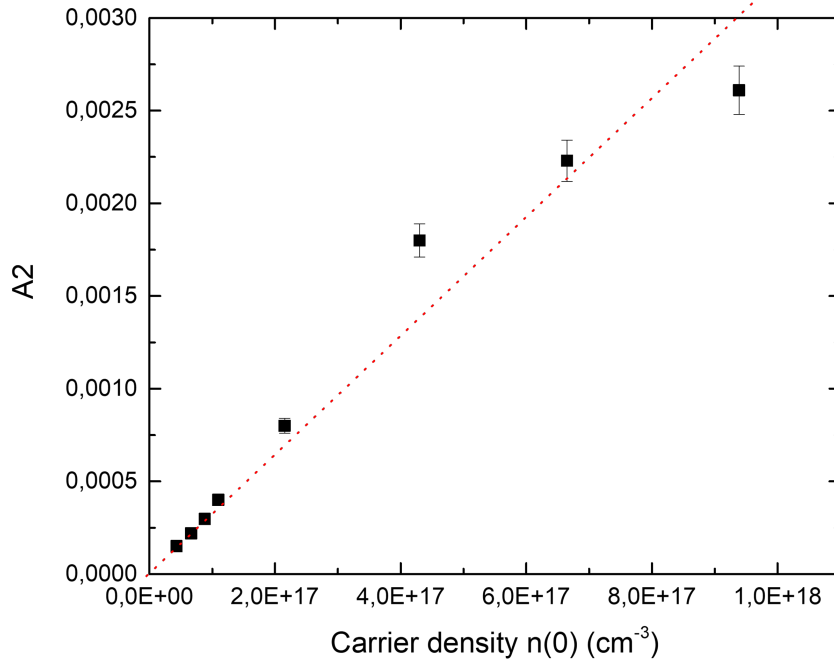


Figure III.19 – Experimental determination of the bimolecular recombination term

At equal temperature, the β term is expected to be constant and does not depend on the initial power density. The $A2$ term is expected to evolve proportionally with the power increase since the only variable on which its growth depends is the initial carrier density. We observe on figure III.19 that the $A2$ term follows an almost linear growth with the increase of the power density. We can therefore easily deduce the bimolecular recombination term according to the following equation:

$$\beta = \frac{A2}{n(0)} \quad (\text{III.38})$$

The values of β calculated as a function of the carrier densities are presented in the following table III.4:

The experimentally determined values are of the order of $(3.4 \pm 0.6) \times 10^{-9} \text{ cm}^3/\text{s}$ and appear to be in disagreement with the values used by Binet et al. [111]. Many values published in the literature focus on room temperature bimolecular coefficient being of the order of $3 \times 10^{-11} \text{ cm}^3/\text{s}$ [132, 133, 134, 135] and Malinauskas et al. calculated and measured a value of $3.2 \times 10^{-9} \text{ cm}^3/\text{s}$

Carrier density (cm ⁻³)	β (cm ³ /s)
4.3×10^{16}	3.5×10^{-9}
6.6×10^{16}	3.3×10^{-9}
8.8×10^{16}	3.4×10^{-9}
1.1×10^{17}	3.6×10^{-9}
2.2×10^{17}	3.7×10^{-9}
4.3×10^{17}	4.2×10^{-9}
6.6×10^{17}	3.4×10^{-9}
9.4×10^{17}	2.8×10^{-9}

Table III.4 – Experimental values of β

at 9K on a sample of the same origin as our bulk sample (epitaxial growth by Lumilog) [136]. The deduced β values we have found appears in agreement with Malinauskas et al. and our fitting method would thus allow to experimentally determine the bimolecular recombination coefficient.

III.5 Conclusion

From an experimental point of view, the determination of the Mott density was a challenge as the experimental carrier determination requires a good understanding of the carrier density evolution in the sample. It allowed us to better approach our experimental methodology and led to many improvements in our workflow by correlating the TRPL and μ -PL experiments. It was interesting to extend the reasoning to find and measure values that are essentials parameters in the knowledge of GaN, such as, lifetimes, experimentally measured carrier density and finally the influence of the bimolecular recombination term. These studies started from the observation of a scaling law between the exciton binding energies of GaN and ZnO, and we find that this law is also preserved for other wide gap semiconductors: reported values of the excitonic Mott density at low temperature (< 25 K) in other wide gap semiconductors are listed in table III.5, the value corresponding to GaAs is also reported for information.

	CuCl[137]	Cu ₂ O[138]	ZnO[68]	CdS[139]	GaN*	GaAs[140]
E_b (meV)	190	150	60	29	25	4.2
n_{Mott} (cm ⁻³)	5×10^{19}	3×10^{18}	1.5×10^{17}	5×10^{16}	6×10^{16}	7×10^{15}

Table III.5 – Summary of exciton binding energy and Mott densities at low temperature ($T < 25$ K) for wide bandgap semiconductors. The value corresponding to GaAs is also reported. (* this work)

To summarize the progress made with our different studies, figure III.20 presents the estimated Mott density as a function of the excitonic volume. To illustrate the scaling law two materials are

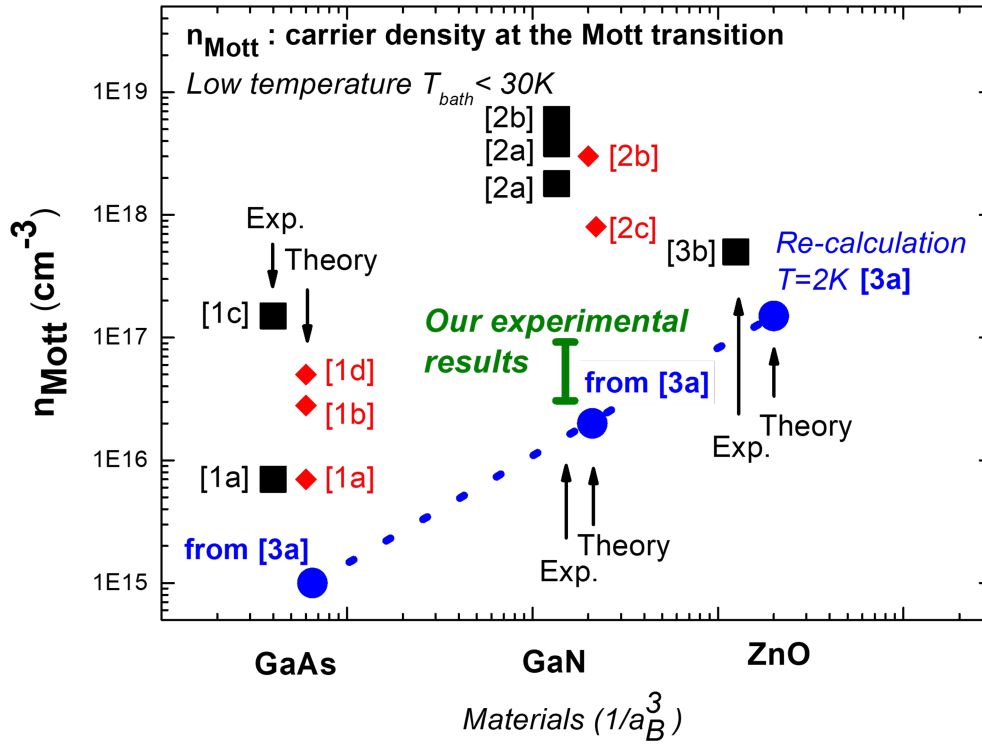


Figure III.20 – Scaling law of different Mott transition estimations found in literature at temperature below 30K (calculated and experimental). a_B being the Bohr radius and $1/a_B^3$ the excitonic volume.

compared to GaN, a well-known small gap semiconductor GaAs, and ZnO which feature higher exciton binding energy. The values of Mott density are reported in two different categories: experimental results are presented in black squares and theoretical ones in red points. A renewed theoretical calculation of the Mott density at 2K from the Versteegh model introduced in chapter I.7.3.3 is displayed in blue and is used as a base-line for our new estimation. This line is considered such as the lower boundary of the calculated Mott transition. This figure also shows that both previous experimental and theoretical reported values for GaN Mott transition are equal to or higher than those of ZnO despite the ZnO larger excitonic binding energy in comparison with that of GaN (60 meV versus 25 meV). Furthermore, it should be noted that because of the GaN larger Bohr radius (4.2 nm for GaN versus 1.8 nm for ZnO), the excitonic Coulomb interaction screening with the increase of the excitation intensity should be more efficient in GaN than in ZnO.

Spectroscopy of single core-shell nanowires

This chapter is devoted to the study of the optical properties of single nanowire. Indeed, as stated by Gorgis [141], nanowires "exhibit different properties due to different lengths, diameters, and shapes because of random nucleation processes and local fluctuations in the growth parameters". Even if those nanowires were obtained by self-organized growth by molecular beam epitaxy (MBE), the same observation is made on our sample. This inhomogeneity in the nanowire morphology, limits the precision of optical transitions due to averaging effect and the optical characteristics are not representative of the optical properties of individual nanowires [141, 142]. In order to gain more accuracy and to limit the averaging effect we chose to analyze single nanowire.

The work previously done on the bulk sample and the optimization of our experimental setup opens the way to the experimentally difficult study of single nanowires. Nanowires study is experimentally difficult due to their small size and thus the low luminescence signal intensity as compared to bulk sample.

In order to fully characterize our samples, it is therefore necessary to have a rigorous experimental workflow following the methodology demonstrated in chapter III (studies in power and temperature, time-resolved spectroscopy). As demonstrated by [142] on MBE self-induced grown nanowire and was also observed in our MOCVD sample grown samples, the growth technique will have a huge impact on the optical transition measured and results varies between growth techniques, aspect ratios and structures of samples. This single nanowire optical characterization work is essential as it aims at the optimization of the structures for electrical injection. The laser effect in nanowire through electrical injection remains a technological challenge especially achieving sustainable contact onto the nanowire under high current injection and only a few work has achieved it. Duand and Lieber's team have demonstrated an electrically pumped nanowire lasing effect around 509 nm by utilizing p- silicon/n-CdS heterojunctions [98]. Afterward, few work has been done on nanowire laser under electrical pumping and more remains to be done on electrical injection in GaN based materials [143]. The objective of this chapter is therefore to understand the impact of the nanowire structure (especially for a doped nanostructure) on the optical properties in order to realize a nanowire laser under electrical injection.

IV.1 Sample presentation

In order to carry out those different experimental campaigns in the same way as the bulk reference sample different structures have been chosen. The first idea was to study the optical properties of a single undoped GaN nanowire. But on the growth side it was not possible to achieve the sufficiently high nanowires without adding silane in the MOCVD growth reactor. The need of silane in order to enhance the vertical growth rate during the growth of GaN nanowires by MOCVD (using a continuous flow growth mode) has been published by several groups indeed [144, 145, 146, 147]. Therefore we decided to study a n-i core-shell nanowire, chosen to characterize the intrinsic shell in order to measure the optical transitions and to compare the results with our bulk reference sample. The second sample is n-i-p core-shell nanowire designed to achieve electrical injection through a radial p-n junction. It is the structure allowing the laser effect optical characterization. These nanowires are MOCVD grown through selective area growth using a SiO₂ mask on GaN templates of Ga polarity. The growth conditions were optimized as described by Coulon et al. [148].

IV.1.1 CC0414

CC0414 is a n-i-p core shell sample on which the core is n-doped, 450nm thick, followed consecutively by a 140nm thick intrinsic shell and a 110nm thick p-doped shell.

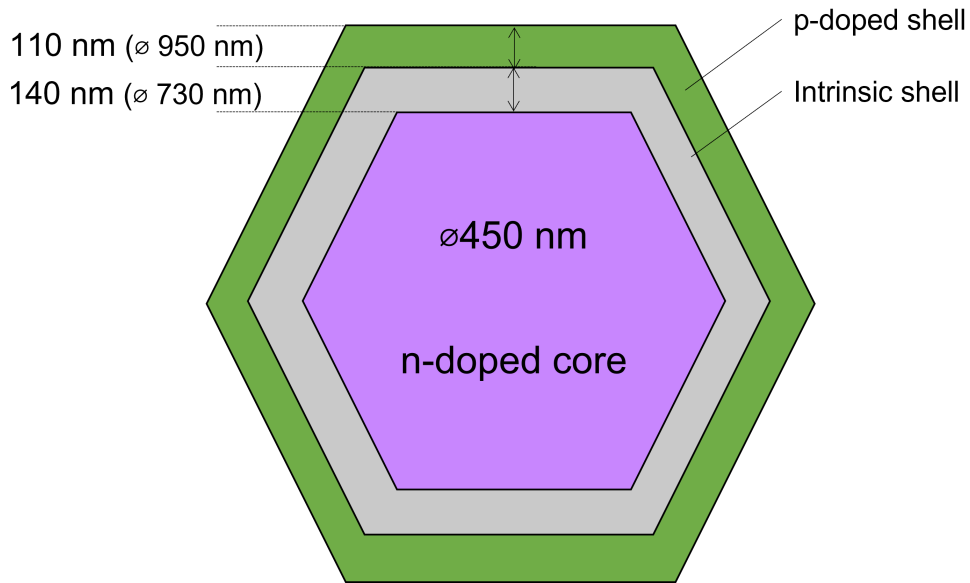


Figure IV.1 – Schematic view of a typical n-i-p core shell nanowire.

The cross-section of the sample has been schematized in figure IV.1 and allows to better represent the thicknesses between each layer. The nanowires feature a Si-based n-doping of the order of $5 \times 10^{18} \text{cm}^{-3}$ and a Mg-based p-doping of the order of $1 \times 10^{19} \text{cm}^{-3}$. The doping level has been estimated on planar devices with similar growth conditions. Although the size is not perfectly homogeneous over the whole sample, the aspect ratio is similar along each nanowires and the typical measurement

range from 2 to 5 μm in length as visible on the scanning electron microscope (SEM) measurement presented in figure IV.2.

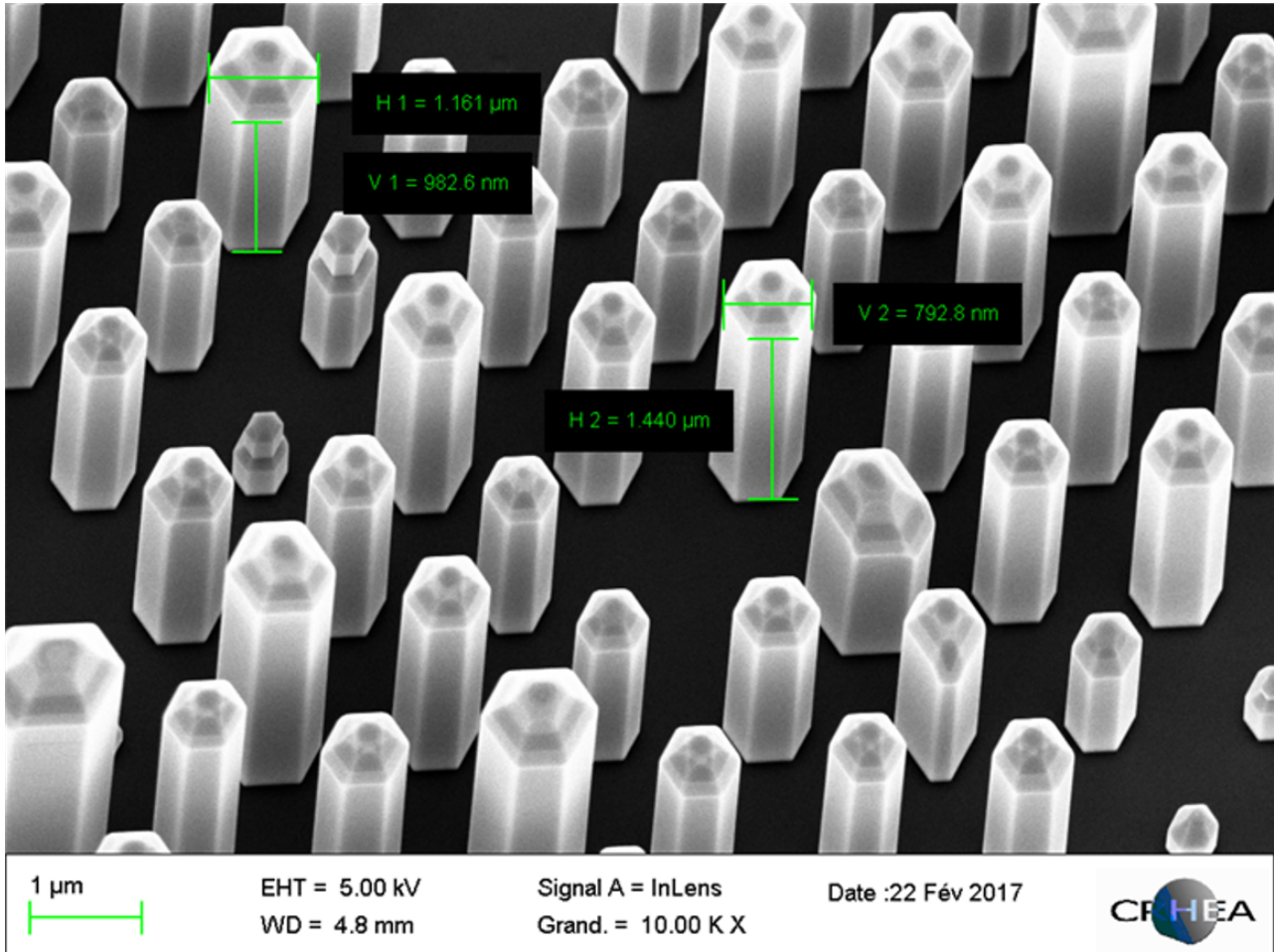


Figure IV.2 – SEM measurement of as grown CC0414 sample. "H" values are for the length and "V" values are the nanowire diameter. tilted view with 25deg

The apex is of a generally pointy shape and as seen on the detailed picture IV.3 also measured by SEM, it is possible to distinguish the different shells visible by contrast variation. The final goal of those structured nanowires is to create a p-i-n junction by contacting the p-shell and the n-core. To perform the single object study, the nanowires were dispersed on a sapphire substrate. The difference of optical index and thermal resistance was taken into account during the choice of the substrate: if the substrate has a too important difference of optical index with the studied sample, it would have for consequence to absorb the luminescence coming out of the sample, and if the substrate features a bad thermal resistance coefficient, it would cause the overheating of the sample.

The first SEM measurement gives an overview of the nanowires distributed on the substrate and gives the average aspect ratio of the wires. The measurement written do not take in account the SEM tilt (around 25 deg), thus the real dimensions are rather of the order of 2 to 4 μm in length (a factor of 2.4 is added to the measurement to compensate the tilted view).

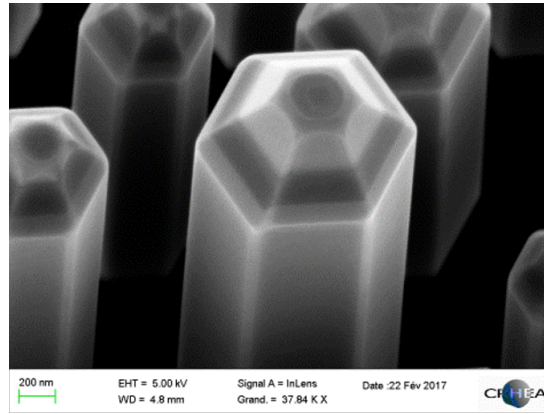


Figure IV.3 – Close up of the CC0414 Apex measured by SEM. The difference in shades shows the different core and shell layers of the nanowires.

IV.1.2 CC0287a

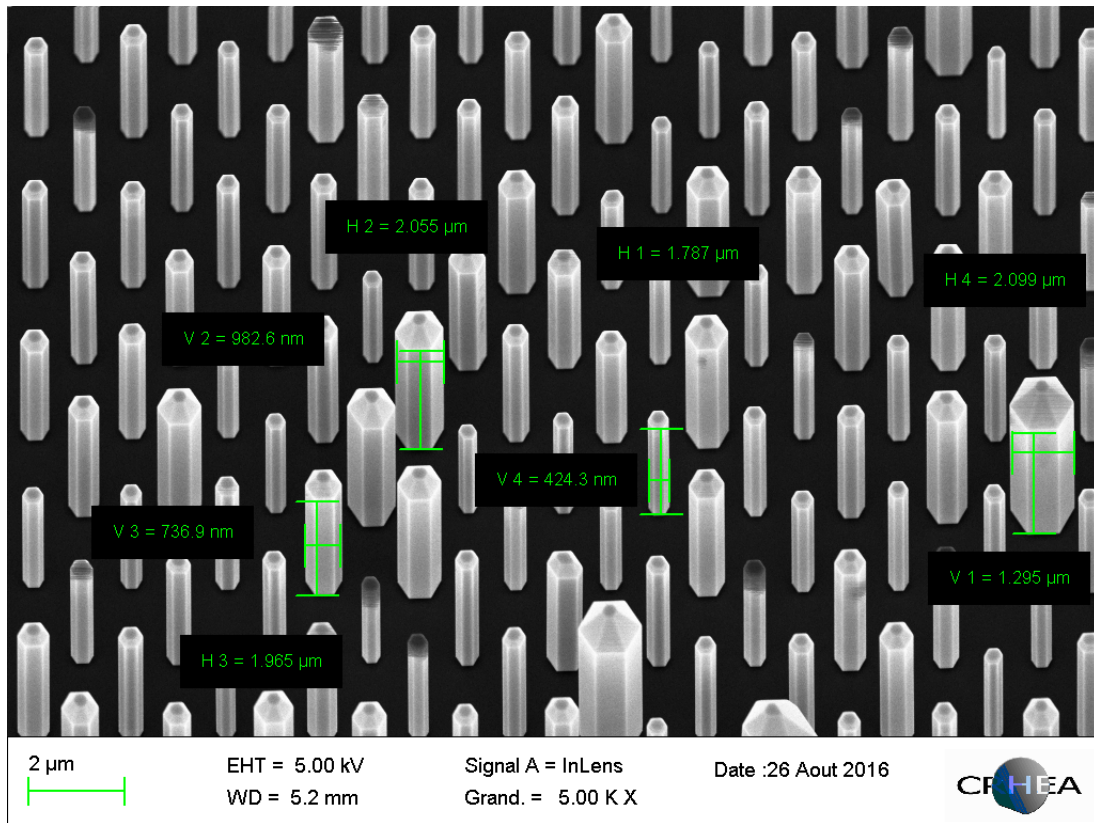
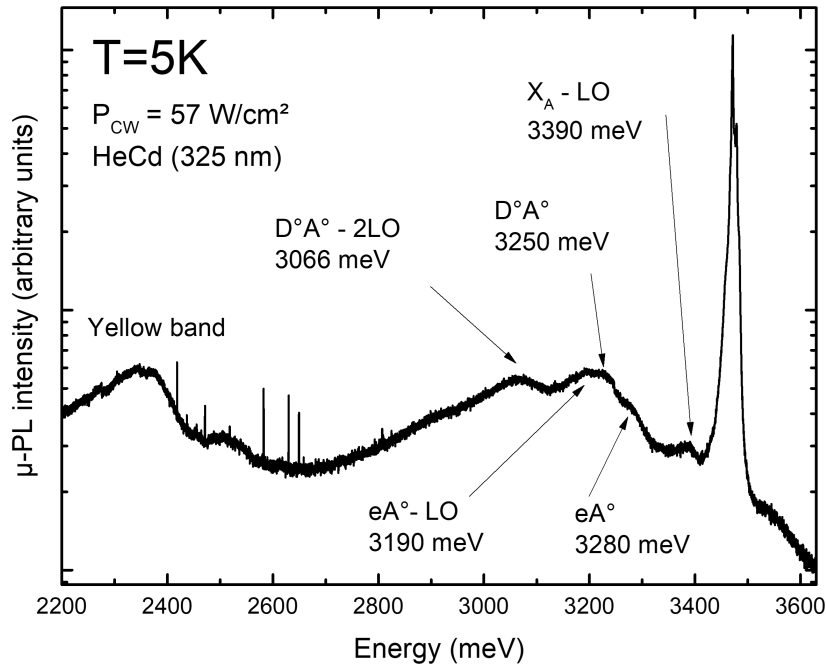


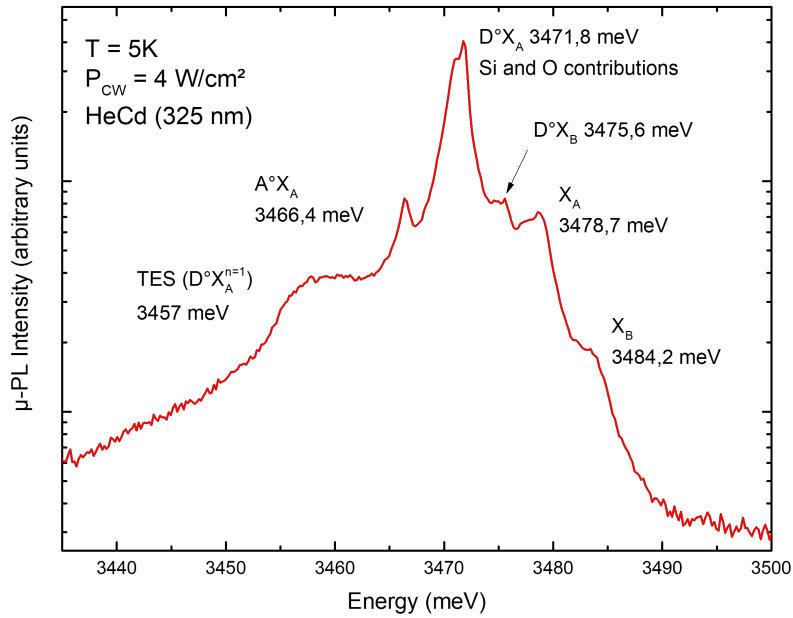
Figure IV.4 – SEM measurement of as grown CC0287a sample. "H" values are for the length and "V" values are the nanowire diameter. Tilted view with 25deg angle.

The CC0287a nanowire consists of an n-doped core and an intrinsic shell whose thickness is around 100nm without however being precisely measured. The typical length of nanowires are 2 to 4 μm long as shown in figure IV.4. For the study of a single object, these nanowires were scattered on an etched Si grid, so as to more easily identify each wire. Therefore, the sample CC0287a has been

particularly used for these campaigns: as the nanowires are scattered on a Si grid, it is very simple to identify a single object and to conduct in-depth campaigns always on the same identified wire.



(a) μ -PL spectra at low temperature under continuous excitation (HeCd excitation laser at 325 nm). Excitons transitions are more intense than donor acceptor pairs (DAP) and results are similar to those of strain-free bulk GaN.



(b) μ -PL spectrum of single n-i nanowire at low temperature featuring clearly visible excitons transitions.

Figure IV.5 – μ -PL spectra at 5K of a single n-i core-shell nanowire

Figure IV.5 summarizes the typical PL spectra measured with CW laser excitation. In figures

IV.5a IV.5b the photoluminescence intensity is plotted as a function of the photon energy. The first figure IV.5a shows a wide energy range featuring D^0A^0 and eA^0 respectively at 3250 and 3280meV and their respective LO phonon replica [149]. The yellow band is also visible at lower energy. The luminescence of excitonic peaks are detailed in the second graph.

Figure IV.5b shows a photoluminescence spectrum measured at low temperature (5K) and low power density using the HeCd continuous wave (CW) laser. We note that the excitonic transitions are sharp and that the energies of the free exciton A bound to a neutral donor D^0X_A measured at 3471.8meV with the splitting due to the contribution of the Oxygen and Si donors is visible. The free exciton B bound to a neutral donor D^0X_B measured at 3475.6meV [150] is also visible. The free excitons X_A and X_B are respectively recorded at 3478.7meV and 3484.2meV. The results are similar to those measured in unstrained bulk GaN.

In this preliminary study we show that the measured photoluminescence corresponds indeed to that of an undoped GaN sample, previously presented in the section III.2 in chapter III. Only the intrinsic shell seems to contribute to the luminescence signal. Since the depth of absorption for GaN $1/\alpha$ is in the range of 90nm (with $\alpha = 1.2 \times 10^5 \text{ cm}^{-1}$) these results confirm the hypothesis that the intrinsic shell is more than 100nm thick.

IV.2 Optical characterization of a single nanowire

IV.2.1 Power study

The studies conducted on a single wire are power studies with several types of excitations: first using the continuous HeCd laser with low excitation densities and then using the pulsed Qswitch laser, allowing to inject higher carrier densities. Through the following sections the experiments were made on a single n-i nanowire. All the presented results involving the n-i nanowire were measured **on the same nanowire**.

IV.2.1.1 Continuous excitation

The photoluminescence spectra recorded as a function of excitation intensity are shown in figure IV.6. We find again that the free excitons and the bound excitons exhibit narrow peaks. The power dependent results are not significantly different from those of the bulk. The redshift starts from 14 W/cm^2 and is increasing for higher excitation intensities. For the X_A peak, the redshift goes from 3481 meV to the main peak at 3469meV for 358 W/cm^2 . This 12 meV redshift is more important than the 3 meV measured in bulk GaN. We can make the hypothesis that the continuous excitation generate a strong heating effect leading to thermal activation energy high enough to facilitate the ionization of carriers. The analysis of the redshift will be discussed more precisely in the following sections.

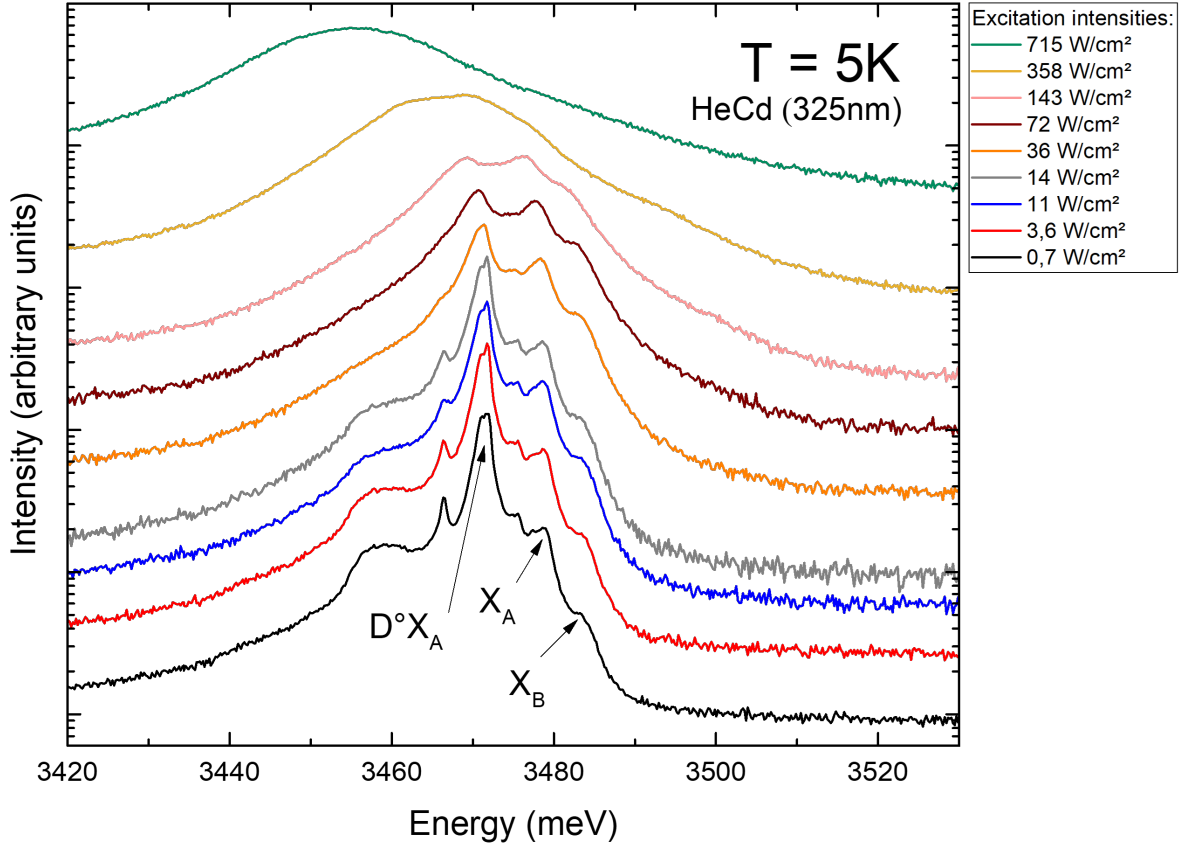


Figure IV.6 – μ -PL measurement of a single n-i core-shell nanowire made with CW HeCd continuous excitation at low temperature.

Two effects can be seen on those spectra with the increasing of the power density: first of all there is a relative intensity variation between D^0X_A , X_A and X_B . The luminescence of the free exciton X_A becomes dominant to that of the exciton bound to a neutral donor D^0X_A with the increase of the power density, until it exceeds it in intensity at 143 W/cm^2 . Then, those intensity variations are combined with a redshift of the spectrum starting at 14 W/cm^2 with a characteristic broadening of the luminescence peaks, associated to an increase of the associated electronic temperature around 100 W/cm^2 . The peak broadening associated with the redshift is a typical signature of high electronic temperature. In contrast to the result obtained with a bulk reference sample, exciton signatures remain visible for all the spectra except the highest intensity recorded, i.e. starting from 715 W/cm^2 . There is no visible evidence of exciton screening under this CW excitation. Moreover the redshift and the broadening clearly depicts the consequences of the heating effects on the excitonic transition.

Figure IV.7 shows the electronic temperature fit at high energies for the two highest power densities. The measured temperatures are about 190 K for 360 W/cm^2 and 250 K for 715 W/cm^2 for a lattice temperature of 5 K . The wire heats up a lot and explains initially the delocalization effects, favoring the X_A peak at the expense of D^0X_A starting from 143 W/cm^2 . An interpretation of these effects can be decomposed in two steps: first of all, the delocalization of the trapped excitons on the neutral donors D^0 contributing to X_A and X_B increasing relative intensity compared to the donor

bound transition. Also, D^0h transition is expected to replace the D^0X_A transition as the neutral donor bonded hole energy is slightly superior than the one of D^0X_A . The electronic temperature inducing delocalization energy is too high to preserve D^0X_A transitions as such. Secondly the ionization of the neutral donors D^0 coupled to the gap reduction characterized by the observed redshift. It is possible to estimate the lattice temperature from the redshift following Vinã law that will be presented in detail later. With a 13 meV redshift at 360 W/cm^2 excitation intensity, the lattice temperature would be around 110K, confirming the analysis of the D^0h transition instead of the D^0X_A one.

The main luminescence peak broadens but the excitonic signature is still perceptible at 360 W/cm^2 , leading to a conclusion that the vanishing of the excitonic signature is essentially temperature dependent instead of the carrier dependent self-screening as seen in the bulk sample. Interestingly, the redshift further progress toward 3456 meV at 715 W/cm^2 , thus adding 10 meV to the previous 13 meV measured redshift.

From this standpoint, it is hard to be certain of the nature of this peak as no excitonic feature can be seen adding to the fact that the electronic temperature is high. An hypothesis that can be made would be that the n-doped core can contribute to the luminescence of the i-shell at high excitation power.

We will now compare the photoluminescence spectra obtained with continuous and pulsed excitation to probe very large power density ranges.

IV.2.1.2 Pulsed excitation

Figure IV.8 is also a stack of spectra measured for increasing excitation intensities at low temperature. The aim of the measurement with the Qswitch is twofold: to find in very weak signals the signature of excitons at energies already measured with the HeCd and to see if the single wire was able to trigger a lasing effect at higher excitation density. We can see that for the first spectrum measured at a peak power density of 1.7 kW/cm^2 , the excitons bound to a neutral donor D^0X as well as the free excitons X_A are visible for energies of 3471.3meV and 3478.2meV respectively. We find here the energies measured on the figure showing that our experimental setup is well mastered for small signal and single object measurements.

The signal of the free excitons X_A is still weak as seen for a density of 4 kW/cm^2 then with increasing power density, the signal broadens and a redshift of 5 meV occurs giving an estimated lattice temperature around 84 K. Finally there is no lasing effect at higher power density. It is interesting to recall that in the confocal excitation configuration, the spot diameter is $78.5 \mu\text{m}^2$ and is well controlled allowing repeatable and accurate measurements. The electronic temperature is around 160K for an excitation density of 60 kW/cm^2 . This result also highlights the difference between continuous wave excitation and pulsed excitation. The repetition rate is low enough to allow the sample to "cool down" explaining why the calculated temperature does not exceed that calculated with CW excitation. The first spectrum at the power density at 2.2 kW/cm^2 still displays excitonic features with D^0X_A and free excitons X_A respectively at 3471.3 and 3478.2 meV but with increasing excitation density the

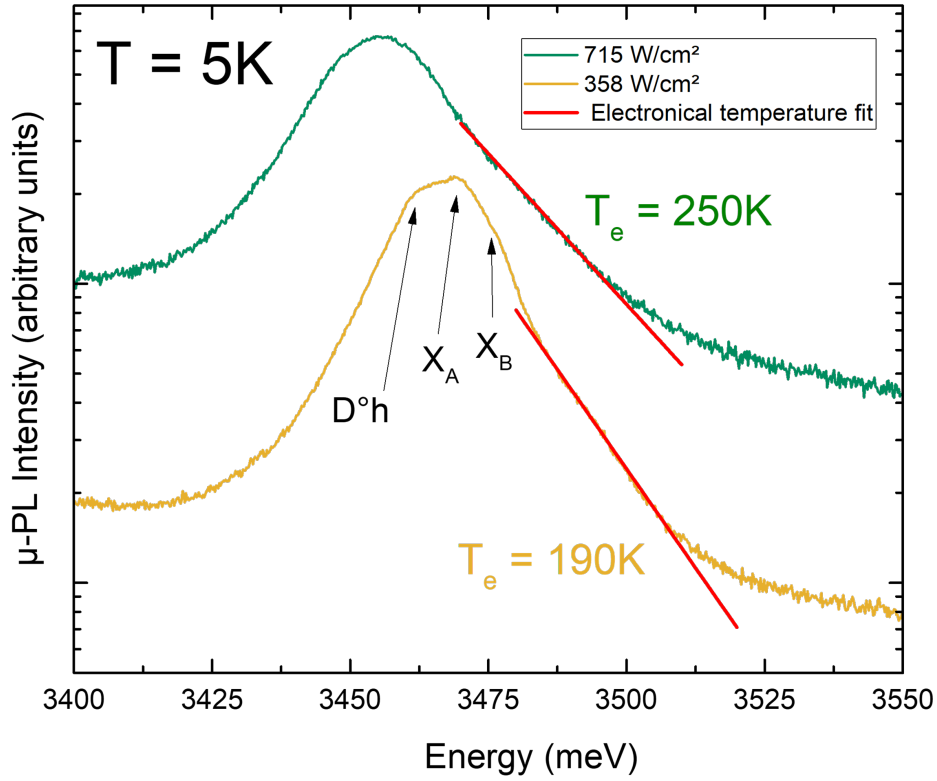


Figure IV.7 – Single n-i structured nanowire μ -PL spectra recorded at 5K featuring high energy tails fit to determine electronic temperature. D^0X_A , X_A and X_B signatures are still visible at 358 W/cm² but disappear at higher excitation density with the broadening of the spectrum.

broadening is too important to distinguish them. We can see that the relative intensity between the two excitonic features is close and follows the same behavior of the previous high excitation density CW-excitation spectra, that is to say an high electronic temperature induced broadening and an increase in the intensity of X_A regarding D^0X_A through the delocalization of neutral donor bonded excitons.

We know from this first campaign that the probed area corresponds to the intrinsic shell, the results obtained being in perfect agreement with those measured in our reference sample of strained free bulk GaN and also shows that as expected, nanowires are strain free. We have seen on the bulk GaN sample that the temperature affected the excitonic transitions. In order to fully characterize the sample and to see the effect of the temperature on a single nanowire, a temperature study was conducted.

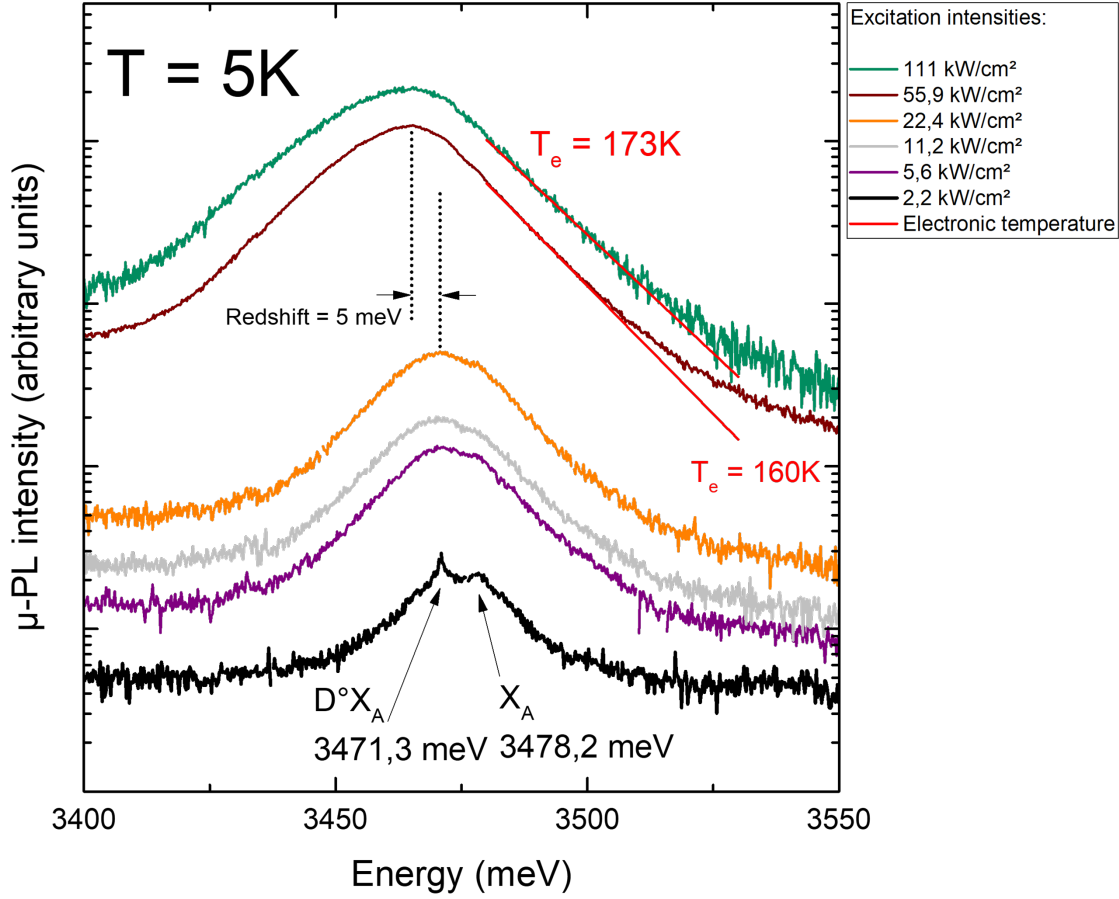


Figure IV.8 – Single n-i nanowire μ -PL spectra measured with a Q-switched pulsed excitation.

IV.2.2 Temperature study

A complete temperature study was conducted on the same single nanowire in order to observe the evolution of excitons according to the temperature. The figure IV.9 shows a series of different spectra measured for the same power density from a continuous excitation with the HeCd laser.

It is interesting to follow the different luminescence peak characteristics of bound excitons D^0X and free excitons X_A , X_B . The analysis at 5K has already been performed on figure IV.6 and is our starting point. The energies of D^0X , X_A and X_B do not shift for up to 50K, but beyond that we mark a progressive redshift first visible on the excitons bound to a neutral donor, then on the free excitons. Moreover, the luminescence peak of the free exciton X_A becomes predominant, exceeding the μ -PL intensity of D^0X from 70K.

With the increase of temperature and beyond 100K, the peak definition of free excitons is gradually lost. The broadening of the peaks is also noticeable, and can be explained several combined effects. First and foremost, a high thermal agitation energy will essentially contribute to the broadening and the ionization of the excitons bound to a neutral donor will contribute to increase the relative intensity of free excitons X_A . The complete delocalization of D^0X_A is expected to occur before 120K as only

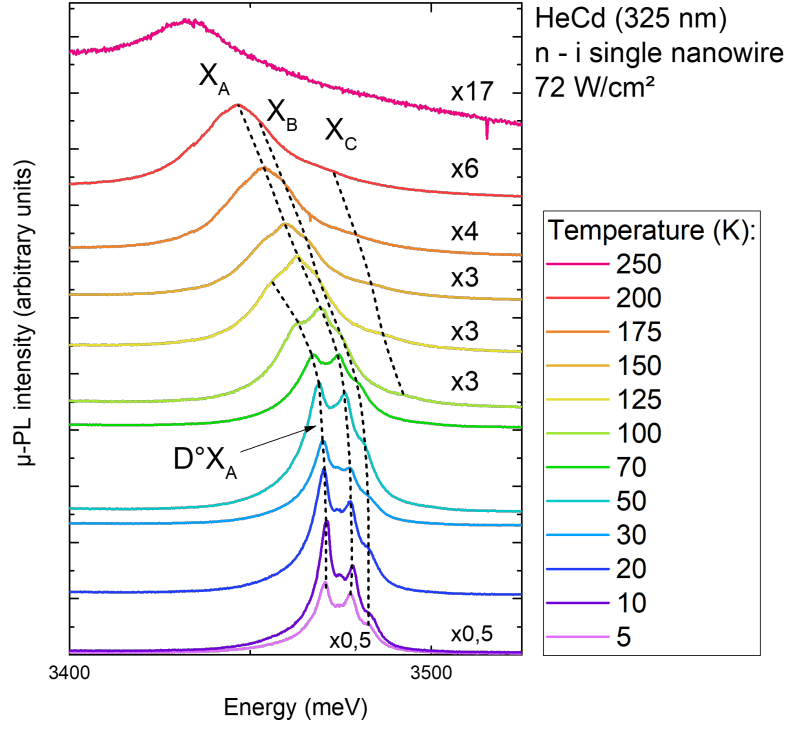


Figure IV.9 – μ -PL Spectra measured on a single n-i nanowire for different temperature ranging from 5K to 300K (ambient temperature)

7 meV are needed to exceed the donor binding energy and the thermally induced energy is estimated to be around 8.6 meV. As it can be seen on the 125K spectra, the D^0X_A signature is barely visible past this temperature. Beyond 175K, the broadening is such that it is no longer possible to distinguish each of the contributions and an hypothesis would be that an electron-hole plasma would contribute to the luminescence.

The evolution of the gap energy E_g with temperature is described by the Vinã law [151]. It also allows to simulate the dependence of the energy of the excitons as a function of the temperature. The latter is written:

$$E(T) = E(0) - \frac{2a_B}{e^{\Theta_B/T} - 1} \quad (\text{IV.1})$$

where E_0 is the band gap energy at 0 K, Θ is the Debye temperature and T denotes the temperature. a_B is an adjustable parameter characteristic of the material. Several values of a_B and Θ depending of the free exciton energy can be found in work of Ouloum Aoudé [62]. The reduction of the band gap energy is caused by two mechanisms: firstly the electron-phonon interactions [152] and to a lesser extent the thermal expansion of the lattice [153].

The graph in figure IV.10 represents the evolution of the energy of the different peaks measured by photoluminescence as a function of temperature. It is possible to plot the evolution of the energy of D^0X until its disappearance around 125 K, the peaks of X_A and X_B is observable until around 200K.

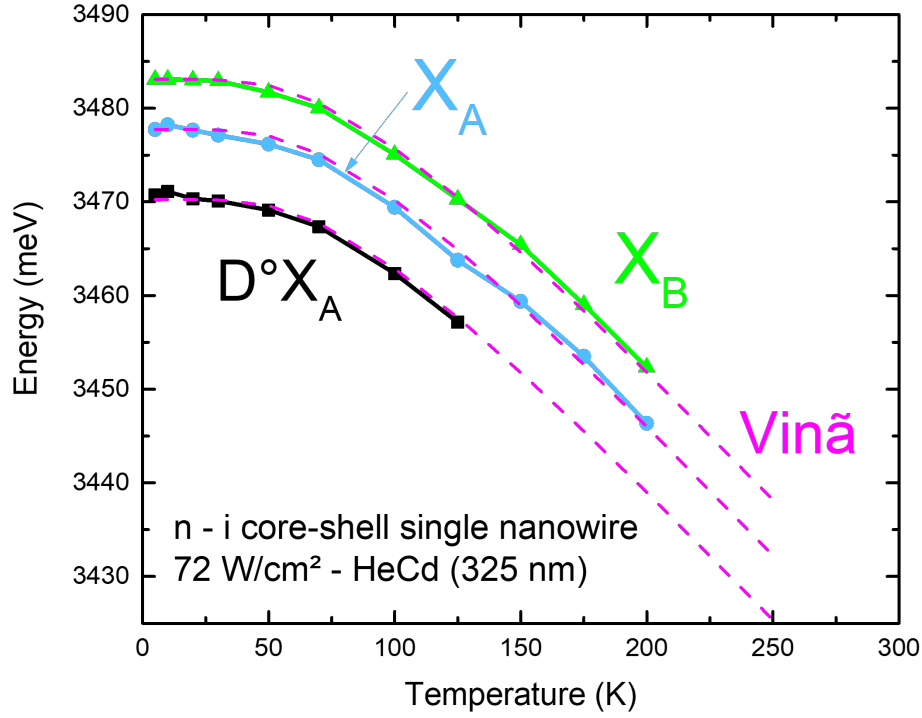


Figure IV.10 – Vinã law fit on a single n-i nanowire. This law allows to give the temperature dependence of corresponding exciton energies.

As the temperature increases, the excitons move to lower energies as does the band gap energy. In the studied temperature range, this phenomenon is essentially related to the phonon-exciton interaction. The fitted Vinã law perfectly describes the evolution of the measured energy of excitonic optical transitions.

This fit can also be used to describe the evolution of the lattice temperature regarding the measured redshift: for example, in the figure IV.6, the redshift is around 22.9 meV between the lowest and the highest power densities giving a lattice temperature of 110K. From this temperature, the thermal agitation energy is deduced from the lattice temperature. In this example, the energy is of the order of 9.5 meV, thus exceeding the 7 meV neutral donor bound exciton binding energy resulting in the D^0X_A delocalization.

Generally, the results of these first experimental campaigns show the similarity between the optical characterizations of the bulk and the single nanowire, with the main optical transitions at the same energy. It is difficult to perfectly quantify the impact of the n-i structuring of the wire as the results seem to come from the surface layer of the wire, and thus, from the intrinsic layer. At low excitation density the impact of the core on the luminescence of the shell seems to be null (due to its sufficient thickness) but at higher excitation intensity, it is possible that it influences the optical transitions.

To complete the characterization of the single wire, an extensive time-resolved photoluminescence campaign was performed.

IV.3 Single nanowire time-resolved spectroscopy

The setup used is the same as the one presented in the chapter III in the case of the bulk sample. The TRPL campaign took place in two steps: first at low temperature, benefiting from a sufficiently large signal to extract points covering a wide range of power density, then in a second step, by varying the temperature to measure its influence on the carrier lifetime.

IV.3.1 Single nanowire TRPL at 5K

At low temperature, TRPL spectra obtained on the same single wire previously studied in μ -PL show a double contribution, thus suggesting the presence of a short and a long time. A typical spectrum at 5K is shown in figure IV.11 with two fits being applied: the first purple dotted line is a mono-exponential similarly used during the previous chapter III following the expression:

$$y = y_0 + A_1 e^{-(t-t_0)/\tau_{mono}} \quad (\text{IV.2})$$

The second fit, in red dotted line, used to extract the carrier lifetimes is of the bi-exponential expression type:

$$y = y_0 + A_1 e^{-(t-t_0)/\tau_1} + A_2 e^{-(t-t_0)/\tau_2} \quad (\text{IV.3})$$

With A_1 , A_2 being fit coefficients, t_0 the time to slope inflection, y_0 the offset level adjustment and τ_1 , τ_2 the two decay times deduced from the fit. It is interesting to compare the coefficients A_1 and A_2 since they allow us to weight the importance of one exponential compared to the other. In this case, in the results obtained at 5K, the A_1 term is ten times greater than that of A_2 indicating that the main contribution of the decay can be attributed to the shorter lifetime. All the other TRPL decays at higher excitation density can be fitted by using only a monoexponential function. It has been indicated in the paper of Izumi et al. [154] that the presence of these two lifetimes can be explained such as a radiative recombination is partly contributed not only from bi-molecular process but can also be explained by the presence of two regions having different recombination times. That is to say that there can be structural inhomogeneities such as nitride vacancies or point defects that will change the recombination lifetime. As all of other decay time fits are monoexponential, the hypothesis where the nanowire features inhomogeneities would be the most evident one. This inhomogeneity is not measured for other excitation densities and implies that our excitation spot may have been slightly moved from the initial measured area. The femtosecond chain induced by the excitation laser has been known to slightly shift if not perfectly locked and this result can be justified by the fact that the

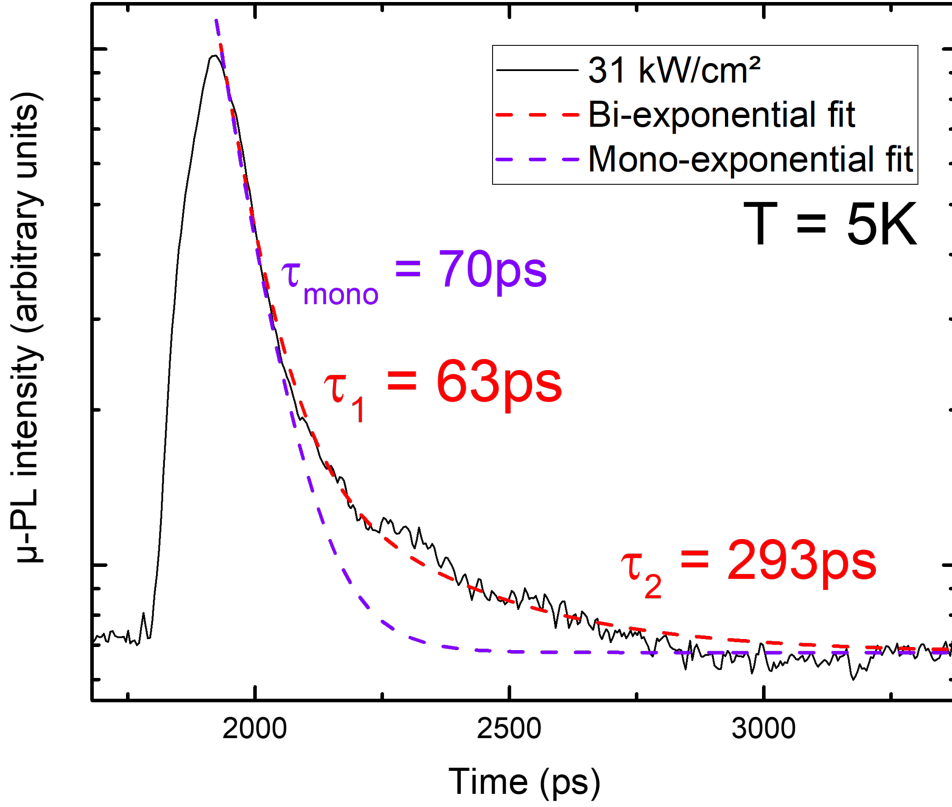


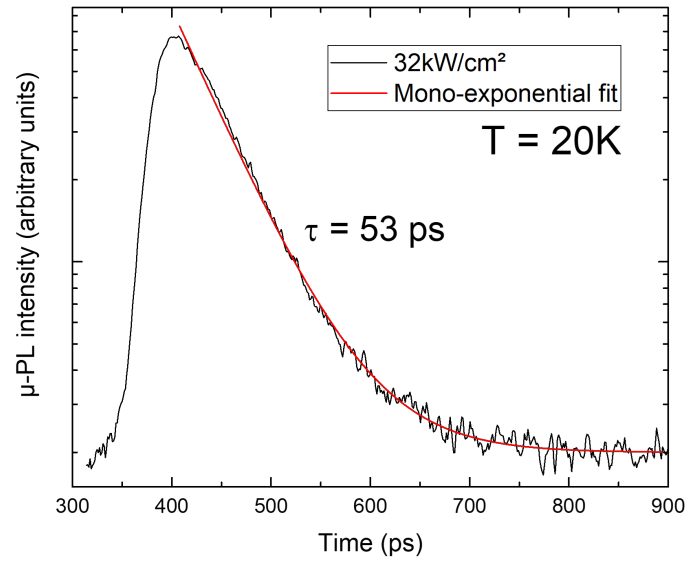
Figure IV.11 – Time resolved photoluminescence fit for a single n-i nanowire at 5K. The luminescence exhibit two distinctive slopes, possibly due to inhomogeneities inside the nanowire.

spot is not exactly at the same position between the first measured temperature and the others. We will see later that spectroscopy results are affected by the location on the excitation spot on the nanowire.

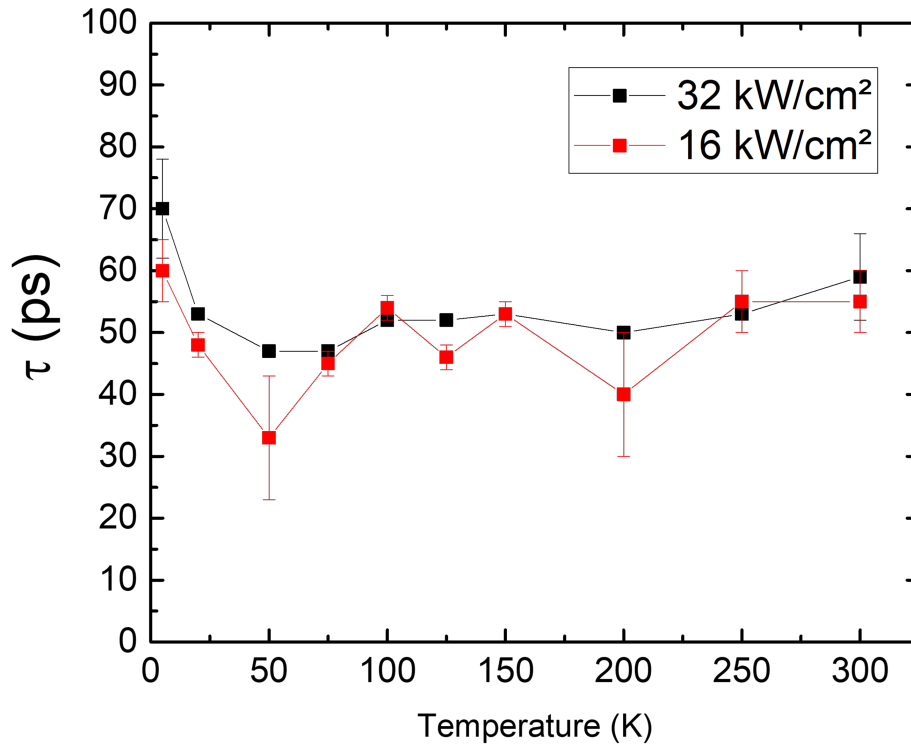
IV.3.2 Influence of temperature on decay times

The extensive characterization campaign on the wire continues with a temperature study. The main difficulty lies in the weak signal extracted from the single nanowire and limits the range of available excitation intensities at different temperatures. All the TRPL spectra obtained, from 20K to 300K are fitted by a simple mono-exponential previously presented. An example of the fit is shown in the figure IV.12a where a linear slope in logarithmic scale can be clearly seen, thus describing the mono-exponential fit. All the measured temperatures for the same density of 32kW/cm² and 16kW/cm² are assembled on the figure IV.12b.

The first point at 5K has already been detailed and suggests that the measured area was not the same as the other points revealing an inhomogeneity along the nanowire. On the other hand, the average time obtained by the mono-exponential fits seems little impacted by the temperature increase



(a) Time resolved photoluminescence fit for a single n-i nanowire at 5K. Decay time is fitted by a mono-exponential.



(b) Summary of the lifetimes measured in a single n-i core-shell nanowire for two different excitation intensities as a function of temperature. The average time is similar between the two excitation intensities and shows a stable evolution.

Figure IV.12 – TRPL campaign featuring power and temperature study on a single nanowire

and gravitates around 50 ps. Those results are similar at lower power density confirming the trend of a lifetime not affected by excitation intensities and does not depend on thermal activation. We note by comparison that the average lifetime of 50 ± 5 ps is quite low compared to the 250 ps measured in the bulk. Therefore the hypothesis can be made of a phenomena inducing non-radiative recombination such as crystal defects, surface recombination or even the existence of an internal electric field at the interface between the intrinsic shell and the n-doped core leading to the formation of a depletion zone. Even if nanowires are known to be stress-free and of high crystalline quality [143], the stability of the lifetimes even if the temperature is rising means that carriers recombination is limited by non-radiative recombination channels [154] thus privileging the hypothesis of point defects, surface recombinations or internal electric field.

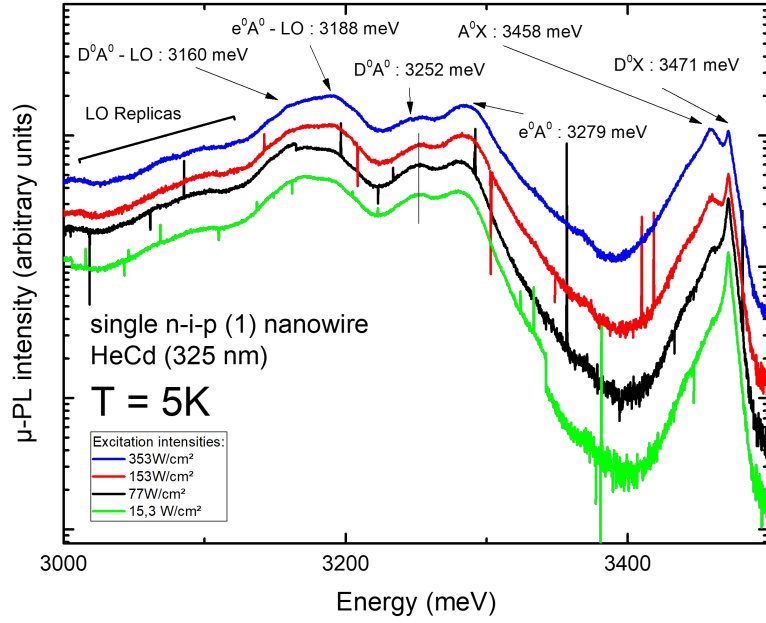
IV.4 Spectroscopy of a single n-i-p core-shell nanowire structure designed for electrical injection

The campaigns conducted on the CC0287a , n-i core-shell nanowire gave a good general idea of the behavior of a single wire under different kind of excitations. This knowledge is useful to better address the more complex structure of the sample CC0414, n-i-p core shell. This structure is the closest to a nanowire that would pass the technological steps toward electrical injection. The number of interfaces makes its analysis and characterization more complex.

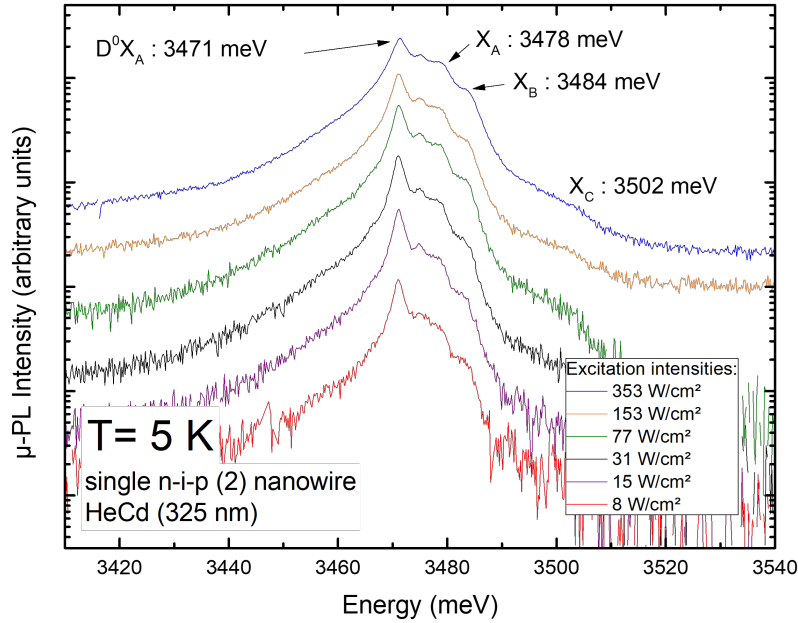
Several campaigns were carried out on different nanowires as the nanowires have shown inhomogeneities in both shapes and luminescence spectra. The results presented in figures IV.13a and IV.13b were measured on different single nanowires dispersed on a sapphire substrate.

The low temperature photoluminescence reveals a good peaks definition of the different excitonic transitions as shown in figures IV.13a and IV.13b. Those two different nanowires (n-i-p (1) and n-i-p (2)) exhibit differences in their μ -PL spectra. The first one presented on figure IV.13a had an interesting luminescence peaks coming from the donor acceptor pairs (DAPs) with their associated phonon replica. The luminescence coming from the DAPs is way higher than the one recorded on the n-i single nanowire showing that the luminescence is coming from the p-doped shell. The second recorded μ -PL spectra exhibits good exciton peak definition with the well-known D^0X_A , X_A , X_B and it is also possible to see X_C at higher energy. Overall, the different energies of the excitonic peaks are consistent with previous measurements performed on the bulk and in the i-n core shell nanowire.

A complementary cathodoluminescence study has been performed at the Centre de Recherche sur l'Hétéro-Epitaxie et ses Applications (CNRS-CRHEA) on a single wire in order to verify the influence of the position on the wire on the luminescence. Nanowires from sample CC0414 was scattered on Si substrate and then analyzed according to three zones, the first zone associated to the red point, is close to the basis of the wire, the second blue point in the middle of the wire and the third zone, green point, is close to the apex.



(a) Photoluminescence spectra of a single n-i-p (1) nanowire for several excitation intensities at 5K.



(b) Photoluminescence spectra focus on excitons peaks measured on a single n-i-p nanowire (2), for several excitation intensities at 5K.

Figure IV.13 – μ-PL campaign results made on several single nanowires

The resulting spectra show a photoluminescence intensity as a function of energy for each area. It is possible to distinguish the band edge exciton line as well as the DAPs around 3.25 eV as expected and we distinguish a variation of intensity depending on the position of the spot on the wire. In the case where the spot is close to the bottom of the wire, on the red point, the signal of the free excitons is lower than the two others and especially the signal of the DAPs is non-existent. The second zone

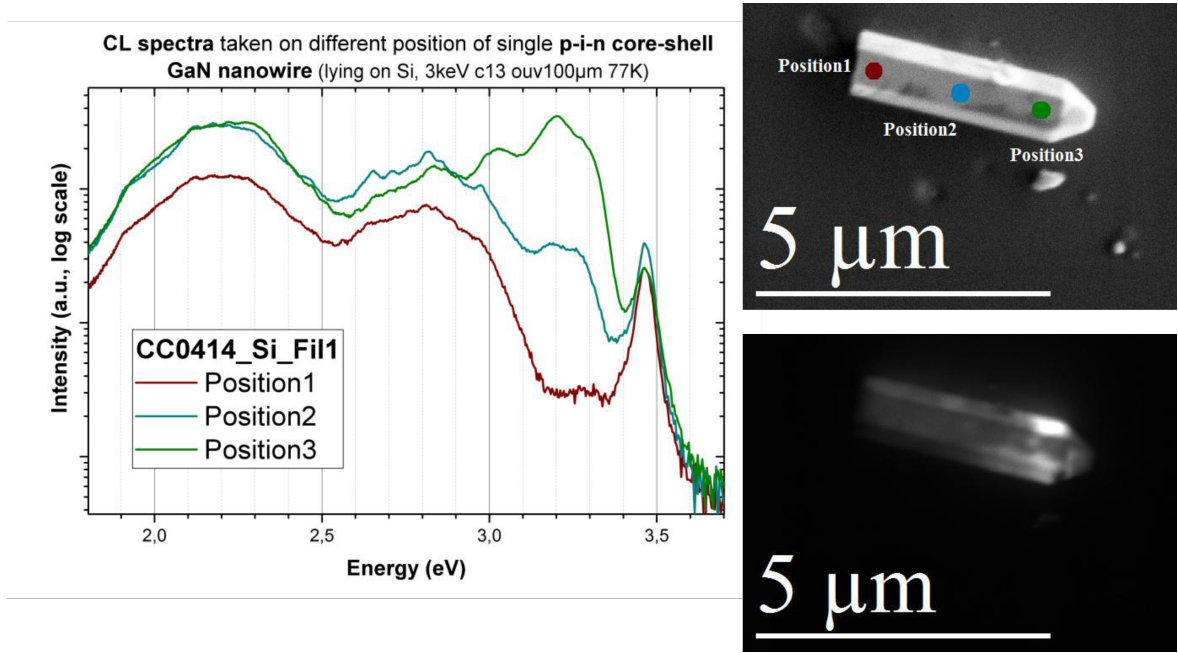


Figure IV.14 – Cathodoluminescence of a single n-i-p (3) nanowire at 77K, the result shows that measured luminescence spectra are affected by the position on the wire.

(blue point) has a strong signal at the energy of the free excitons but a weaker relative intensity at the level of the DAPs. Finally, the third zone near the apex (green point) has the best signal dynamic for the DAPs with a relative intensity recorded from the excitonic peak a little weaker than the second zone. We note on the right hand side of the spectra obtained by real space panchromatic imaging, that the luminescence seems to be extracted mainly on the right end of the nanowire, near the apex. We observe a more intense luminosity around the collar that could be explained by a thicker shell in this zone.

A power campaign was performed on a single wire deposited on a silicon substrate. Figure IV.15 summarizes the power study recorded with the continuous and pulsed laser. The figure can be read in two steps: first the green spectra corresponding to the luminescence as a function of the power density for a continuous excitation, then in red, the luminescence spectra as a function of the power density for a pulsed excitation. This figure summarizes the luminescence of a single n-i-p core-shell nanowire for a large selection of power density covering the very small excitation signals at 0.03 W/cm^2 up to the very high intensity of excitation at 850 kW/cm^2 . On the stack of continuous spectra, we find the peak of excitons bound to a neutral donor D^0X which will be our reference, as well as the characteristic shoulder of free excitons X_A at the expected energy.

At low power density with pulsed excitation (red curves), we find the energy position for D^0X with a strong spectral broadening suggesting that the wire is already heating up a lot essentially due to strong excitation intensities on a single nanowire. The high energy tail being wider is a reliable indicator of the increase of the electronic temperature and it will be calculated in the following part. The excitonic signature is not visible from the lowest pulse power density. As the power density increases, a redshift occurs progressively and a non-linearity appears. The study of this non-linearity

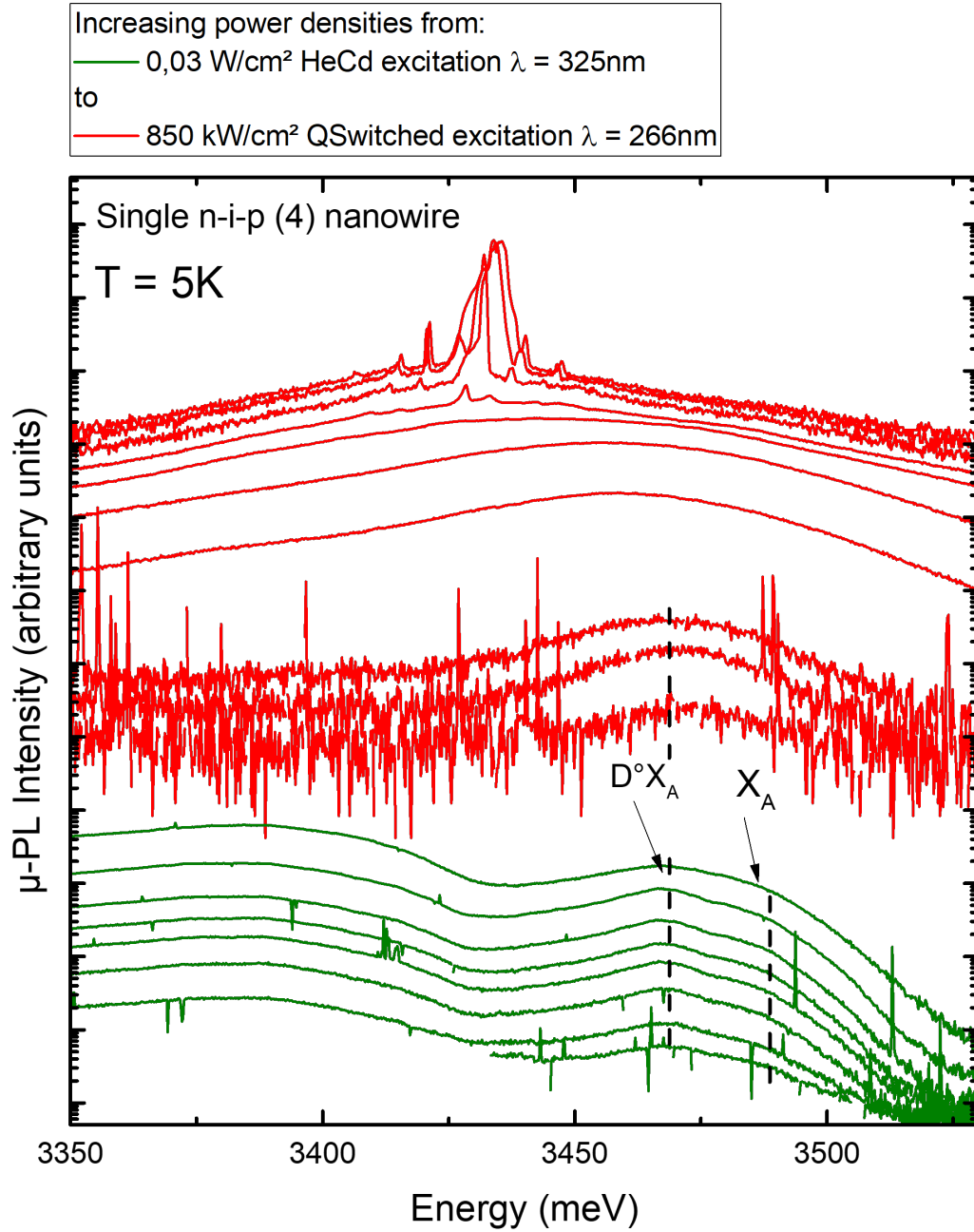


Figure IV.15 – Superimposed power studies featuring both continuous and pulsed excitation for a single n-i-p core-shell nanowire at 5K. Excitonic energies are the same for respectfully the highest power density of HeCd and the lowest power density of the pulsed excitation. This campaign highlight the luminescence behavior for a wide range of power density.

constitutes the study of the lasing effect in a nanowire, developed in the next part.

IV.5 Laser effect in a nanowire

The laser effect is characterized by a non-linear evolution of the photoluminescence intensity as a function of the power density and spectral thinning. The evolution of GaN based laser structures is well described by Johnson et al. [97]. Stimulated emission in bulk GaN at low temperature has been reported at first in thin films in the 1970s [155], and as well as room-temperature lasing [156]. Lasing effect have been achieved in GaN-based micropillar structures with longitudinal whispering gallery modes (WGMs) [157]. Several gain mechanisms are known to characterize laser effect in GaN based samples (bulk or nanowires). The dominant lasing mechanism at high temperature known in GaN is the electron-hole plasma (EHP) [158] and has been reported by Amano et al. at room temperature [159]. It has been published in the literature that nanowires could lead to lower the lasing threshold [141] and would allow enhanced excitonic effects. Thanks to those structures, other gain mechanisms are supposed accessible such as excitonic gain, exciton-exciton (ex-ex) scattering or even polaritonic gain. We seek to observe these phenomena thanks to several photoluminescence campaigns and see if the typical characteristics of the laser effect are found or not.

IV.5.1 Experimental characteristics of the laser effect

Figure IV.16 shows an experimental campaign on a single core-shell n-i-p nanowire (n-i-p (4)) using the QSwitch pulsed laser as excitation source at different excitation intensities. From a power density of 260 kW/cm^2 , a peak can be seen to form and then grow with increasing power density. This "emerging" peak is characteristic of the laser effect with a threshold power (P_{th}). Several peaks also develop at different energies, corresponding to different lasing modes and will also be studied. The global aim of those campaigns is to discuss the origin of the modes and to understand where the resonant cavity, responsible for the laser effect is located in a single wire. The fitted electronic temperature is high with a T_e respectively of 400 and 450 K for 430 and 450 kW/cm^2 respectively.

The evolution of the main peak after the threshold is used to determine the laser effect characteristics. The experimental indicator of a laser effect is the abrupt thinning of the peak associated with its sharp increase with the excitation intensity.

The figure IV.17 displays an image of the evolution of the maximum intensity as a function of the power of the main peak. The graph is divided in two parts: the first part is plotted with gray points, corresponding to the measured points before the laser threshold and the second part in color, corresponds to the measurements after P_{th} . The non-linearity is visible for the main peak with a strong increase of the maximum intensity once the threshold power is exceeded.

The figure IV.18 displays an image of the same single n-i-p nanowire under quasi continuous excitation at high excitation intensity. This so-called 1D picture shows the length of the nanowire (measured in pixel on the y axis) and the resulting luminescence wavelength on x axis. We can clearly see that the luminescence is extracted near the extremities of the nanowire.

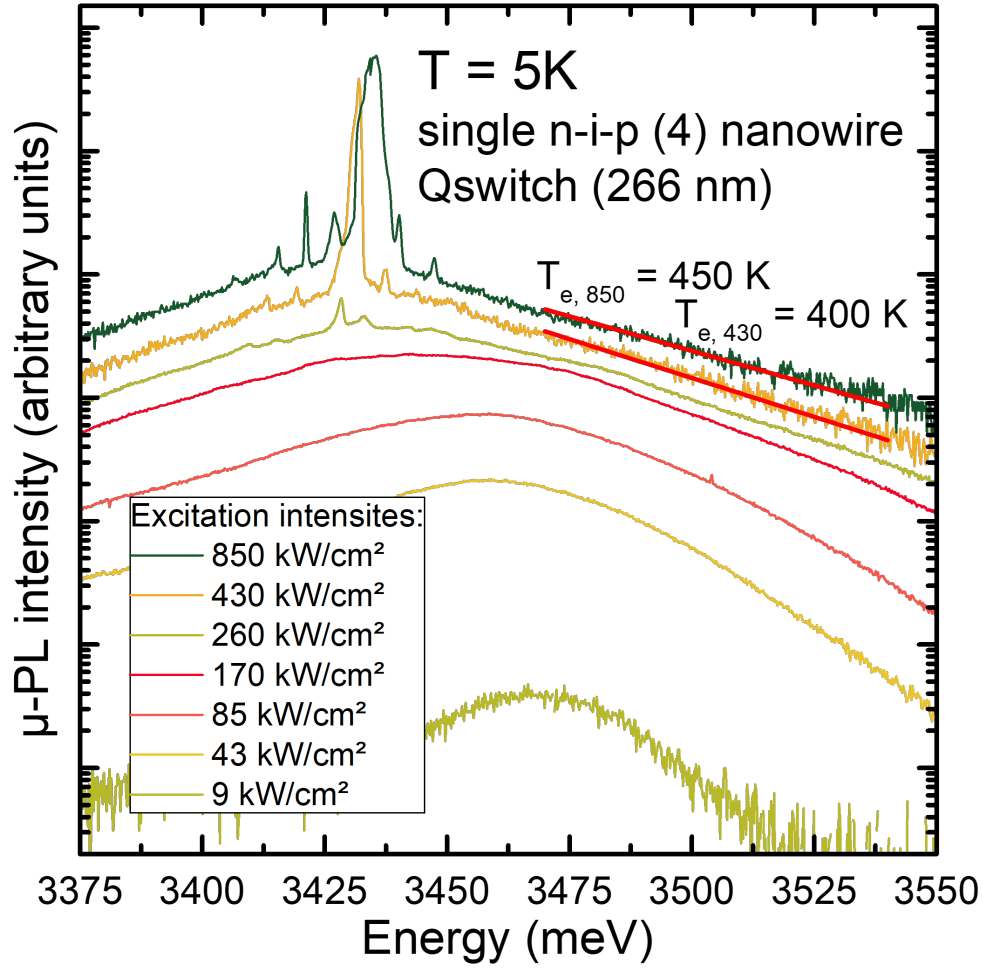


Figure IV.16 – μ -PL spectra with increasing excitation intensities on a single n-i-p nanowire (n-i-p (4)). Laser effect is evidenced for high excitation density with a threshold of 260 kW/cm^2

On figure IV.19 the PL spectrum of the nanowire at 850 kW/cm^2 is plotted with the associated variation of refractive index where the excitons have not been taken into account (in black points) with several interference orders (k lines) ranging from $k = 75$ to $k = 79$. Figure IV.19 also gives a close-up view of lasing modes at high excitation density for a single nanowire where we can see the non-monotonic distribution of modes in wavelength. From this observation it can be deduced that such as a non-monotonic variation of the optical index occurs. This phenomenon is known to happen only in the vicinity of the gap (or an absorption discontinuity). We also find that under strong excitation, the redshift is significant. From figure IV.15 the estimated redshift is around 40 meV . The high energy tail seen on figure IV.16 also demonstrates a strong heating under the high excitation intensities and fitted electronic temperatures are as high as 400 K . Those observations suggests that the bandgap energy has been lowered.

Based on those experimental observations and interpretations, we can make the following assumptions: (i) the lasing effect is assumed to occur at the bandgap energy. (ii) Because of the high excitation intensities, the excitons are not involved in the lasing effect.

We know that optical modes can be guided in several ways and the light confinement is com-

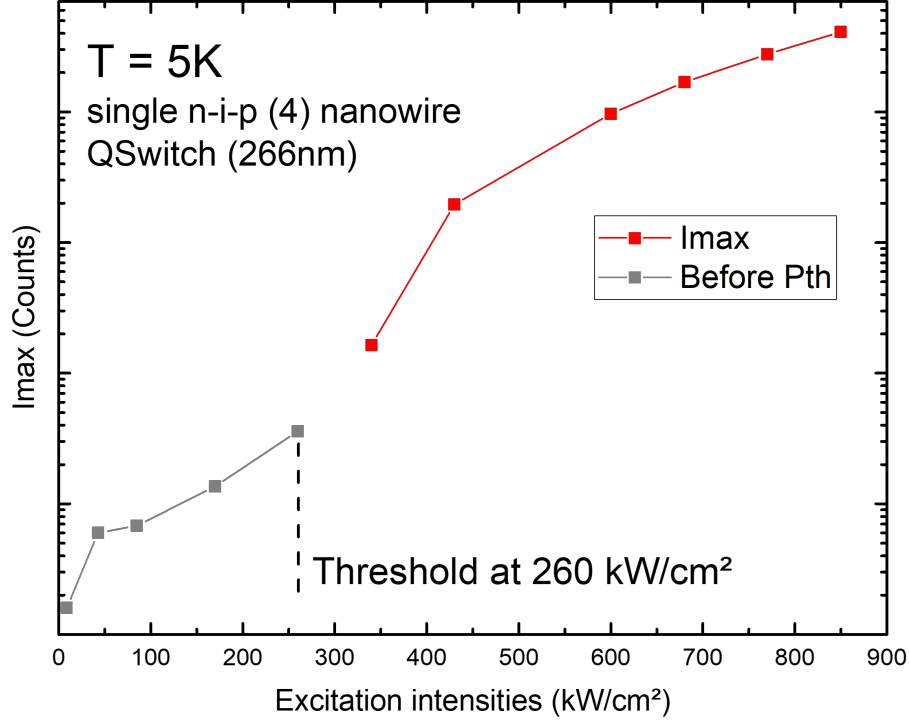


Figure IV.17 – Experimental characteristics of a laser effect inside a single n-i-p (4) nanowire: the photoluminescence intensity evolution is not linear after the threshold. The plot is obtained from the data on figure IV.16. The lasing threshold is estimated at 260 kW/cm².

plicated because of nanowire aspect ratio. With the hexagonal shape, whispering gallery modes or even radial Fabry-Perot cavity can be used to describe the light confinement. In our case, to know a bit more about what happens past the threshold, we make the assumption based on our experimental observations that the peaks can be interpreted as Perot-Fabry modes. Thus, we can interpret the figure IV.18 such as a Fabry-Perot cavity where the light is extracted near the extremities. This implies that the mode spacing can be expressed as a function of the wavelength variation as well as of the refractive index [160]. The mode spacing $\Delta\lambda$ can be written such as :

$$\Delta\lambda = \frac{\lambda^2}{(2d) \left[n - \lambda \left(\frac{dn}{d\lambda} \right) \right]} \quad (\text{IV.4})$$

where λ is the wavelength, d is the cavity length, and n is the index of refraction.

Also, if the single n-i-p nanowire can be understood such as an optical Fabry-Perot cavity and the peaks can be interpreted here as interferences, it is possible to calculate the characteristic resonance length associated with the interference modes. This result is expected to be in the same order of the length of the nanowire.

Consequently, we try to verify that the position of the modes can be found by graphical intersection of the interferences orders lines with the index variation of GaN measured by ellipsometry without considering excitons. The redshift of the bandgap is also taken into account.

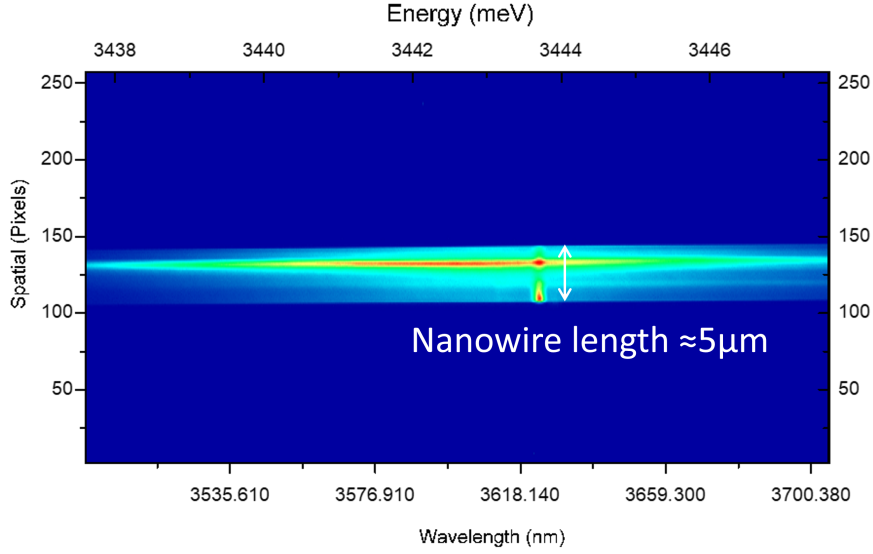


Figure IV.18 – 1D image of a single n-i-p nanowire under quasi continuous excitation. The nanowire length can be estimated on the y axis (measured in pixels), while the x axis display the luminescence wavelength (in nm). The luminescence is extracted near the ends of both extremities of the nanowire suggesting a Fabry-Perot cavity.

To verify it, we can therefore adapt the previous equation IV.4 in order to link the $2d$ term to the the wavelength difference between modes as well as the variation of the refractive index :

$$2d = \frac{\lambda_1 \lambda_2}{(\lambda_2 - \lambda_1) \left[n - \lambda_1 \left(\frac{dn}{d\lambda} \right) \right]} \quad (\text{IV.5})$$

where λ^2 is becoming λ_1 and λ_2 and $\Delta\lambda$ is the difference between each peaks wavelength, now written $(\lambda_2 - \lambda_1)$.

The equation IV.5 can not be used as such because the derivative of the refractive index is not monotonous. The intersection of the refractive index without excitons with the k lines will give us the solution to the following equation:

$$n(\lambda) = \frac{k}{2d} \lambda \quad (\text{IV.6})$$

For this analysis, the black dotted curve $n(\lambda)$ was measured by ellipsometry on an other sample and excitonic contributions have been removed. The red curve which corresponds to a slight modification of the previous measurements allows a perfect match with the position of the experimental longitudinal modes.

Finally, the plotted intersections of the interference orders and the modified refractive index match with the modes positions for a value of $2d = 10\mu\text{m}$. This graphical resolution works well with

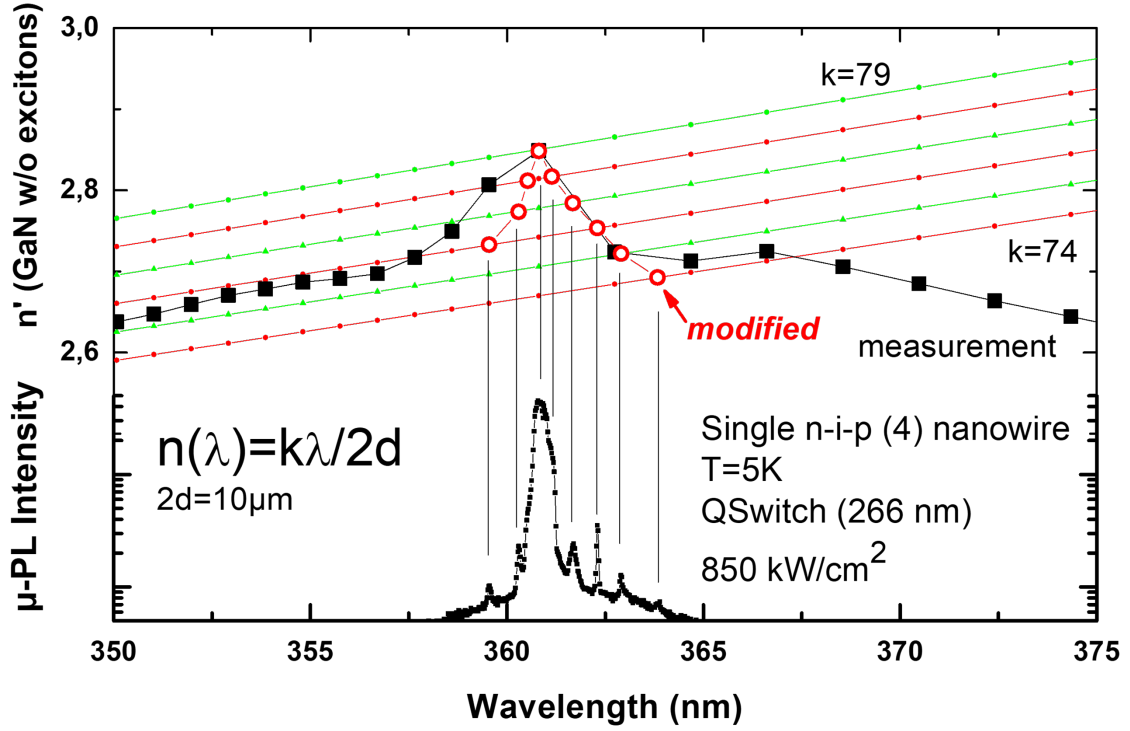


Figure IV.19 – In depth analysis of lasing modes for a single n-i-p (4) nanowire. The aim of this figure is to determine the characteristic length of the nanowire based on the assumption that the nanowires is behaving like a Fabry-Perot cavity. By plotting interference orders aligned with spectral modes the characteristic length of the nanowire can be deduced.

a single n-i-p nanowire of $5 \mu\text{m}$ estimated length. This analysis has shown that the laser effect in the single n-i-p nanowire is closely behaving as a Fabry-Perot cavity, thanks to that it was possible to calculate its length.

With all those experimental results and according to our hypothesis, we can make the conclusion that the nanowire will lose its excitons under high excitation intensities, in the same way as in the bulk GaN. The oscillator strength of the excitons within the nanowire are screened through the high excitation intensity and will lead to the creation of electron-hole pairs. Past the threshold the excitons don't exist anymore.

IV.6 Conclusion

The characterization of a single nanowire is experimentally challenging as the measured signal is very weak. The need to have a fully mastered setup and to identify the wire allows the realization

of extensive campaigns. It was possible to follow the evolution of a single wire in temperature and power. This first characterization opens the way to a more detailed study of time-resolved photoluminescence, first at room temperature, then as a function of temperature. The results show that the i-n structure does not essentially influence the μ -PL spectra as the optical transitions that was recorded were essentially similar to those of an unstrained bulk reference sample suggesting that only the intrinsic shell was probed. The power study has shown that high impact of electronic temperature over the broadening: with the rising power densities, electronic temperatures up to 250K were recorded. The TRPL campaign also revealed that the lifetimes are stable and not temperature dependent in their evolution and those stable results can be such interpreted as the evolution of decay lifetimes are essentially limited by channels of non-radiative recombination [154].

It was also possible to see a laser effect on a single n-i-p structured nanowire and to analyze the laser effect origin. The investigation regarding the longitudinal lasing modes have allowed us to deduce that the wire behaves like a Fabry-Perot cavity. The laser effect is probably coming from a classical gain mechanism featuring electron-hole pairs recombination. In our samples, the lasing threshold remain high and excitonic or polaritonic gain mechanisms are not yet usable. Those results could mean that the electrical injection could be hard to achieve in a radial p-i-n junction such as our samples as it would mean to inject high current to reach the threshold, leading to a premature degradation of the welded electrodes or even the nanowire.

Conclusion

This thesis has presented experimental measurements of some optical properties of bulk GaN and GaN core-shell nanowires. The experimental nature of this work led to many decisions regarding the evolution of the thesis topic and finally resulted in extensive on the study of the Mott density in bulk GaN. The experimental determination of the Mott density was a key moment of this thesis: there are relatively few fully experimental papers dealing with this subject (at low temperature as well as at high temperature). The experiments done in μ -PL with continuous and pulsed excitation lasers and the TRPL experiments have been carefully correlated: it is now possible to fully justify the determination of the carrier densities as function of the power density and as function of the temperature. All the results obtained during this thesis have been measured several times in order to guarantee the veracity and reliability of the campaigns. The second key part of this thesis was the understanding of optical properties under high optical injection in core-shell n-i-p doped nanowires. We could demonstrate the lasing effect in a single nanowire and analyze its gain mechanism. It was shown that in a regime of high excitation density, the excitons were screened into an electron-hole plasma.

The updated initial objective was to define the Mott density at low temperature for bulk GaN in order to delimit the domain of existence of excitons as function of carrier density in a bulk GaN layer. The results allowed us to complete our knowledge on the fundamental properties of this material and to better understand the different structures studied later. Subsequently, the nanowires have been the subject of many experimental campaigns. We could measure experimentally the decay time and deduce the carrier density of a single nanowire for a given power density and temperature.

The first chapter of this manuscript is used to lay the fundamental context; those theoretical foundations are necessary for the understanding of the physical phenomena experimentally observed in the rest of this thesis such as the main physical properties of GaN and the notion of excitons. The behavior under strong optical injection has been presented with the Mott transition and most specifically theoretical models allowing to calculate the vanishing of excitons. Those demonstrations were useful to present the main parameters related to the Mott transition in GaN.

The second chapter makes the link between the first theoretical part and the experimental results by presenting the different experimental techniques. This part details the different elements and techniques used in the μ -PL and TRPL setup. The principal optical transitions were described as well as

physical phenomena related to them (bandgap renormalization, thermalization effects, electron-hole recombination,...). This knowledge is required to interpret results that can be seen on self-supported bulk taking into account specificity such as dislocations, impurities linked to doping (intentional or not). We describe also the experiments that can be performed with our equipment and the different technical points necessary for the realization of accurate measurements. The measurement in μ -PL and TRPL strongly depends on the type of excitation and the quality of the spot focused on the sample: an image taken in real space allows to estimate if the excitation is well adjusted and optimized for the measurement (minimization of the size of the spot, clear image). Finally the measurement of spectrally or temporally resolved optical recombinations becomes possible.

In the third chapter the experimental results are presented: first the power and temperature studies in a self-supported bulk GaN sample allow us to observe the excitonic lines in a reference sample of very good crystalline quality. In temperature dependent experimentation, we observe the broadening of the excitonic lines from 80K with the decrease of the light intensity for the D^0X recombination in favor of the free excitons X_A . This phenomena is accompanied by a redshift to the low energy side. The power study shows the end of the exciton existence resulting from the bandgap reduction with increasing carrier density. The main optical transitions are clearly identified at low excitation levels. The energies of the free exciton (X_A and X_B) recombinations indicate that no residual strain is present in the sample. The first excited state of X_A exciton ($n=2$) is also detected at higher energy. With increasing power density, the free-exciton lines progressively disappear with the increase of the excitation intensity and the D^0X line peak shifts towards the low energy side. The redshift of the main luminescence peak (initially the D^0X transition) is concomitant with the disappearance of the excitonic signature. These results, together with the lifetime measurements, allow us to conclude that the Mott transition is reached in our bulk sample for a carrier density of $6 \times 10^{16} \text{ cm}^{-3}$ at 5K [161], in agreement with the estimation deduced from the calculation of the excitonic fraction using the Versteegh model. This new experimentally found value is one order of magnitude lower than the ones previously found in the literature and opens the discussion about the interpretation of the Mott transition in GaN based samples. It was also possible to push the reasoning further in order to observe the influence of the bi-molecular recombination term and to better identify the processes related to the evolution of carriers as a function of time and absorption. It was finally possible to find that our results are in line with a scaling law with other large bandgap semiconductors and to open this study to temperature dependent Mott density estimations.

Finally, the fourth and last chapter of the manuscript is dedicated to the spectroscopy of single nanowires. This part highlights the need to perfectly control the experimental setup given the high requirements related to the measurement of a single nanowire especially in TRPL as the signal obtained from a single nanowire is very weak. It could be achieved with the correct identification of the single nanowire thanks to a Si grid support and a good spot optimization first obtained through real space imaging then by tweak the measured signal. The relation between the μ -PL setup and TRPL setup is important here as the μ -PL results can be used as a reference as this first characterization allows to judge if the signal obtained with the TRPL setup is acceptable or not.

The work focused on two types of structures: n-i and n-i-p core-shell nanowires. Indeed, due to the difficulty of the bottom-up growth of undoped GaN nanowires by MOCVD, we tried first to circumvent the problem by studying the undoped shell of a core-shell n-i nanowire. In a first step, the power study shows the persistence of free excitons with the increase of the power density, the observed redshift is mainly due to the increase of the temperature of the nanowire associated with a broadening attributed to the electronic temperature. In a second step, it was possible to measure lifetimes as a function of temperature and power on a single wire previously studied by μ -photoluminescence. Thanks to this results we could fully characterize the optical properties of the n-i wire and see that the evolution of the lifetime does not depend on the temperature and could be limited by point defects, surface defects or strong internal electric field. Finally, the study of the lasing effect could be performed on the single core-shell n-i-p nanowire. The analysis of the modes by assuming that the nanowire behaved as a Fabry-Perot cavity allowed us to fall back on its characteristic dimension. This work led to a better understanding of the phenomena involved under the regime of strong optical injection, necessary for the realization of a nanodevice under electrical injection.

In the future, it would be interesting to extend this work with more complete studies as a function of temperature in particular for the determination of the Mott transition in bulk and nanowire based GaN samples. The realization of undoped nanowire with different aspect-ratio (diameter and length) would allow to complete the optical characterizations in a simpler structure than our n-i and n-i-p nanowires and would also open the way on the study of different propagation modes such as the gallery modes or radial Fabry-Perot modes for example. Finally, the characterization of the laser effect would be interesting to study longitudinal n-i-p nanowires, facilitating the realization of electrical contacts on each end of the nanowire.

Bibliography

- [1] P. Morgan Pattison, M. Hansen, and J. Y. Tsao, “LED lighting efficacy: Status and directions,” *Comptes Rendus Physique*, vol. 19, pp. 134–145, 3 2018.
- [2] E. Mallet, F. Réveret, P. Disseix, T. V. Shubina, and J. Leymarie, “Influence of excitonic oscillator strengths on the optical properties of GaN and ZnO,” *Physical Review B*, vol. 90, p. 045204, 7 2014.
- [3] J. Zúñiga-Pérez, V. Consonni, L. Lymperakis, X. Kong, A. Trampert, S. Fernández-Garrido, O. Brandt, H. Renevier, S. Keller, K. Hestroffer, M. R. Wagner, J. S. Reparaz, F. Akyol, S. Rajan, S. Rennesson, T. Palacios, and G. Feuillet, “Polarity in GaN and ZnO: Theory, measurement, growth, and devices,” *Applied Physics Reviews*, vol. 3, no. 4, 2016.
- [4] H. Amano, M. Kito, K. Hiramatsu, and I. Akasaki, “P-Type Conduction in Mg-Doped GaN Treated with Low-Energy Electron Beam Irradiation (LEEBI),” *Japanese Journal of Applied Physics*, vol. 28, pp. L2112–L2114, 12 1989.
- [5] S. Nakamura, T. Mukai, and M. Senoh, “Candela-class high-brightness InGaN/AlGaIn double-heterostructure blue-light-emitting diodes,” *Applied Physics Letters*, vol. 64, pp. 1687–1689, 3 1994.
- [6] D. Bajoni, “Polariton lasers. Hybrid light–matter lasers without inversion,” *Journal of Physics D: Applied Physics*, vol. 45, p. 313001, 8 2012.
- [7] A. Imamoglu, R. J. Ram, S. Pau, and Y. Yamamoto, “Nonequilibrium condensates and lasers without inversion: Exciton-polariton lasers,” *Physical Review A*, vol. 53, pp. 4250–4253, 6 1996.
- [8] B. Hönerlage, C. Klingshirn, and J. B. Grun, “Spontaneous emission due to exciton—electron scattering in semiconductors,” *physica status solidi (b)*, vol. 78, pp. 599–608, 12 1976.
- [9] G. Mohs, T. Aoki, R. Shimano, M. Kuwata-Gonokami, and S. Nakamura, “On the gain mechanism in GaN based laser diodes,” *Solid State Communications*, vol. 108, pp. 105–109, 8 1998.
- [10] A. Trichet, F. Médard, J. Zúñiga-Pérez, B. Alloing, and M. Richard, “From strong to weak coupling regime in a single GaN microwire up to room temperature,” *New Journal of Physics*, vol. 14, 2012.
- [11] J. Pankove, E. Miller, and J. Berkeyheiser, “GaN electroluminescent diodes,” *1971 International Electron Devices Meeting*, vol. 32, no. 3, pp. 78–78, 1971.
- [12] J. I. Pankove and H. Schade, “Photoemission from GaN,” *Applied Physics Letters*, vol. 25, pp. 53–55, 7 1974.

- [13] S. Nakamura, “Background story of the invention of efficient blue InGaN light emitting diodes (Nobel Lecture),” *Annalen der Physik*, vol. 527, pp. 335–349, 6 2015.
- [14] C. Monier, Fan Ren, Jung Han, Ping-Chih Chang, R. Shul, Kyu-Pil Lee, Anping Zhang, A. Baca, and S. Pearton, “Simulation of npn and pnp AlGaIn/GaN heterojunction bipolar transistors performances: limiting factors and optimum design,” *IEEE Transactions on Electron Devices*, vol. 48, pp. 427–432, 3 2001.
- [15] P. Caroff, J. Bolinsson, and J. Johansson, “Crystal Phases in III–V Nanowires: From Random Toward Engineered Polytypism,” *IEEE Journal of Selected Topics in Quantum Electronics*, vol. 17, pp. 829–846, 7 2011.
- [16] C. Stampfl and C. G. Van de Walle, “Density-functional calculations for III-V nitrides using the local-density approximation and the generalized gradient approximation,” *Physical Review B*, vol. 59, pp. 5521–5535, 2 1999.
- [17] I. Vurgaftman and J. R. Meyer, “Band parameters for nitrogen-containing semiconductors,” *Journal of Applied Physics*, vol. 94, pp. 3675–3696, 9 2003.
- [18] H. M. Ng, D. Doppalapudi, T. D. Moustakas, N. G. Weimann, and L. F. Eastman, “The role of dislocation scattering in n -type GaN films,” *Applied Physics Letters*, vol. 73, pp. 821–823, 8 1998.
- [19] D. Wu, W. Wang, W. Shih, R. Horng, C. Lee, W. Lin, and J. Fang, “Enhanced output power of near-ultraviolet InGaIn-GaN LEDs grown on patterned sapphire substrates,” *IEEE Photonics Technology Letters*, vol. 17, pp. 288–290, 2 2005.
- [20] T. Sugahara, H. Sato, M. Hao, Y. Naoi, S. Kurai, S. Tottori, K. Yamashita, K. Nishino, L. T. Romano, and S. Sakai, “Direct Evidence that Dislocations are Non-Radiative Recombination Centers in GaN,” *Japanese Journal of Applied Physics*, vol. 37, pp. L398–L400, 4 1998.
- [21] C. M. Park, Y. S. Park, H. Im, and T. W. Kang, “Optical properties of GaN nanorods grown by molecular-beam epitaxy; dependence on growth time,” *Nanotechnology*, vol. 17, pp. 952–955, 2 2006.
- [22] L. Cerutti, J. Ristić, S. Fernández-Garrido, E. Calleja, A. Trampert, K. H. Ploog, S. Lazic, and J. M. Calleja, “Wurtzite GaN nanocolumns grown on Si(001) by molecular beam epitaxy,” *Applied Physics Letters*, vol. 88, p. 213114, 5 2006.
- [23] R. B. Schwarz, K. Khachatryan, and E. R. Weber, “Elastic moduli of gallium nitride,” *Applied Physics Letters*, vol. 70, pp. 1122–1124, 3 1997.
- [24] M. Yamaguchi, T. Yagi, T. Sota, T. Deguchi, K. Shimada, and S. Nakamura, “Brillouin scattering study of bulk GaN,” *Journal of Applied Physics*, vol. 85, pp. 8502–8504, 6 1999.

- [25] K. Kim, W. R. L. Lambrecht, and B. Segall, “Elastic constants and related properties of tetrahedrally bonded BN, AlN, GaN, and InN,” *Physical Review B*, vol. 53, pp. 16310–16326, 6 1996.
- [26] A. Polian, M. Grimsditch, and I. Grzegory, “Elastic constants of gallium nitride,” *Journal of Applied Physics*, vol. 79, no. 6, pp. 3343–3344, 1996.
- [27] V. A. Savastenko and A. U. Sheleg, “Study of the elastic properties of gallium nitride,” *physica status solidi (a)*, vol. 48, pp. K135–K139, 8 1978.
- [28] O. Aoudé, P. Disseix, J. Leymarie, A. Vasson, M. Leroux, E. Aujol, B. Beaumont, A. Trassoudaine, and Y. André, “Continuous-wave and ultrafast coherent reflectivity studies of excitons in bulk GaN,” *Physical Review B*, vol. 77, p. 045206, 1 2008.
- [29] V. Y. Davydov, Y. E. Kitaev, I. Goncharuk, A. Smirnov, J. Graul, O. Semchinova, and D. Uffmann, “Phonon dispersion and Raman scattering in hexagonal GaN and AlN,” *Physical Review B - Condensed Matter and Materials Physics*, vol. 58, no. 19, pp. 12899–12907, 1998.
- [30] D. Sam-Giao, *Etude optique de nanofils GaN et de microcavités GaN/AlN*. PhD thesis, Université de Grenoble, 2012.
- [31] J. Lähnemann, O. Brandt, U. Jahn, C. Pfüller, C. Roder, P. Dogan, F. Grosse, A. Belabbes, F. Bechstedt, A. Trampert, and L. Geelhaar, “Direct experimental determination of the spontaneous polarization of GaN,” *Physical Review B*, vol. 86, p. 081302, 8 2012.
- [32] A. D. Bykhovski, B. L. Gelmont, and M. S. Shur, “Elastic strain relaxation and piezoeffect in GaN-AlN, GaN-AlGaN and GaN-InGaN superlattices,” *Journal of Applied Physics*, vol. 81, pp. 6332–6338, 5 1997.
- [33] E. Rosencher and B. Vinter, *Optoelectronics*. Cambridge University Press, 1 ed., 5 2002.
- [34] L. Lew Yan Voon, M. Willatzen, M. Cardona, and N. Christensen, “Terms linear in k in the band structure of wurtzite-type semiconductors,” *Physical Review B - Condensed Matter and Materials Physics*, vol. 53, no. 16, pp. 10703–10714, 1996.
- [35] S. Chuang, “Optical gain of strained wurtzite GaN quantum-well lasers,” *IEEE Journal of Quantum Electronics*, vol. 32, pp. 1791–1800, 10 1996.
- [36] S. Bloom, G. Harbeke, E. Meier, and I. B. Ortenburger, “Band Structure and Reflectivity of GaN,” *physica status solidi (b)*, vol. 66, pp. 161–168, 11 1974.
- [37] C. F. Klingshirn, *Semiconductor Optics*. Graduate Texts in Physics, Berlin, Heidelberg: Springer Berlin Heidelberg, 4 ed., 2012.
- [38] J. Frenkel, “On the Transformation of light into Heat in Solids. I,” *Physical Review*, vol. 37, pp. 17–44, 1 1931.

- [39] G. H. Wannier, “The Structure of Electronic Excitation Levels in Insulating Crystals,” *Physical Review*, vol. 52, pp. 191–197, 8 1937.
- [40] N. F. Mott, “Conduction in polar crystals. II. The conduction band and ultra-violet absorption of alkali-halide crystals,” *Transactions of the Faraday Society*, vol. 34, pp. 500–506, 1938.
- [41] D. Ahn and S.-H. Park, “Cuprous halides semiconductors as a new means for highly efficient light-emitting diodes,” *Scientific Reports*, vol. 6, p. 20718, 2 2016.
- [42] W. Y. Liang and A. D. Yoffe, “Transmission Spectra of ZnO Single Crystals,” *Physical Review Letters*, vol. 20, pp. 59–62, 1 1968.
- [43] U. Ozgür, Y. I. Alivov, C. Liu, A. Teke, M. A. Reshchikov, S. Doğan, V. Avrutin, S.-J. Cho, and H. Morkoç, “A comprehensive review of ZnO materials and devices,” *Journal of Applied Physics*, vol. 98, p. 041301, 8 2005.
- [44] M. Feneberg, R. A. R. Leute, B. Neuschl, K. Thonke, and M. Bickermann, “High-excitation and high-resolution photoluminescence spectra of bulk AlN,” *Physical Review B*, vol. 82, p. 075208, 8 2010.
- [45] I. Hernandez-Calderon, “Optical Properties and Electronic Structure of Wide Band Gap II-VI Semiconductors,” in *II-VI Semiconductor Materials and Their Applications*, pp. 113–170, Routledge, 5 2018.
- [46] K. Kornitzer, T. Ebner, K. Thonke, R. Sauer, C. Kirchner, V. Schwegler, M. Kamp, M. Leszczynski, I. Grzegory, and S. Porowski, “Photoluminescence and reflectance spectroscopy of excitonic transitions in high-quality homoepitaxial GaN films,” *Physical Review B*, vol. 60, pp. 1471–1473, 7 1999.
- [47] M. Wörz, E. Griehl, T. Reisinger, R. Flierl, B. Haserer, T. Semmler, T. Frey, and W. Gebhardt, “Gap Energies, Exciton Binding Energies and Band Offsets in Ternary ZnMgSe Compounds and ZnSe/ZnMgSe Heterostructures,” *physica status solidi (b)*, vol. 202, pp. 805–816, 8 1997.
- [48] S. B. Nam, D. C. Reynolds, C. W. Litton, R. J. Almassy, T. C. Collins, and C. M. Wolfe, “Free-exciton energy spectrum in GaAs,” *Physical Review B*, vol. 13, pp. 761–767, 1 1976.
- [49] C. Klingshirn, R. Hauschild, J. Fallert, and H. Kalt, “Room-temperature stimulated emission of ZnO: Alternatives to excitonic lasing,” *Physical Review B*, vol. 75, p. 115203, 3 2007.
- [50] E. Mallet, *Etude des propriétés polaritoniques de ZnO et GaN. Application à l’étude de l’effet laser à polaritons dans une microcavité*. PhD thesis, Université Clermont Auvergne, 2015.
- [51] W. Shan, B. D. Little, A. J. Fischer, J. J. Song, B. Goldenberg, W. G. Perry, M. D. Bremser, and R. F. Davis, “Binding energy for the intrinsic excitons in wurtzite GaN,” *Physical Review B*, vol. 54, pp. 16369–16372, 12 1996.

- [52] M. Tchounkeu, O. Briot, B. Gil, J. P. Alexis, and R. L. Aulombard, “Optical properties of GaN epilayers on sapphire,” *Journal of Applied Physics*, vol. 80, no. 9, pp. 5352–5360, 1996.
- [53] D. C. Reynolds, D. C. Look, W. Kim, O. Aktas, A. Botchkarev, A. Salvador, H. Morkoc, and D. N. Talwar, “Ground and excited state exciton spectra from GaN grown by molecular-beam epitaxy,” *Journal of Applied Physics*, vol. 80, pp. 594–596, 7 1996.
- [54] A. Shikanai, T. Azuhata, T. Sota, S. Chichibu, A. Kuramata, K. Horino, and S. Nakamura, “Biaxial strain dependence of exciton resonance energies in wurtzite GaN,” *Journal of Applied Physics*, vol. 81, pp. 417–424, 1 1997.
- [55] G. D. Chen, M. Smith, J. Y. Lin, H. X. Jiang, S. Wei, M. Asif Khan, and C. J. Sun, “Fundamental optical transitions in GaN,” *Applied Physics Letters*, vol. 68, pp. 2784–2786, 5 1996.
- [56] A. S. Barker and M. Ilegems, “Infrared Lattice Vibrations and Free-Electron Dispersion in GaN,” *Physical Review B*, vol. 7, pp. 743–750, 1 1973.
- [57] D. C. Reynolds, J. Hoelscher, C. Litton, and T. C. Collins, “Strain splitting of the Γ_5 and Γ_6 free excitons in GaN,” *Applied Physics Letters*, vol. 81, pp. 3792–3794, 11 2002.
- [58] S. L. Chuang and C. S. Chang, “k.p method for strained wurtzite semiconductors,” *Physical Review B*, vol. 54, pp. 2491–2504, 7 1996.
- [59] D. D. Sell, S. E. Stokowski, R. Dingle, and J. V. DiLorenzo, “Polariton Reflectance and Photoluminescence in High-Purity GaAs,” *Physical Review B*, vol. 7, pp. 4568–4586, 5 1973.
- [60] F. Evangelisti, J. U. Fischbach, and A. Frova, “Dependence of exciton reflectance on field and other surface characteristics: The case of InP,” *Physical Review B*, vol. 9, pp. 1516–1524, 2 1974.
- [61] J. J. Hopfield and D. G. Thomas, “Theoretical and Experimental Effects of Spatial Dispersion on the Optical Properties of Crystals,” *Physical Review*, vol. 132, pp. 563–572, 10 1963.
- [62] O. Aoudé, *Etude des propriétés excitoniques de GaN par spectroscopies continue et résolue en temps à l’échelle de la femtoseconde*. PhD thesis, Université Clermont-Auvergne, 2006.
- [63] P. Vashishta and R. K. Kalia, “Universal behavior of exchange-correlation energy in electron-hole liquid,” *Physical Review B*, vol. 25, pp. 6492–6495, 5 1982.
- [64] C. Klingshirn, J. Fallert, O. Gogolin, M. Wissinger, R. Hauschild, M. Hauser, H. Kalt, and H. Zhou, “Linear and nonlinear optics, dynamics, and lasing in ZnO bulk and nanostructures,” *Journal of Luminescence*, vol. 128, pp. 792–796, 5 2008.
- [65] R. Zimmermann, “Nonlinear Optics and the Mott Transition in Semiconductors,” *physica status solidi (b)*, vol. 146, pp. 371–384, 3 1988.

- [66] K. Kyhm, R. A. Taylor, J. F. Ryan, B. Beaumont, and P. Gibart, “Electron-hole plasma mott transition and stimulated emission in GaN,” *Journal of the Korean Physical Society*, vol. 45, pp. 526–529, 12 2004.
- [67] C. Klingshirn, M. Jörger, T. Fleck, and A. Jolk, “Exciton transport in Cu₂O, exciton detection by field ionization in a Schottky barrier and intraexcitonic transitions,” *Solid State Communications*, vol. 134, no. 1-2, pp. 155–158, 2005.
- [68] M. A. M. Versteegh, T. Kuis, H. T. C. Stoof, and J. I. Dijkhuis, “Ultrafast screening and carrier dynamics in ZnO: Theory and experiment,” *Physical Review B*, vol. 84, p. 035207, 7 2011.
- [69] M. H. Anderson, J. R. Ensher, M. R. Matthews, C. E. Wieman, and E. A. Cornell, “Observation of Bose-Einstein Condensation in a Dilute Atomic Vapor,” *Collected Papers of Carl Wieman*, vol. 1, pp. 453–456, 1 2008.
- [70] J. M. Kosterlitz and D. J. Thouless, “Ordering, metastability and phase transitions in two-dimensional systems,” *Journal of Physics C: Solid State Physics*, vol. 6, pp. 1181–1203, 4 1973.
- [71] J. Kasprzak, M. Richard, S. Kundermann, A. Baas, P. Jeambrun, J. M. J. Keeling, F. M. Marchetti, M. H. Szymańska, R. André, J. L. Staehli, V. Savona, P. B. Littlewood, B. Deveaud, and L. S. Dang, “Bose–Einstein condensation of exciton polaritons,” *Nature*, vol. 443, pp. 409–414, 9 2006.
- [72] K. T. Tsen, D. K. Ferry, A. Botchkarev, B. Sverdlov, A. Salvador, and H. Morkoç, “Direct measurements of electron-longitudinal optical phonon scattering rates in wurtzite GaN,” *Applied Physics Letters*, vol. 71, pp. 1852–1853, 9 1997.
- [73] F. Tassone, C. Piermarocchi, V. Savona, A. Quattropani, and P. Schwendimann, “Bottleneck effects in the relaxation and photoluminescence of microcavity polaritons,” *Physical Review B*, vol. 56, pp. 7554–7563, 9 1997.
- [74] L. S. Dang, D. Heger, R. André, F. Bœuf, and R. Romestain, “Stimulation of Polariton Photoluminescence in Semiconductor Microcavity,” *Physical Review Letters*, vol. 81, pp. 3920–3923, 11 1998.
- [75] G. Weihs, H. Deng, D. Snoke, and Y. Yamamoto, “Polariton lasing in a microcavity,” *physica status solidi (a)*, vol. 201, pp. 625–632, 3 2004.
- [76] R. Balili, V. Hartwell, D. Snoke, L. Pfeiffer, and K. West, “Bose-Einstein Condensation of Microcavity Polaritons in a Trap,” *Science*, vol. 316, pp. 1007–1010, 5 2007.
- [77] E. Wertz, L. Ferrier, D. D. Solnyshkov, P. Senellart, D. Bajoni, A. Miard, A. Lemaître, G. Malpuech, and J. Bloch, “Spontaneous formation of a polariton condensate in a planar GaAs microcavity,” *Applied Physics Letters*, vol. 95, p. 051108, 8 2009.

- [78] P. Tsotsis, P. S. Eldridge, T. Gao, S. I. Tsintzos, Z. Hatzopoulos, and P. G. Savvidis, “Lasing threshold doubling at the crossover from strong to weak coupling regime in GaAs microcavity,” *New Journal of Physics*, vol. 14, p. 023060, 2 2012.
- [79] N. Antoine-Vincent, F. Natali, D. Byrne, A. Vasson, P. Disseix, J. Leymarie, M. Leroux, F. Semond, and J. Massies, “Observation of Rabi splitting in a bulk GaN microcavity grown on silicon,” *Physical Review B*, vol. 68, p. 153313, 10 2003.
- [80] F. Semond, I. R. Sellers, F. Natali, D. Byrne, M. Leroux, J. Massies, N. Ollier, J. Leymarie, P. Disseix, and A. Vasson, “Strong light-matter coupling at room temperature in simple geometry GaN microcavities grown on silicon,” *Applied Physics Letters*, vol. 87, p. 021102, 7 2005.
- [81] R. Shimada, J. Xie, V. Avrutin, U. Ozgur, and H. Morkoc, “Cavity polaritons in ZnO-based hybrid microcavities,” *Applied Physics Letters*, vol. 92, no. 1, p. 011127, 2008.
- [82] S. Faure, C. Brimont, T. Guillet, T. Bretagnon, B. Gil, F. Médard, D. Lagarde, P. Disseix, J. Leymarie, J. Zúñiga-Pérez, M. Leroux, E. Frayssinet, J. C. Moreno, F. Semond, and S. Bouchoule, “Relaxation and emission of Bragg-mode and cavity-mode polaritons in a ZnO microcavity at room temperature,” *Applied Physics Letters*, vol. 95, p. 121102, 9 2009.
- [83] G. Oohata, T. Nishioka, D. Kim, H. Ishihara, and M. Nakayama, “Giant Rabi splitting in a bulk CuCl microcavity,” *Physical Review B*, vol. 78, p. 233304, 12 2008.
- [84] A. Pawlis, A. Khartchenko, O. Husberg, D. As, K. Lischka, and D. Schikora, “Large room temperature Rabi-splitting in a ZnSe/(Zn,Cd)Se semiconductor microcavity structure,” *Solid State Communications*, vol. 123, pp. 235–238, 8 2002.
- [85] K. Sebal, A. Trichet, M. Richard, L. S. Dang, M. Seyfried, S. Klemmt, C. Kruse, and D. Hommel, “Optical polariton properties in ZnSe-based planar and pillar structured microcavities,” *The European Physical Journal B*, vol. 84, pp. 381–384, 12 2011.
- [86] S. Raychaudhuri and E. T. Yu, “Calculation of critical dimensions for wurtzite and cubic zinc blende coaxial nanowire heterostructures,” *Journal of Vacuum Science & Technology B: Microelectronics and Nanometer Structures*, vol. 24, no. 4, p. 2053, 2006.
- [87] F. Glas, “Critical dimensions for the plastic relaxation of strained axial heterostructures in free-standing nanowires,” *Physical Review B*, vol. 74, p. 121302, 9 2006.
- [88] A. Waag, X. Wang, S. Fündling, J. Ledig, M. Erenburg, R. Neumann, M. Al Suleiman, S. Merzsch, J. Wei, S. Li, H. H. Wehmann, W. Bergbauer, M. Straßburg, A. Trampert, U. Jahn, and H. Riechert, “The nanorod approach: GaN NanoLEDs for solid state lighting,” *physica status solidi (c)*, vol. 8, pp. 2296–2301, 7 2011.

- [89] H. Sekiguchi, K. Kishino, and A. Kikuchi, "Emission color control from blue to red with nanocolumn diameter of InGaN/GaN nanocolumn arrays grown on same substrate," *Applied Physics Letters*, vol. 96, p. 231104, 6 2010.
- [90] A.-L. Henneghien, G. Tourbot, B. Daudin, O. Lartigue, Y. Désières, and J.-M. Gérard, "Optical anisotropy and light extraction efficiency of MBE grown GaN nanowires epilayers," *Optics Express*, vol. 19, p. 527, 1 2011.
- [91] J. Wang, "Highly Polarized Photoluminescence and Photodetection from Single Indium Phosphide Nanowires," *Science*, vol. 293, pp. 1455–1457, 8 2001.
- [92] X. Duan, Y. Huang, Y. Cui, J. Wang, and C. M. Lieber, "Indium phosphide nanowires as building blocks for nanoscale electronic and optoelectronic devices," *Nature*, vol. 409, pp. 66–69, 1 2001.
- [93] Z. Zhong, F. Qian, D. Wang, and C. M. Lieber, "Synthesis of p-Type Gallium Nitride Nanowires for Electronic and Photonic Nanodevices," *Nano Letters*, vol. 3, pp. 343–346, 3 2003.
- [94] F. Qian, Y. Li, S. Gradečak, D. Wang, C. J. Barrelet, and C. M. Lieber, "Gallium Nitride-Based Nanowire Radial Heterostructures for Nanophotonics," *Nano Letters*, vol. 4, pp. 1975–1979, 10 2004.
- [95] Y. Huang, X. Duan, and C. M. Lieber, "Nanowires for Integrated Multicolor Nanophotonics," *Small*, vol. 1, pp. 142–147, 10 2004.
- [96] M. H. Huang, S. Mao, H. Feick, H. Yan, Y. Wu, H. Kind, E. Weber, R. Russo, and P. Yang, "ChemInform Abstract: Room-Temperature Ultraviolet Nanowire Nanolasers.," *ChemInform*, vol. 32, pp. no–no, 5 2010.
- [97] J. C. Johnson, H.-J. Choi, K. P. Knutsen, R. D. Schaller, P. Yang, and R. J. Saykally, "Single gallium nitride nanowire lasers," *Nature Materials*, vol. 1, pp. 106–110, 10 2002.
- [98] X. Duan, Y. Huang, R. Agarwal, and C. M. Lieber, "Single-nanowire electrically driven lasers," *Nature*, vol. 421, pp. 241–245, 1 2003.
- [99] R. Agarwal, C. J. Barrelet, and C. M. Lieber, "Lasing in Single Cadmium Sulfide Nanowire Optical Cavities," *Nano Letters*, vol. 5, pp. 917–920, 5 2005.
- [100] I. Pelant and J. Valenta, *Luminescence Spectroscopy of Semiconductors*, vol. 9780199588. Oxford University Press, 2 2012.
- [101] D. C. Reynolds, D. C. Look, B. Jogai, and R. J. Molnar, "Evidence for shallow acceptors in GaN," *Journal of Applied Physics*, vol. 89, pp. 6272–6274, 6 2001.

- [102] A. Wysmolek, R. Stępniewski, M. Potemski, B. Chwalisz-Piętka, K. Pakuła, J. M. Baranowski, D. C. Look, S. S. Park, and K. Y. Lee, “Magnetopolaron effect on shallow donors in GaN,” *Physical Review B*, vol. 74, p. 195205, 11 2006.
- [103] J. R. Haynes, “Experimental Proof of the Existence of a New Electronic Complex in Silicon,” *Physical Review Letters*, vol. 4, pp. 361–363, 4 1960.
- [104] O. Aoudé, P. Disseix, J. Leymarie, A. Vasson, E. Aujol, B. Beaumont, A. Trassoudaine, and Y. André, “Continuous wave and ultra-fast reflectivity studies for the determination of GaN excitonic oscillator strengths as a function of the in-plane biaxial strain,” *Superlattices and Microstructures*, vol. 40, pp. 166–173, 9 2006.
- [105] W. R. L. Lambrecht, B. Segall, J. Rife, W. R. Hunter, and D. K. Wickenden, “UV reflectivity of GaN: Theory and experiment,” *Physical Review B*, vol. 51, pp. 13516–13532, 5 1995.
- [106] S. A. Self, “Focusing of spherical Gaussian beams,” *Applied Optics*, vol. 22, p. 658, 3 1983.
- [107] M. A. M. Versteegh, D. Vanmaekelbergh, and J. I. Dijkhuis, “Room-Temperature Laser Emission of ZnO Nanowires Explained by Many-Body Theory,” *Physical Review Letters*, vol. 108, p. 157402, 4 2012.
- [108] J. G. Gay, “Screening of Excitons in Semiconductors,” *Physical Review B*, vol. 4, pp. 2567–2575, 10 1971.
- [109] S. Hess, R. A. Taylor, K. Kyhm, J. F. Ryan, B. Beaumont, and P. Gibart, “Femtosecond exciton dynamics and the Mott transition in GaN under resonant excitation,” *Physica Status Solidi (B) Basic Research*, vol. 216, pp. 57–62, 11 1999.
- [110] A. J. Fischer, B. D. Little, T. J. Schmidt, C.-K. Choi, J.-J. Song, R. D. Horning, and B. L. Goldenberg, “Ultrafast carrier dynamics in GaN epilayers studied by femtosecond pump-probe spectroscopy,” in *Ultrafast Phenomena in Semiconductors III* (K.-T. F. Tsen, ed.), vol. 3624, pp. 179–187, 5 1999.
- [111] F. Binet, J. Y. Duboz, J. Off, and F. Scholz, “High-excitation photoluminescence in GaN: Hot-carrier effects and the Mott transition,” *Physical Review B*, vol. 60, pp. 4715–4722, 8 1999.
- [112] D. Gogova, H. Larsson, A. Kasic, G. R. Yazdi, I. Ivanov, R. Yakimova, B. Monemar, E. Aujol, E. Frayssinet, J.-P. Faurie, B. Beaumont, and P. Gibart, “High-Quality 2” Bulk-Like Free-Standing GaN Grown by Hydride Vapour Phase Epitaxy on a Si-doped Metal Organic Vapour Phase Epitaxial GaN Template with an Ultra Low Dislocation Density,” *Japanese Journal of Applied Physics*, vol. 44, pp. 1181–1185, 3 2005.
- [113] M. Leroux, B. Beaumont, N. Grandjean, P. Lorenzini, S. Haffouz, P. Vennégues, J. Massies, and P. Gibart, “Luminescence and reflectivity studies of undoped, n- and p-doped GaN on (0001) sapphire,” *Materials Science and Engineering: B*, vol. 50, pp. 97–104, 12 1997.

- [114] A. Wysmolek, K. P. Korona, R. Stepniewski, J. M. Baranowski, J. Bloniarz, M. Potemski, R. L. Jones, D. C. Look, J. Kuhl, S. S. Park, and S. K. Lee, "Recombination of excitons bound to oxygen and silicon donors in freestanding GaN," *Physical Review B*, vol. 66, p. 245317, 12 2002.
- [115] J. A. Freitas, W. J. Moore, and B. V. Shanabrook, "Comment on "Recombination of excitons bound to oxygen and silicon donors in freestanding GaN"," 4 2004.
- [116] K. Pakuła, A. Wysmołek, K. Korona, J. Baranowski, R. Stępniewski, I. Grzegory, M. Boćkowski, J. Jun, S. Krukowski, M. Wróblewski, and S. Porowski, "Luminescence and reflectivity in the exciton region of homoepitaxial GaN layers grown on GaN substrates," *Solid State Communications*, vol. 97, pp. 919–922, 3 1996.
- [117] S. Fischer, D. Volm, D. Kovalev, B. Averboukh, A. Graber, H. Alt, and B. Meyer, "Shallow donors in epitaxial GaN," *Materials Science and Engineering: B*, vol. 43, pp. 192–195, 1 1997.
- [118] H. Teisseyre, G. Nowak, M. Leszczynski, I. Grzegory, M. Bockowski, S. Krukowski, S. Porowski, M. Mayer, A. Pelzmann, M. Kamp, K. J. Ebeling, and G. Karczewski, "Photoluminescence study on GaN homoepitaxial layers grown by molecular beam epitaxy," *MRS Internet Journal of Nitride Semiconductor Research*, vol. 1, p. e13, 6 1996.
- [119] D. Volm, K. Oettinger, T. Streibl, D. Kovalev, M. Ben-Chorin, J. Diener, B. K. Meyer, J. Majewski, L. Eckey, A. Hoffmann, H. Amano, I. Akasaki, K. Hiramatsu, and T. Detchprohm, "Exciton fine structure in undoped GaN epitaxial films," *Physical Review B*, vol. 53, pp. 16543–16550, 6 1996.
- [120] F. Calle, F. J. Sánchez, J. M. G. Tijero, M. A. Sánchez-García, E. Calleja, and R. Beresford, "Exciton and donor - acceptor recombination in undoped GaN on Si(111)," *Semiconductor Science and Technology*, vol. 12, pp. 1396–1403, 11 1997.
- [121] B. Monemar, P. P. Paskov, J. P. Bergman, A. A. Toropov, T. V. Shubina, T. Malinauskas, and A. Usui, "Recombination of free and bound excitons in GaN," *Physica Status Solidi (B) Basic Research*, vol. 245, no. 9, pp. 1723–1740, 2008.
- [122] P. J. Dean, J. D. Cuthbert, D. G. Thomas, and R. T. Lynch, "Two-Electron Transitions in the Luminescence of Excitons Bound to Neutral Donors in Gallium Phosphide," *Physical Review Letters*, vol. 18, pp. 122–124, 1 1967.
- [123] D. C. Reynolds, C. W. Litton, and T. C. Collins, "Excited States of Bound Exciton Complexes in CdS," *Physical Review*, vol. 174, pp. 845–849, 10 1968.
- [124] D. C. Reynolds, C. W. Litton, and T. C. Collins, "Excited Terminal States of Bound Exciton-Donor Complexes in CdSe," *Physical Review*, vol. 177, pp. 1161–1164, 1 1969.
- [125] D. C. Reynolds and T. C. Collins, "Excited Terminal States of a Bound Exciton-Donor Complex in ZnO," *Physical Review*, vol. 185, pp. 1099–1103, 9 1969.

- [126] D. C. Reynolds, C. W. Litton, R. J. Almassy, S. B. Nam, P. J. Dean, and R. C. Clarke, “Excited states of bound exciton complexes in InP,” *Physical Review B*, vol. 13, pp. 2507–2510, 3 1976.
- [127] R. Hauschild, H. Priller, M. Decker, J. Brückner, H. Kalt, and C. Klingshirn, “Temperature dependent band gap and homogeneous line broadening of the exciton emission in ZnO,” *Physica Status Solidi C: Conferences*, vol. 3, no. 4, pp. 976–979, 2006.
- [128] C. Netzel, V. Hoffmann, J. W. Tømm, F. Mahler, S. Einfeldt, and M. Weyers, “Temperature-Dependent Charge Carrier Diffusion in [0001[−]] Direction of GaN Determined by Luminescence Evaluation of Buried InGa⁺N Quantum Wells,” *Physica Status Solidi (B) Basic Research*, vol. 257, no. 6, p. 2000016, 2020.
- [129] H. Mathieu and H. Fanet, *Physique des semiconducteurs et des composants électroniques - 6ème édition: Cours et exercices corrigés*. Dunod, 6th editio ed., 2009.
- [130] H. Haug and S. Schmitt-Rink, “Basic mechanisms of the optical nonlinearities of semiconductors near the band edge,” *Journal of the Optical Society of America B*, vol. 2, p. 1135, 7 1985.
- [131] D. Snoke, “Predicting the ionization threshold for carriers in excited semiconductors,” *Solid State Communications*, vol. 146, pp. 73–77, 4 2008.
- [132] J. S. Im, A. Moritz, F. Steuber, V. Härle, F. Scholz, and A. Hangleiter, “Radiative carrier lifetime, momentum matrix element, and hole effective mass in GaN,” *Applied Physics Letters*, vol. 70, pp. 631–633, 2 1997.
- [133] S. Juršėnas, S. Miasojedovas, and A. Žukauskas, “Rate of radiative and nonradiative recombination in bulk GaN grown by various techniques,” *Journal of Crystal Growth*, vol. 281, pp. 161–167, 7 2005.
- [134] S. Juršėnas, S. Miasojedovas, A. Žukauskas, B. Lucznik, I. Grzegory, and T. Suski, “Carrier recombination and diffusion in GaN revealed by transient luminescence under one-photon and two-photon excitations,” *Applied Physics Letters*, vol. 89, p. 172119, 10 2006.
- [135] E. Kuokstis, G. Tamulaitis, K. Liu, M. S. Shur, J. W. Li, J. W. Yang, and M. Asif Khan, “Photoluminescence dynamics in highly nonhomogeneously excited GaN,” *Applied Physics Letters*, vol. 90, p. 161920, 4 2007.
- [136] T. Malinauskas, K. Jarašiūnas, R. Aleksiejunas, D. Gogova, B. Monemar, B. Beaumont, and P. Gibart, “Contribution of dislocations to carrier recombination and transport in highly excited ELO and HVPE GaN layers,” *physica status solidi (b)*, vol. 243, pp. 1426–1430, 6 2006.
- [137] M. Nagai, R. Shimano, and M. Kuwata-Gonokami, “Direct creation of electron–hole plasma by exciton Mott transition in CuCl,” *Journal of Luminescence*, vol. 87-89, pp. 192–194, 5 2000.

- [138] G. Manzke, D. Semkat, F. Richter, D. Kremp, and K. Henneberger, “Mott transition versus Bose-Einstein condensation of excitons,” *Journal of Physics: Conference Series*, vol. 210, p. 012020, 2 2010.
- [139] V. Egorov, G. Müller, R. Zimmermann, A. Dite, V. Lysenko, and V. Timofeev, “Photoconductivity of CdS under high excitation - indicating no homogeneous Mott transition,” *Solid State Communications*, vol. 38, pp. 271–274, 4 1981.
- [140] J. Shah, R. F. Leheny, and W. Wiegmann, “Low-temperature absorption spectrum in GaAs in the presence of optical pumping,” *Physical Review B*, vol. 16, pp. 1577–1580, 8 1977.
- [141] A. Gorgis, T. Flissikowski, O. Brandt, C. Chèze, L. Geelhaar, H. Riechert, and H. T. Grahn, “Time-resolved photoluminescence spectroscopy of individual GaN nanowires,” *Physical Review B*, vol. 86, p. 041302, 7 2012.
- [142] C. Pfüller, O. Brandt, T. Flissikowski, C. Chèze, L. Geelhaar, H. T. Grahn, and H. Riechert, “Statistical analysis of excitonic transitions in single, free-standing GaN nanowires: Probing impurity incorporation in the poissonian limit,” *Nano Research*, vol. 3, pp. 881–888, 12 2010.
- [143] C. Couteau, A. Larrue, C. Wilhelm, and C. Soci, “Nanowire Lasers,” *Nanophotonics*, vol. 4, pp. 90–107, 5 2015.
- [144] C. Tessarek, M. Heilmann, E. Butzen, A. Haab, H. Hardtdegen, C. Dieker, E. Spiecker, and S. Christiansen, “The Role of Si during the Growth of GaN Micro- and Nanorods,” *Crystal Growth & Design*, vol. 14, pp. 1486–1492, 3 2014.
- [145] B. O. Jung, S.-Y. Bae, Y. Kato, M. Imura, D.-S. Lee, Y. Honda, and H. Amano, “Morphology development of GaN nanowires using a pulsed-mode MOCVD growth technique,” *CrystEngComm*, vol. 16, no. 11, pp. 2273–2282, 2014.
- [146] R. Koester, J. S. Hwang, C. Durand, D. Le Si Dang, and J. Eymery, “Self-assembled growth of catalyst-free GaN wires by metal–organic vapour phase epitaxy,” *Nanotechnology*, vol. 21, p. 015602, 1 2010.
- [147] X. Wang, J. Hartmann, M. Mandl, M. Sadat Mohajerani, H.-H. Wehmann, M. Strassburg, and A. Waag, “Growth kinetics and mass transport mechanisms of GaN columns by selective area metal organic vapor phase epitaxy,” *Journal of Applied Physics*, vol. 115, p. 163104, 4 2014.
- [148] P. M. Coulon, B. Alloing, V. Brändli, P. Vennégues, M. Leroux, and J. Zúñiga-Pérez, “Dislocation filtering and polarity in the selective area growth of GaN nanowires by continuous-flow metal organic vapor phase epitaxy,” *Applied Physics Express*, vol. 9, no. 1, 2016.
- [149] J. Jayapalan, B. J. Skromme, R. P. Vaudo, and V. M. Phanse, “Optical spectroscopy of Si-related donor and acceptor levels in Si-doped GaN grown by hydride vapor phase epitaxy,” *Applied Physics Letters*, vol. 73, pp. 1188–1190, 8 1998.

- [150] B. Monemar, “Bound excitons in GaN,” *Journal of Physics: Condensed Matter*, vol. 13, pp. 7011–7026, 8 2001.
- [151] L. Viña, S. Logothetidis, and M. Cardona, “Temperature dependence of the dielectric function of germanium,” *Physical Review B*, vol. 30, pp. 1979–1991, 8 1984.
- [152] M. Leroux, N. Grandjean, B. Beaumont, G. Nataf, F. Semond, J. Massies, and P. Gibart, “Temperature quenching of photoluminescence intensities in undoped and doped GaN,” *Journal of Applied Physics*, vol. 86, pp. 3721–3728, 10 1999.
- [153] S. Biernacki, U. Scherz, and B. K. Meyer, “Temperature dependence of optical transitions between electronic energy levels in semiconductors,” *Physical Review B*, vol. 49, pp. 4501–4510, 2 1994.
- [154] T. Izumi, Y. Narukawa, K. Okamoto, Y. Kawakami, S. Fujita, and S. Nakamura, “Time-resolved photoluminescence spectroscopy in GaN-based semiconductors with micron spatial resolution,” *Journal of Luminescence*, vol. 87-89, pp. 1196–1198, 5 2000.
- [155] R. Dingle, K. L. Shaklee, R. F. Leheny, and R. B. Zetterstrom, “Stimulated Emission and Laser Action in Gallium Nitride,” *Applied Physics Letters*, vol. 19, pp. 5–7, 7 1971.
- [156] M. A. Khan, D. T. Olson, J. M. Van Hove, and J. N. Kuznia, “Vertical-cavity, room-temperature stimulated emission from photopumped GaN films deposited over sapphire substrates using low-pressure metalorganic chemical vapor deposition,” *Applied Physics Letters*, vol. 58, pp. 1515–1517, 4 1991.
- [157] S. Chang, N. B. Rex, R. K. Chang, G. Chong, and L. J. Guido, “Stimulated emission and lasing in whispering-gallery modes of GaN microdisk cavities,” *Applied Physics Letters*, vol. 75, pp. 166–168, 7 1999.
- [158] S. Bidnyk, T. J. Schmidt, B. D. Little, and J. J. Song, “Near-threshold gain mechanisms in GaN thin films in the temperature range of 20–700 K,” *Applied Physics Letters*, vol. 74, pp. 1–3, 1 1999.
- [159] I. Akasaki and H. Amano, “Retrospect and prospect of nitride research in Japan,” in *Proc. of the Topical Workshop on III-V Nitrides, Nagoya, Japan*, (Nagoya), pp. 193–195, 1995.
- [160] M. Law, D. J. Sirbully, J. C. Johnson, J. Goldberger, R. J. Saykally, and P. Yang, “Nanoribbon Waveguides for Subwavelength Photonics Integration,” *Science*, vol. 305, pp. 1269–1273, 8 2004.
- [161] L. Mallet-Dida, P. Disseix, F. Réveret, F. Médard, B. Alloing, J. Zúñiga-Pérez, and J. Leymarie, “The low temperature limit of the excitonic Mott density in GaN: an experimental reassessment,” *New Journal of Physics*, vol. 24, p. 033031, 3 2022.

RÉSUMÉ

Propriétés excitoniques dans le GaN massif et les nanofils de GaN sous forte excitation

Cette thèse présente l'étude du blanchiment des excitons sous une excitation optique quasi-continue dans un échantillon de GaN massif de haute qualité et dans des nanofils uniques de GaN. Des expériences de micro-photoluminescence et micro-photoluminescence résolue en temps en fonction de la puissance et de la température ont été réalisées dans le but d'observer l'évolution de la densité de porteurs injectés dans les échantillons. La photoluminescence résolue en temps permet de mesurer la durée de vie des porteurs en fonction de l'intensité d'excitation, qui s'avère nécessaire pour une évaluation précise de la densité de porteurs injectés. La valeur expérimentale de la densité excitonique de Mott dans le GaN massif trouvée dans ce travail est inférieure de plus d'un ordre de grandeur aux déterminations précédentes publiées dans la littérature et est en accord avec des calculs. Cette analyse approfondie des résultats expérimentaux a été menée au moyen d'une simulation numérique qui a permis d'estimer l'évolution de la distribution des porteurs en profondeur dans les échantillons.

Mots-Clefs: Semi-conducteurs, GaN, nanofil unique, couche massive, excitons, transition de Mott excitonique, spectroscopie, micro-photoluminescence, photoluminescence résolue en temps, densité de porteurs, temps de vie, génération de photoporteurs, forte injection optique

ABSTRACT

Excitonic properties in bulk GaN and GaN nanowires under high excitation

The aim of this thesis was to study the bleaching of excitons under a quasi-continuous optical excitation in a bulk GaN sample of high quality and single nanowires through power dependent micro-photoluminescence and time-resolved micro-photoluminescence experiments. Time-resolved photoluminescence allows to measure the carrier lifetime as a function of excitation intensity, which is required for a reliable evaluation of the injected carrier density. The experimental value of excitonic Mott density in bulk GaN found in this work is more than an order of magnitude smaller than previous determinations published in the literature and is in accordance with many-body calculations. An in-depth analysis of experimental results was carried out with the help of numerical simulations in order to estimate the evolution of the carrier distribution along the depth of the samples.

Key-words: Semiconductors, GaN, single nanowire, bulk, excitons, excitonic Mott transition, spectroscopy, micro-photoluminescence, time-resolved photoluminescence, carrier densities, lifetime, photo-carrier generation, high optical excitation